MICROCOPY RESOLUTION TEST CHART
NATIONAL BUREAU OF STANDARDS

ARO 12240.3-EL

REPORT DOCUMENTATION PAGE		READ INSTRUCTIONS BEFORE COMPLETING FORM
1. REPORT NUMBER	2. GOVT ACCESSION NO.	3. RECIPIENT'S CATALOG NUMBER
4. TITLE (and Subtitle) Microwave Relaxation and Microstructure in Polycrystalline Ferrites		5. TYPE OF REPORT & PERIOD COVERED Final Report, 1 Sept. 1974 to 30 Sept. 1977
		6. PERFORMING ORG. REPORT NUMBER
7. AUTHOR(s) Carl E. Patton		8. CONTRACT OR GRANT NUMBER(s) DAHC04 75 G 0010
9. PERFORMING ORGANIZATION NAME AND ADDRESS Department of Physics Colorado State University Fort Collins, Colorado 80523		10. PROGRAM ELEMENT, PROJECT, TASK AREA & WORK UNIT NUMBERS
11. CONTROLLING OFFICE NAME AND ADDRESS U.S. Army Research Office Post Office Box 12211 Research Triangle Park, NC 27709		12. REPORT DATE February 28, 1978
		13. NUMBER OF PAGES
14. MONITORING AGENCY NAME & ADDRESS(If different from Controlling Office)		15. SECURITY CLASS. (of this report) Unclassified
		15a. DECLASSIFICATION/DOWNGRADING SCHEDULE NA

16. DISTRIBUTION STATEMENT (of this Report)

Approved for public release; distribution unlimited.

17. DISTRIBUTION STATEMENT (of the abstract entered in Block 20, if different from Report)

NA

18. SUPPLEMENTARY NOTES

The findings in this report are not to be construed as an official Department of the Army position, unless so designated by other authorized documents.

19. KEY WORDS (Continue on reverse side if necessary and identify by block number)

20. ABSTRACT (Continue on reverse side if necessary and identify by block number)

The relationship between microstructure and microwave loss in polycrystalline ferrites has been investigated. Two classes of materials were used, polycrystalline yttrium iron garnet (YIG) with a systematic variation in porosity and grain size and arc-plasma-sprayed Li-Ti ferrite. Data include magnetization versus field at room temperature, near-resonance and off-resonance effective linewidth as functions of temperature from 100°K to 300°K at 10 GHz, and parallel pump spin-wave linewidth as a function of wave-number

DD FORM 1473 EDITION OF 1 NOV 65 IS OBSOLETE

ADA058652

DDC FILE COPY

at 9 GHz, for temperatures from 90°K to 370°K.

The data indicate that neither the transit-time nor the magnetostriction mechanism are reasonable sources of the intrinsic microwave losses in polycrystals. The YIG effective linewidth data suggest the importance of small second phase content, possibly in the grain boundaries, with a Curie temperature on the order of 300°K. The YIG high power data indicate that the mechanism(s) controlling the spin-wave linewidth are quite different from those limiting the effective linewidth. Significant increases in spin-wave linewidth occur at low temperature, while the effective linewidth is relatively constant at low temperature.

The data on the Li-ferrite materials prepared by the arc-plasma-spraying process indicate that this novel process is potentially of great value in the production of practical materials for radar applications. The effective linewidths and spin-wave linewidths are comparable to those parameters for conventionally prepared materials.

(18) ARO (19) 12240.3-EL

FINAL REPORT

(6) MICROWAVE RELAXATION AND MICROSTRUCTURE

IN

POLYCRYSTALLINE FERRITES

(9) Final rept. 1 Sep 74 - 30 Sep 77,

(10) Carl E. Patton and Geoffrey O. White

Department of Physics

Colorado State University

Fort Collins, Colorado 80523

(11) 28 Feb 78

(12) 146 p.

(15) Grant DAHC04-75-G-0010

United States Army Research Office

Research Triangle Park, North Carolina 27709

Grant Period: September 1, 1974 to

September 30, 1977

78 09 05 138

ABSTRACT

The relationship between microstructure and microwave loss in poly-
crystalline ferrites has been investigated. Two classes of materials were
used, polycrystalline yttrium iron garnet (YIG) with a systematic variation
in porosity and grain size and arc-plasma-sprayed Li-Ti ferrite. Data
include magnetization versus field at room temperature, near-resonance and
off-resonance effective linewidth as functions of temperature from 100°K to
300°K at 10 GHz, and parallel pump spin-wave linewidth as a function of
wave-number at 9 GHz, for temperatures from 90°K to 370°K.

The data indicate that neither the transit-time nor the magnetostriction
mechanism are reasonable sources of the intrinsic microwave losses in poly-
crystals. The YIG effective linewidth data suggest the importance of small
second phase content, possibly in the grain boundaries, with a Curie tem-
perature on the order of 300°K. The YIG high power data indicate that the
mechanism(s) controlling the spin-wave linewidth are quite different from
those limiting the effective linewidth. Significant increases in spin-wave
linewidth occur at low temperature, while the effective linewidth is rela-
tively constant at low temperature.

The data on the Li-ferrite materials prepared by the arc-plasma-
spraying process indicate that this novel process is potentially of great
value in the production of practical materials for radar applications. The
effective linewidths and spin-wave linewidths are comparable to those para-
meters for conventionally prepared materials.

FORWARD

This final report on Grant No. DAHC04-75-G-0010, entitled "Microwave Relaxation and Microstructure in Polycrystalline Ferrites", presents in technical format, the accomplishments made during the entire grant period from September 1, 1974 to September 30, 1977. These accomplishments fall into three categories: (1) those concerned with microwave techniques for the measurement of ferrite properties, (2) those concerned with the physics of microwave relaxation in polycrystalline ferrites, and (3) those concerned with the evaluation of practical polycrystalline ferrite materials for phased array radar. For background information, the reader is referred to the original proposal, ARO proposal number P-12240-EL, the references contained therein, and the bibliography at the end of this report.

TABLE OF CONTENTS

CHAPTER I

INTRODUCTION

The microwave properties of ferrite materials have been the subject
of several thousand papers in the technical literature over the past 25
years. The basic relaxation mechanisms are well understood, as discussed
by Sparks (1964) and Patton (1975). However, the attractiveness of poly-
crystalline ferrite applications in microwave devices which operate at
fields far from ferromagnetic resonance (FMR) has raised several new
problems, with implications for basic physical understanding as well as
materials engineering for devices. The basic dilemna may be concisely
stated. The accepted theories of microwave loss and nonlinear effects
indicate that when a polycrystalline ferrite is biased at fields very far
from FMR, the effective losses should be very nearly the same as those
for single crystals of the same material. In practice, the effective losses
are significantly higher, by as much as several orders of magnitude for
some microstructures. This clearly shows that the basic physics of relaxa-
tion in polycrystals is not understood. It also means that the performance
of devices that use polycrystalline ferrite materials is not optimum. It
is therefore important to (1) discover why the losses in polycrystals are
so large and (2) utilize that understanding to engineer better polycrystal-
line materials for device applications.

An effort to accomplish the first objective was initiated by scientists
at Raytheon Company, Philips GmbH, and Nippon Electric Company in the late
1960's. Significant progress has been made. A continuation of this effort
was the subject of the research done under the ARO grant DAHC04-75-G-0010.
The effort is currently continuing under ARO sponsorship, with a shift of
materials emphasis from YIG to Li ferrite, because of the tremendous versa-
tility of substituted Li ferrite in microwave applications and its low cost.

In the present investigation, the off-resonance effective linewidth and the spin-wave linewidth were studied as functions of temperature for polycrystalline yttrium iron garnet materials with a systematic variation in porosity and grain size, and for lithium ferrite materials prepared by the arc plasma spray technique (Babbitt, 1975). Insofar as substantial grant resources were devoted to the development of effective linewidth and spin-wave linewidth spectrometers for these measurements, the systems are described in detail. Chapter II discusses the effective linewidth technique and ferrite applications. Chapter III describes the effective linewidth system in detail. Chapter IV reviews general considerations related to spin-wave linewidth and instability processes in microwave ferrites at high power levels. Chapter V describes the high-power measurement system in detail. The results of the measurements of ΔH_{eff} and ΔH_k for polycrystalline YIG are presented in Chapters VI and VII. Chapter VIII concludes the report with a discussion of results on APS Li ferrite.

Chapters III and V deserve special comment. These chapters present very detailed discussions of the effective linewidth and spin-wave linewidth spectrometers, respectively. They constitute practical operation manuals for these systems. Such elaboration is considered appropriate because of the state-of-the-art or unique aspects of these systems, and the large fraction of grant resources devoted to them. Furthermore, many colleagues have requested details on the construction and operation of these systems.

CHAPTER II

THE EFFECTIVE LINEWIDTH TECHNIQUE:

APPLICATIONS TO POLYCRYSTALLINE FERRITES

A. INTRODUCTION

The most common measure of microwave loss in ferrimagnetic matter is
the ferromagnetic resonance linewidth ΔH. This resonance linewidth is a
useful parameter because it is easily measured with relatively simple
microwave instrumentation, and can be related to the fundamental properties
of the ferrimagnetic material. It is particularly useful for pure single
crystals of simple geometry, such as rods, spheres, or platelets. In such
cases, the linewidth is taken as a direct measure of the intrinsic ferro-
magnetic relaxation. In other classes of materials, such as polycrystalline
ferrites, the interpretation of the FMR linewidth is much more complex. In
these cases, demagnetizing fields due to pores, second phases, shape effects,
etc. will tend to broaden the measured linewidth. For an ensemble of ran-
domly oriented crystallites or magnetic particles, the crystalline anisotropy
will also tend to broaden the linewidth.

A more satisfactory approach for the study of fundamental relaxation
mechanisms in materials where substantial inhomogeneous broadening occurs
is to make appropriate measurements of the microwave responses off-resonance
at high field. At sufficiently high field, usually above about 7 kOe for
FMR at 10 GHz, inhomogeneous broadening or two-magnon scattering is
not operative in most ferrites. A suitable analysis of the microwave
response can yield a direct measure of intrinsic losses. Liu and Shaw
developed a method first reported by Motizuke et al. (1965) in which the
microwave susceptibility of a ferromagnetic sample is measured to determine
the relaxation rate of the spin system. Kohane and Schlömann (1968) and

4

Vrehen (1969) further developed the technique and expressed the relaxation rate in terms of an effective linewidth, ΔH_{eff}. This linewidth parameter simply expresses the relaxation rate η at any bias field in linewidth units. The resonance linewidth ΔH is related to the relaxation rate at resonance η_o according to

$$\Delta H \cong 2\, \eta_o/\gamma \tag{II.1}$$

where γ is the gyromagnetic ratio, $1.76 \times 10^7\ Oe^{-1}\ sec^{-1}$ for electrons. The effective linewidth is obtained from $\eta(H)$ in a similar manner.

$$\Delta H_{eff} = 2\, \eta(H)/\gamma \tag{II.2}$$

Here, H is used to specifically emphasize that η is the relaxation rate at any field value H.

The problem may be divided into three parts: (1) the microwave susceptibility of the sample must be related to the relaxation rate η. (2) The susceptibility must be related to the experimental parameters of the microwave system, namely the cavity frequency f and quality factor Q. (3) Measurements of Q and f must be made and then used to calculate η. These operations are discussed extensively elsewhere (Patton, 1975; Kaelberer, 1977) and only the essential results are given below.

B. MICROWAVE SUSCEPTIBILITY

From analysis of the equation of motion for the ferromagnetic magneti-
zation under crossed dc and linearly polarized microwave fields, one can
define the microwave susceptibility according to

$$4\pi m_x = (\chi' - i\chi'') h_x. \tag{II.3}$$

The subscript x denotes the x direction as the direction of polarization
for the microwave field. The sample is assumed to be saturated in a perpen-
ducilar direction by a static external field H_o to yield a saturation
induction $4\pi M_o$. The specific expressions for χ' and χ'' depend on the
choice of the equation of motion. For the Landau-Lifshitz (1935) form,
which appears to be applicable to many classes of metallic and insulator
ferromagnets and ferrimagnets, one obtains

$$\chi' = \frac{\omega_m}{2} \left[\frac{\omega_o - \omega}{(\omega_o - \omega)^2 + \eta^2} + \frac{\omega_o + \omega}{(\omega_o + \omega)^2 + \eta^2} \right] \tag{II.4}$$

$$\chi'' = \frac{\omega_m}{2} \left[\frac{\eta}{(\omega_o - \omega)^2 + \eta^2} + \frac{\eta}{(\omega_o + \omega)^2 + \eta^2} \right] \tag{II.5}$$

where

$$\omega_m = \gamma \, 4\pi M_o , \tag{II.6}$$

$$\omega_o = \gamma \, H_o \tag{II.7}$$

expresses the saturation induction $4\pi M_o$ and external field H_o in angular
frequency units. The ω term is the excitation frequency in radians/sec.
The above equations are restricted to spherical samples excited by a micro-
wave field which is uniform throughout the sample.

The power absorbed by the sample is proportional to χ'', the negative imaginary part of the susceptibility. In a normal FMR experiment, the absorbed power is measured versus field and a typical resonance curve is obtained. Such a curve of χ'' versus field H_o is shown in Fig. II.1. Resonance occurs at $H_o = \omega/\gamma$. The linewidth is $\Delta H = 2\eta_o/\gamma$ to a very good approximation, for $H_o >> \Delta H$. As mentioned above, however, η_o is often increased by inhomogeneous broadening effects and is not representative of the intrinsic loss of the sample. As discussed extensively (Kohane and Schlömann, 1968; Vrehen, 1969; Patton, 1975), the value of η at high fields will not include such effects and may be taken as intrinsic. The exact reasoning would require a review of spin-wave properties and magnon scattering relaxation. The interested reader is referred to the references cited above.

From Eqs. (II.4-5), it is clear that the measurement of χ'' at high field yields a value of η directly. For FMR at $H_o \sim 3500$ Oe at 10 GHz, and for fields above 5 kOe, the η^2 term in the denominator of Eq. (II.5) can be neglected. A simple expression for η, and hence ΔH_{eff}, results.

$$\eta = \frac{2\chi''}{\omega_m} \left[\frac{1}{(\omega_o - \omega)^2} + \frac{1}{(\omega_o + \omega)^2} \right]^{-1}. \qquad (II.8)$$

Furthermore, it should be noticed that at high fields χ' is independent of η.

$$\chi' = \frac{\omega_m}{2} \left[\frac{1}{\omega_o - \omega} + \frac{1}{\omega_o + \omega} \right]^{-1} \qquad (II.9)$$

In practice, this last result allows for the self-consistent determination of the cavity calibration constant and χ'' as a function of field. These considerations will be discussed shortly.
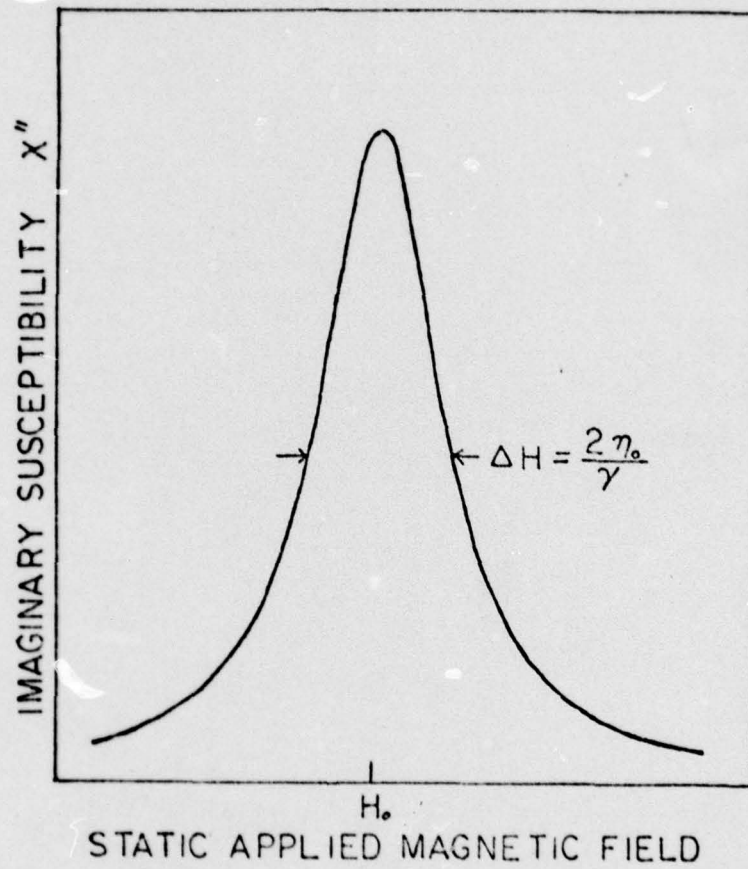
Figure II-1. Schematic ferromagnetic resonance curve.

C. MICROWAVE CAVITY PARAMETERS

It is now necessary to proceed to the second task, the relation of χ' and χ'' to the cavity parameters f and Q. This is accomplished by use of microwave cavity perturbation theory, in which it is assumed that the shapes of the cavity mode spatial field dependences are unaffected by the presence of the magnetic sample. One may then proceed to evaluate the change in cavity frequency f and quality factor Q due to the sample. An excellent review is provided by Green and Kohane (1964). Only the pertinent results are given here.

The essential results are as follows:

(1) The χ' component of the susceptibility leads to a frequency shift,

$$\chi' = -\frac{4V_c g}{V_s}\left(\frac{\omega_p - \omega_\infty}{\omega_p}\right) \tag{II.10}$$

Here, ω_p refers to the frequency of the cavity with the magnetic sample present, and ω_∞ refers to the frequency of the cavity with the magnetic sample absent. In order to include dielectric effects, ω_∞ is usually measured by leaving the sample in place and extrapolating the measured cavity frequency to infinite field. This procedure will be discussed shortly.

(2) The χ'' component of the susceptibility leads to a broadening of the frequency half width of the cavity $\Delta\omega$, which can be expressed in terms of the $Q = \omega/\Delta\omega$.

$$\chi'' = \frac{2V_c g}{V_s}\left(\frac{1}{Q_p} - \frac{1}{Q_\infty}\right) \tag{II.11}$$

Here, Q_p is the Q of the cavity at a given measuring field, and Q_∞ is the Q value for no magnetic effects. It is obtained by an extrapolation

procedure to infinite field. In Eqs. (II.10-11), V_c is the cavity volume, V_s is the sample volume, and g is a dimensionless cavity parameter that depends only on the cavity shape, dimensions, and mode configuration. For the TE_{011} cylindrical cavity used in these investigations,

$$g = \frac{J_1^2(x'_{01})}{4} \left[1 + \left(\frac{R\pi}{dx'_{01}} \right) \right]^2 \tag{II.12}$$

where J_1 is the first order Bessel function, x'_{01} is the first zero of the zero order Bessel function, R is the cavity radius, and d is the cavity height.

Assuming that the cavity frequency f and quality factor Q can be measured with sufficient accuracy, one can determine χ' and χ'' from Eqs. (II.10-11), and then use those results to determine η from Eqs. (II.4-5). Chapter III will consider the details of the experimental system and procedure. The remainder of this chapter will consider the application of the above results to the determination of ΔH_{eff} versus field, assuming that f versus field and Q versus field have been determined.

D.   THE INFINITE FIELD EXTRAPOLATION

The first task involves an extrapolation procedure to determine ω_∞ and Q_∞. From Eqs. (II.8-9) and Eqs. (II.10-11), one can obtain

$$\omega_p = -\left(\frac{V_s}{4V_c g}\right)\left(\frac{\gamma 4\pi M_o}{2}\right)\left[\frac{2\omega_o \omega_p}{\omega_o^2 - \omega_p^2}\right] + \omega_\infty , \qquad (II.13)$$

and

$$\frac{1}{Q_p} = 2\eta \left(\frac{V_s}{2V_c g}\right)\left(\frac{\gamma 4\pi M_o}{2}\right)\left[\frac{(\omega_o^2 + \omega_p^2)}{(\omega_o^2 - \omega_p^2)^2}\right] + \frac{1}{Q_\infty} , \qquad (II.14)$$

in the high field limit where $\eta >> |\omega_o - \omega_p|$ is satisfied. The square bracket term in Eq. (II.13) is roughly proportional to H_o^{-1} and will go to zero in the limit $H_o \to \infty$. Thus, a plot of the cavity frequency as a function of the square bracket term in Eq. (II.13) should be linear for sufficiently high field and have an extrapolated value of ω_∞. Figure II-2 illustrates the dependence for a test sample of yttrium iron garnet at several temperatures. The frequency is expressed as the shift from 9.94 GHz, in MHz for the vertical axis and in GHz for the horizontal axis. The data show that the dependence is quite linear at high field and provides a nice extrapolation to ω_∞. In practice, f_∞ can usually be determined to $\pm$ 10 kHz.

In a similar manner, Eq. (II.14) yields extrapolated values for Q_∞. The square bracket term here is proportional to H_o^{-2} in the high field limit. Representative plots of $\frac{1}{Q_p}$ versus the square bracket term are shown in Fig. II-3 for a YIG test sample. Here, the dependences are in approximate accord with Eq. (II.14) in that $\frac{1}{Q_p}$ decreases with increasing field. This is reasonable, since the magnetic loss decreases with increasing field. The extrapolated values of $\frac{1}{Q_\infty}$ decrease with temperature, i.e., Q_∞ increases as
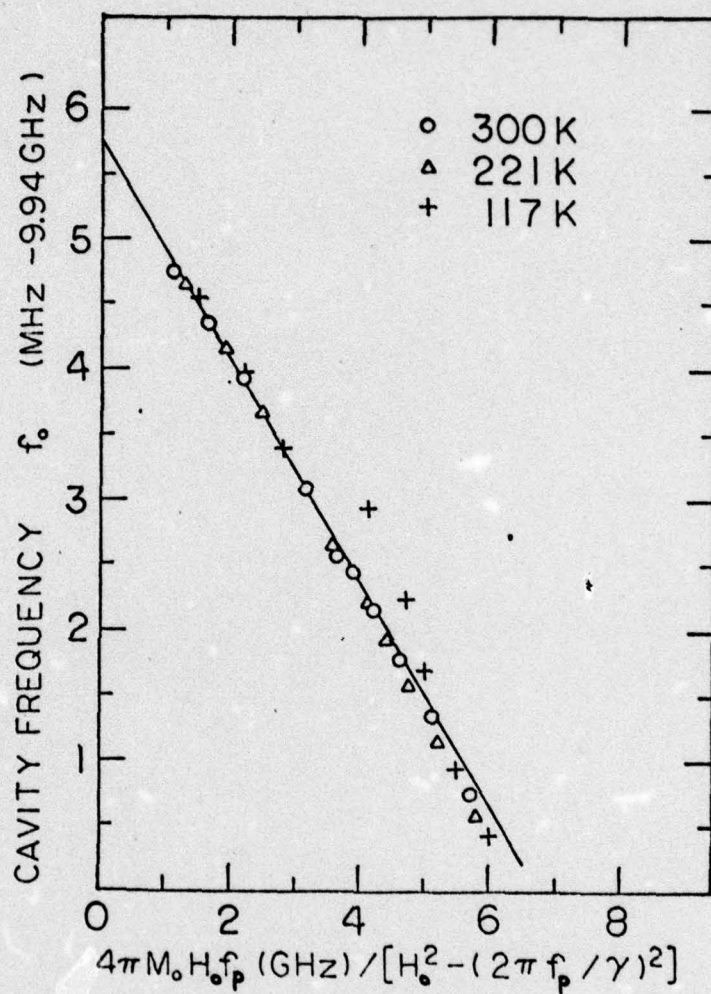
Figure II-2. Plot of cavity frequency versus the H_O^{-1} parameter to obtain the cavity frequency f_∞ in the $H_O = \infty$ limit, for a test sample of yttrium iron garnet (after Kaelberer, 1977).
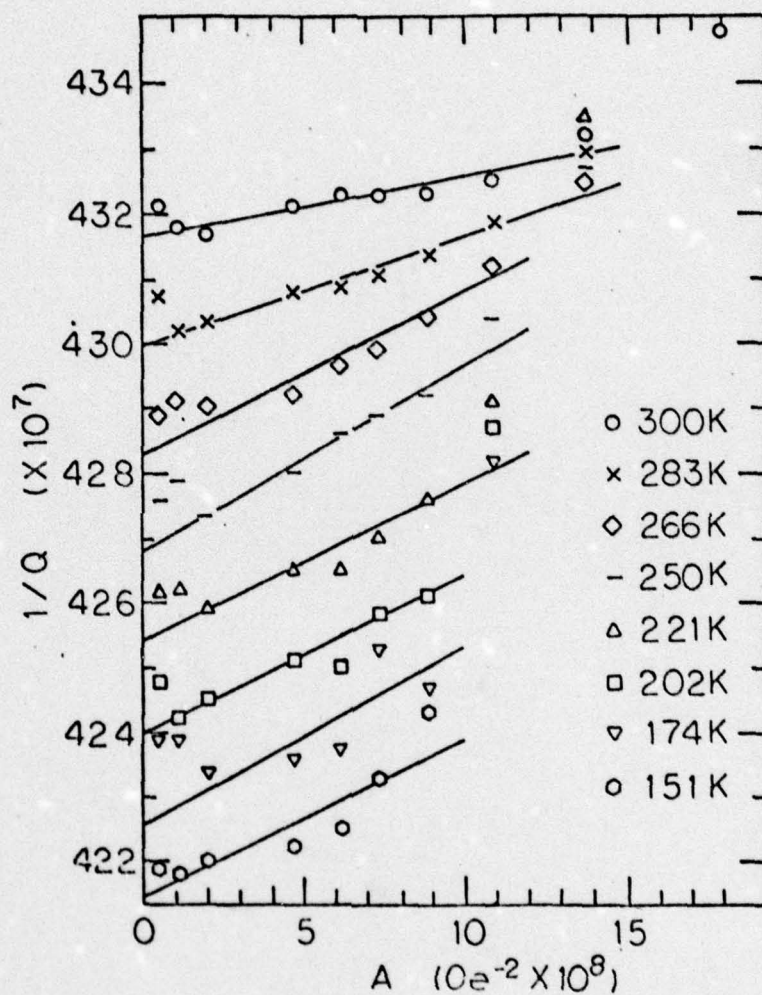
Figure II-3. Plot of inverse cavity Q versus the H^{-2} parameter to obtain the infinite field cavity Q, Q_∞, for a test sample of yttrium iron garnet (after Kaelberer, 1977).

the temperature of the cavity is reduced. This is also reasonable, since the resistive losses in the cavity walls decrease with decreasing temperature. In practice, $\frac{1}{Q_\infty}$ can usually be determined to within ± 0.1% by a least squares fitting procedure.

To recapitulate the results so far:

(1) Micromagnetic analysis based on a Landau-Lifshitz equation of motion yields working equations linking the microwave susceptibility χ with the relaxation rate η, gyromagnetic ratio γ, saturation induction $4\pi M_0$, external static field H_0, and the excitation frequency ω_p.

(2) Microwave cavity perturbation theory yields working equations linking the real part of the susceptibility to a frequency shift of the cavity, and linking the imaginary part to a change in $\frac{1}{Q}$ of the cavity.

(3) Combination of these working equations in the high field limit, with $\gamma H_0 >> \eta$ and η assumed equal to some constant intrinsic relaxation rate, yields an extrapolation procedure for obtaining f_∞ and Q_∞ for the cavity in the absence of magnetic effects.

E.   CALIBRATION AND EFFECTIVE LINEWIDTH DETERMINATION

As applied to ferrite polycrystalline materials, the application of the above results to determine the effective linewidth may be complicated by several factors.

(1) The preceeding analysis is for excitation of the uniform mode. The presence of other modes can lead to large errors and erroneous ΔH_{eff} values.

(2) In order to obtain an adequate signal-to-noise ratio for the accurate measurements of susceptibility, relatively large samples, 2-3 mm diam., are required. This will reduce the accuracy of the perturbation theory, as reflected in the g factor of Eqs. (II.11-14).

Problem (1) was minimized by utilizing a cylindrical TE_{011} cavity with the sample placed at the center. This arrangement provided a sufficiently homogeneous microwave excitation for the 2-3 mm diam. samples. A special calibration procedure was used to eliminate problem (2). The key to this procedure is contained in Eq. (II.9). In the high field region, Eq. (II.9) indicates that χ' is purely a function of the known parameters $\omega_m = \gamma 4\pi M_o$, H_o and ω. For a given ferrite, the gyromagnetic ratio γ and saturation induction are usually known. For dense YIG, we have

$$\gamma = 1.76 \times 10^7 \text{ Oe}^{-1} \text{ sec}^{-1}, \tag{II.15}$$

$$4\pi M_o = 1750 \text{ G (at room temperature)} \tag{II.16}$$

The frequency $\omega = \omega_p$ is determined experimentally. Since χ' at any field H_o is directly calculable, and ω_∞ is known from the extrapolation procedure described above, Eq. (II.10) may be used to obtain a purely empirical value of the cavity calibration coefficient $(V_c g/V_s)_e$. With this calibration

constant thus obtained, the high field effective linewidth may be obtained
from

$$\chi'' = 2 \left(\frac{V_c g}{V_s}\right)_e \left(\frac{1}{Q_p} - \frac{1}{Q_\infty}\right) \tag{II.17}$$

and Eq. (II.8). Recall that ΔH_{eff} is defined as $2\eta/\gamma$.

In actual practice, the following procedure was used:

(1) At a given temperature, Q_p and f_p were determined as functions
of field from $H_o = 7$ kOe to $H_o = 12$ kOe, in 500 Oe increments.

(2) The extrapolation procedure was used to determine f_∞ and Q_∞.

(3) The actual V_c, together with the theoretical value of g from Eq.
(II.12), was used to obtain values of (χ'_{exp}) at each field from the f_p data.

(4) At each field, the theoretical value of χ' from Eq. (II.9) was
compared with the experimental value (χ'_{exp}), to obtain a correction factor
for the cavity calibration.

(5) An average correction factor over the 7–12 kOe field interval
was used to obtain an average empirical cavity calibration $(V_c g/V_s)_e$ which
was then used to reevaluate χ' and χ'' from the data and Eqs. (II.2),
(II.4-7), (II.10-11), by an iterative method. No intrinsic value of γ was
needed in this last step.

The value of ΔH_{eff} versus H_o obtained by the above procedure is there-
fore self-consistent with an empirical cavity calibration which yields the
correct theoretical value of χ' versus field and a value of the gyro-
magnetic ratio γ which is close to the intrinsic value of 1.76×10^7 Oe^{-1}
sec^{-1}, within experimental error. Specific results will be presented and
discussed in Chapter VI.

CHAPTER III

EFFECTIVE LINEWIDTH SPECTROMETER

FOR THE TEMPERATURE RANGE 100-300°K

A. INTRODUCTION

The previous chapter describes a procedure by which measurements of the frequency f_p (or ω_p in rad/sec.) and cavity Q, Q_p, for a microwave cavity containing a magnetic sample, can be used to obtain the intrinsic high field effective linewidth ΔH_{eff}. Intrinsic is taken to mean the linewidth which would be observed if inhomogeneous broadening effects and two-magnon relaxation due to pores, second phase, inhomogeneous demagnetizing fields, and crystalline anisotropy were absent. The present chapter will describe the effective linewidth spectrometer which was developed under the ARO grant. The spectrometer represents a substantial improvement over the earlier system developed by Patton and Kohane (1972).

(1) Advances in microwave frequency measuring instrumentation now allow direct frequency measurement at 10 GHz to better than ± 10 Hz. Heterodyne methods and the consequent increase in frequency error are avoided.

(2) A temperature stabilized water bath and a well insulated circulation system were used to regulate the cavity temperature to about ± 0.01°C or better near 20°C. This allowed a substantial increase in the accuracy of the susceptibility measurements.

(3) A Varian temperature controller was adapted to the cavity system so that data could be obtained as a function of temperature down to about 100°K.

The following discussion will first focus on the interaction between the microwave cavity resonator and the sample FMR. Then a general description

of the system and theory of operation will be presented. Finally, the detailed design of the various subsystems of the spectrometer will be described.

B.   CAVITY-SAMPLE INTERACTION

The effective linewidth measurement involves the use of a transmission cavity with two coupling holes or irises. Power is coupled into the cavity from a variable frequency microwave source through one iris. The transmitted power, coupled out through the second iris, is monitored. The effects of the sample and cavity on the transmitted power are illustrated in Fig. III-1. The transmitted power P is plotted as a function of the microwave source frequency for three different situations.

In graph (a), the effect of the sample alone is shown. Imagine a situation with the sample simply placed in a non-resonant transmission waveguide system. With an applied field of $H_o = \omega_o/\gamma$, resonance occurs and a minimum in the transmitted power occurs at $\omega = \omega_o$. The curve is simply an inverted version of the ferromagnetic resonance curve in Fig. II-1, except that here the frequency is varied instead of the field.

For typical ferromagnetic materials, the frequency linewidth is on the order of 100-1000 MHz. This linewidth is measured between the points on the curve for which the decrease in transmitted power is one-half the maximum decrease. These points are indicated on graph (a) in Fig. III-1 by arrows.

Now consider the effect of the cavity on the transmitted power. Graph (b) shows the transmitted power for the cavity without the sample. Power is reflected back toward the source for all but a narrow band of frequencies centered around the resonant frequency of the cavity ω_r. The frequency width $\Delta\omega_r$ is related to the quality factor Q,

$$Q = \omega_r/\Delta\omega \quad .$$
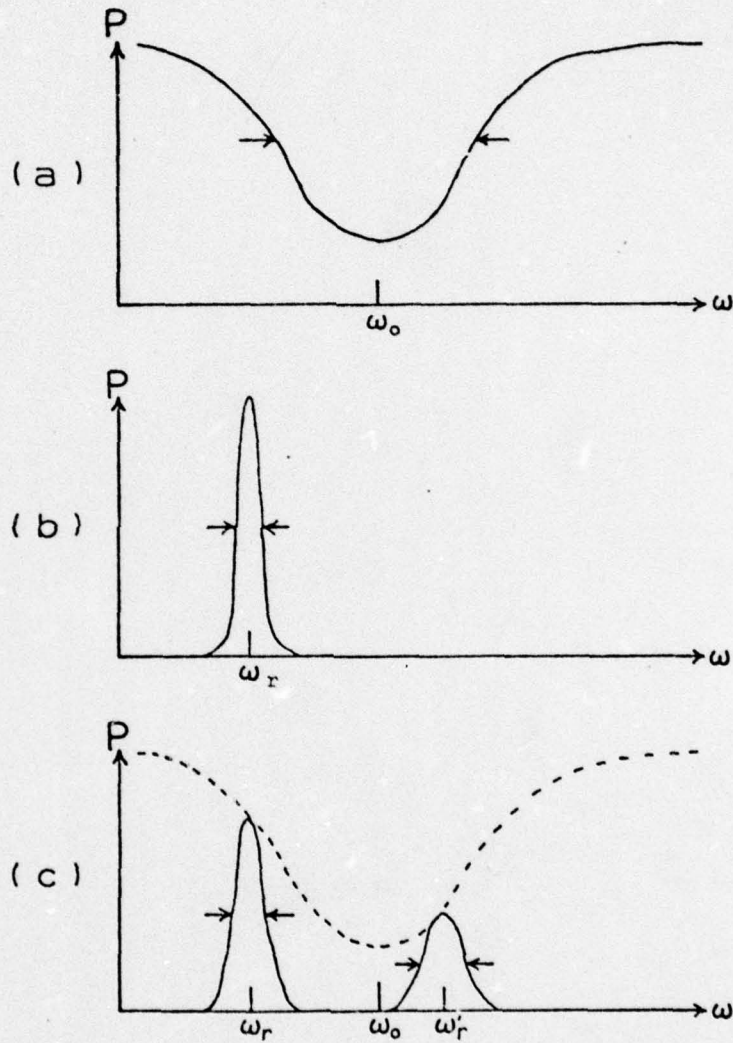
<div align="right">(III.1)</div>

Figure III-1. Schematic representation of the transmitted power for (a) the sample only, (b) the cavity only, (c) the sample and cavity combined (after Kaelberer, 1977).

The Q is inversely proportional to the energy dissipated in the cavity
due to the irises, the eddy currents in the cavity walls, and the magnetic
losses of the ferromagnetic sample when present. For typical x-band cavi-
ties at 9-10 GHz, a rectangular cavity with a TE_{10n} mode configuration will
have a Q of several thousand and a width on the order of 5 MHz. A
cylindrical TE_{011} cavity of OFHC (oxygen free high conductivity) copper
can have a Q in excess of 20,000 and a frequency half width less than
0.5 MHz. Such a cavity is used in the present spectrometer configuration
for high field ΔH_{eff} determinations. It can be seen, then, that the fre-
quency width of the cavity in graph (b) is more than 1000 times narrower
than the frequency width of the magnetic sample.

In graph (c), the combined effect of the sample and cavity on the
transmitted power is shown. Because of the much narrower frequency width
of the cavity, the frequency dependence of the power transmission exhibits
the cavity characteristic, while the peak transmitted power for a variation
in ω_r is characteristic of the sample resonance. Notice that if the sample
were placed in a second cavity with a frequency ω_r' which is closer to
sample resonance at ω_o, the measured bandwidth of the cavity would be
larger and the Q of the cavity would be smaller. In practice, one cavity
is used and the FMR frequency is swept by changing the applied field. For
the case of the high field effective linewidth measurement, we have

$$\omega_o = \gamma H_o >> \omega \qquad \qquad (III.2)$$

to ensure that $|\omega_o - \omega| >> \eta$ is satisfied. In terms of the graphs in
Fig. III-1, this means that ω_o is shifted very far to the right, the peak
in transmitted power is very close to that for the cavity with no magnetic

sample, and the cavity Q is only slightly smaller than that for the non-magnetic case. The change in $\frac{1}{Q}$, $\frac{1}{Q_p} - \frac{1}{Q_\infty}$, is related to χ'' of the sample, and the frequency shift, $\omega_p - \omega_\infty$ is related to χ', as discussed in Chapter II. With ω_o shifted very far to the right, these differences will be quite small since the system is essentially measurng the residual tail of the FMR curve. Consequently, the system must be capable of measuring the frequency and frequency width of the cavity with high accuracy.

C. MICROWAVE MEASUREMENT SYSTEM

The present microwave system is based on the design of Patton and Kohane (1972). The microwave system and associated components are indicated schematically in Fig. III-2. It is designed to operate at an X-band frequency of about 10 GHz. A klystron is used as the signal source. It feeds power into three branches of the system. The first branch simply provides a signal for the frequency counter. The second branch serves as a reference arm and provides a reference voltage from the reference crystal output. The third branch feeds, in sequence, a special two position attenuator, the microwave transmission cavity, and the signal crystal detector. The two position attenuator is calibrated for 0 and 3 db of attenuation. Additional components provide isolation and easy power level adjustment at appropriate points in the system.

The signals from the two crystals are fed to a comparing circuit which provides an error voltage. This error voltage may be fed back to the klystron and added to the repeller voltage to change the klystron frequency. Thus, the system may be operated in a feedback mode to lock the klystron to any selected point on the transmission curve of the cavity. In practice, the system is locked on the two half-power 3 db points on the cavity. The values of the frequency at each point are recorded as $f_\pm$, and the cavity frequency and Q are determined as

$$f_p = \frac{1}{2} (f_+ + f_-) , \tag{III.3}$$

$$Q_p = f_p / |f_+ - f_-| . \tag{III.4}$$

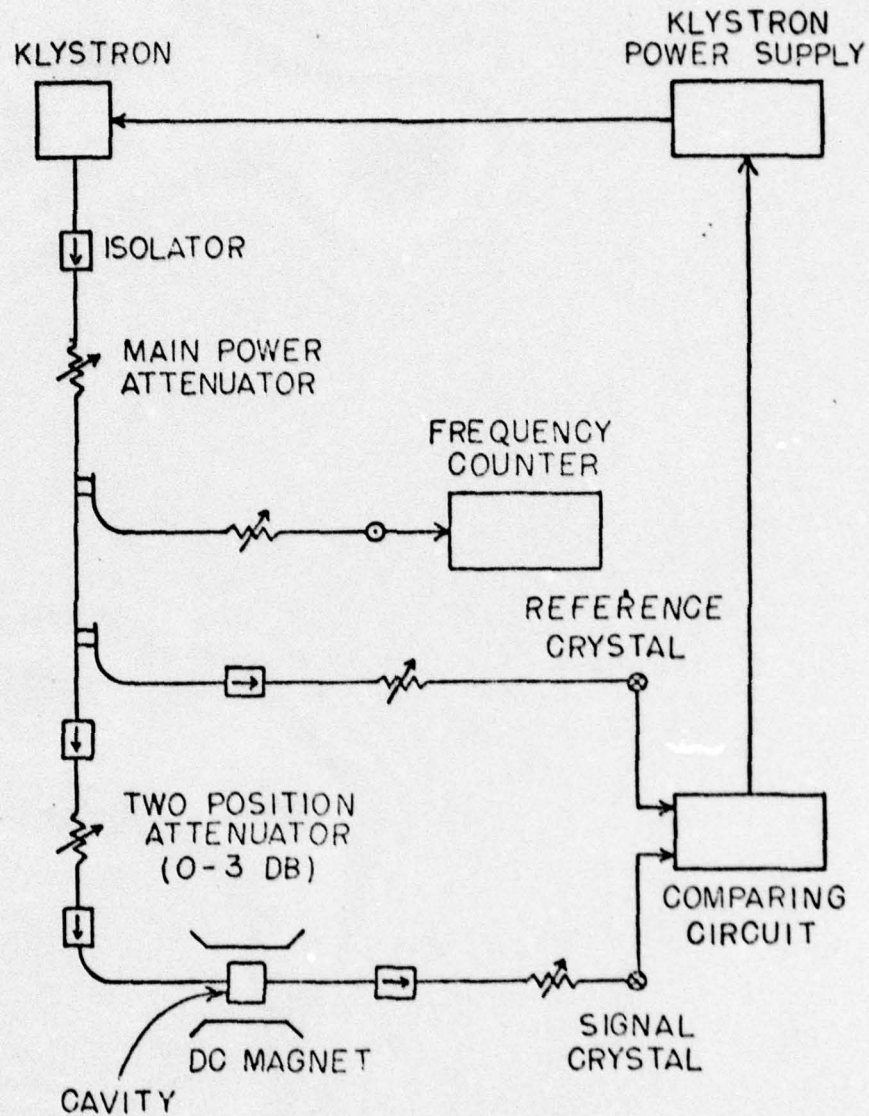The specific sequence of operations to achieve these values is as follows:

Figure III-2. Effective linewidth microwave system and associated components.

(1) With the feedback off, the klystron repeller voltage and klystron mechanical tuning are adjusted so that the cavity transmission peak is centered at the peak in the klystron mode curve. The signal crystal output is then maximum, and corresponds to the peak at ω_r in graph (b) of Fig. III-1.

(2) With the two-position attenuator in the 3 db position, the attenuator in the reference arm is adjusted until the reference crystal output is equal to the signal crystal output. This nulling part of the measurement is most critical.

(3) Next, the precision attenuator is changed to the 0 db position, which in turn creates an imbalance in the signals at the input to the comparing circuit.

(4) As the feedback is turned on, the error voltage generated by the imbalance between the two crystal voltages serves to drive the klystron to stable "locked-in" operation at one of the cavity 3 db point frequencies. By reversing the sign of the feedback, the lock is switched to the other 3 db point of the cavity. In each case, the high gain op amp in the feedback loop serves to shift the klystron to the proper 3 db frequency point at which the error voltage is effectively zero. In this way, f_+ and f_- are measured, f_p and Q_p are determined, and the procedures outlined in Chapter III are then used to obtain ΔH_{eff}.

D. MICROWAVE SYSTEM DETAIL

The microwave source is a Varian X-13 reflex klystron, which can produce up to 250 mw of microwave power over a frequency range of 8.2-12.4 GHz. The frequency and mode shape are adjusted by changing the repeller voltage and the mechanical length of the klystron cavity resonator. The klystron is controlled by a MicroNow model 753 B power supply which has been factory modified so that the feedback correction voltage can be added to the repeller voltage.

The comparing circuit generates a correction voltage which is referenced to ground. This presents a special problem in the coupling of the signal to the repeller voltage. Figure III-3 demonstrates the problem. Diagram (a) illustrates the conventional klystron hook-up. Both the beam voltage V_B and the repeller voltage V_R are referenced to cathode. This places the cathode at $- V_B$ with respect to ground. At this level, the addition of any error voltage to V_R would require some type of conversion. To keep the correction voltage configuration as simple as possible, the alternate hook-up in diagram (b) has been used. Here the repeller supply V_R' is also referenced to ground so that the correction voltage can be conveniently added. It is to be noted that two problems arise with this arrangement. First, the voltage of the repeller supply V_R' must be substantially larger than V_R.

$$V_R' = V_R + V_B \qquad\qquad (III.5)$$

For typical klystron operation at 40 ma with $V_B \sim 350$ V and $V_R \sim 500$ V, the V_R' supply must be capable of ~ 850 V. Second, care must be taken that V_R' is not allowed to fall below V_B, as a $V_R' < V_B$ condition causes klystron burn-out.

(a) Normal Klystron Connections
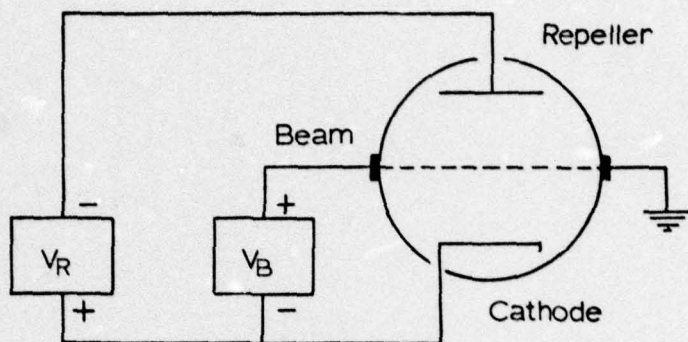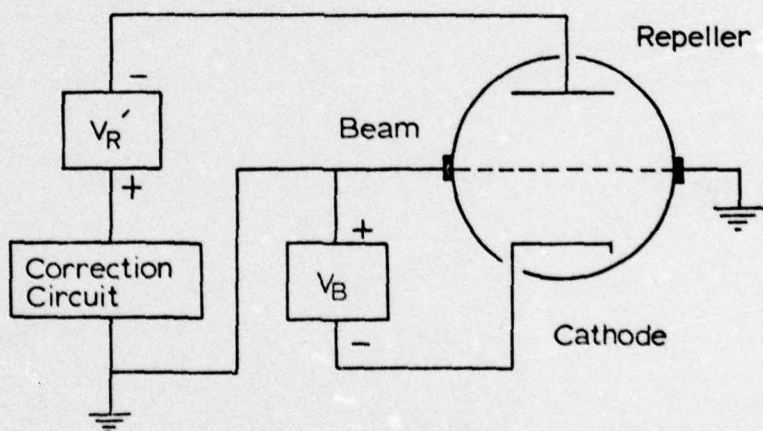

(b) Special Klystron Connections

Figure III-3. Klystron connection configuration for effective linewidth feedback system.

The MicroNow supply was factory modified to provide for conventional operation as in (a) or for operation as in (b). Regulation of the repeller voltage was better than ± 0.01%. Such regulation is extremely important during the nulling operation. The klystron must be tuned manually with the repeller voltage to place the frequency at the very top of the cavity (i.e., at ω_r) while simultaneously adjusting the reference arm attenuator for an accurate null. An accurate null is crucial to the precise determination of f_+ and f_-.

Isolation is needed throughout the microwave circuitry to reduce power reflections from the various impedance mismatches. All isolators in Fig. III-2 are of the resonance type, with isolation factors of 10-20 db. The isolators on either side of the two-position attenuator were found to be particularly critical to proper operation of the system. Directional couplers with 10-20 db coupling coefficients were used for power take-offs for the frequency counter and reference arm because they also provide good isolation. The frequency counter is a Hewlett-Packard model 5340 A, which can directly measure frequencies from 10 Hz to 18 GHz with a maximum resolution of ± 1 Hz. Acquisition time when counting with a resolution of ± 100 Hz is less than 2 sec, and this resolution was used for most of the high field ΔH_{eff} measurements.

Two of the variable attenuators in the circuit of Fig. III-2 are of special importance. The first is the attenuator preceeding the reference crystal which is used to null the crystal outputs. For an accurate null, one must be able to make fine adjustments in the attenuation. The most convenient arrangement was to use two attenuators in series, one for coarse adjustments and one for fine adjustments. The second attenuator of special importance is the two-position attenuator in the cavity arm of the microwave circuit. A Hewlett-Packard model 382 X-band variable attenuator was modified

for this application. Two adjustable aluminum stops were used to restrict
the adjustable attenuation between 0 db and 3 db. Calibration was done with
a microwave power meter. The setting was also compared with that of a
second precision attenuator of the same type which was recently factory cali-
brated.

The cavity assembly will be discussed in the next section. It fits in
a 1.89 inch magnet gap. The magnet is a Varian model V4012A twelve-inch
electromagnet with a model V2100 regulated power supply. The regulation of
the field is better than one part in 10^5. The field is measured using an
F. W. Bell model 660 digital nulling gaussmeter. Relative field values
could be set with four place accuracy.

The signal and reference arms of the microwave system are terminated
with crystal mounts and adjustable shorts which are set to position an
antinode of the microwave electric field at the crystal and thus maximize
the detected power. The crystal detectors consisted of a matched pair of
1N23 diodes with reversed polarity, that is, one diode has a positive out-
put and the other a negative output with respect to ground. The outputs
of these two crystals are summed in the comparing circuit.

A schematic diagram of the comparing circuit is shown in Fig. III-4.
The crystal outputs are applied at inputs A and B. Switches S_1 and S_2 allow
either or both of the crystal voltages to be applied to the summing oper-
ational amplifier OA_1. The amplified signal levels are observed via meter
M_1 and range switch S_4.

During the crystal nulling operation, the gain of amplifier OA_1 can be
increased by means of S_5 while the attenuators in the reference arm are
adjusted to yield a null reading on M_1. For this adjustment, the feedback
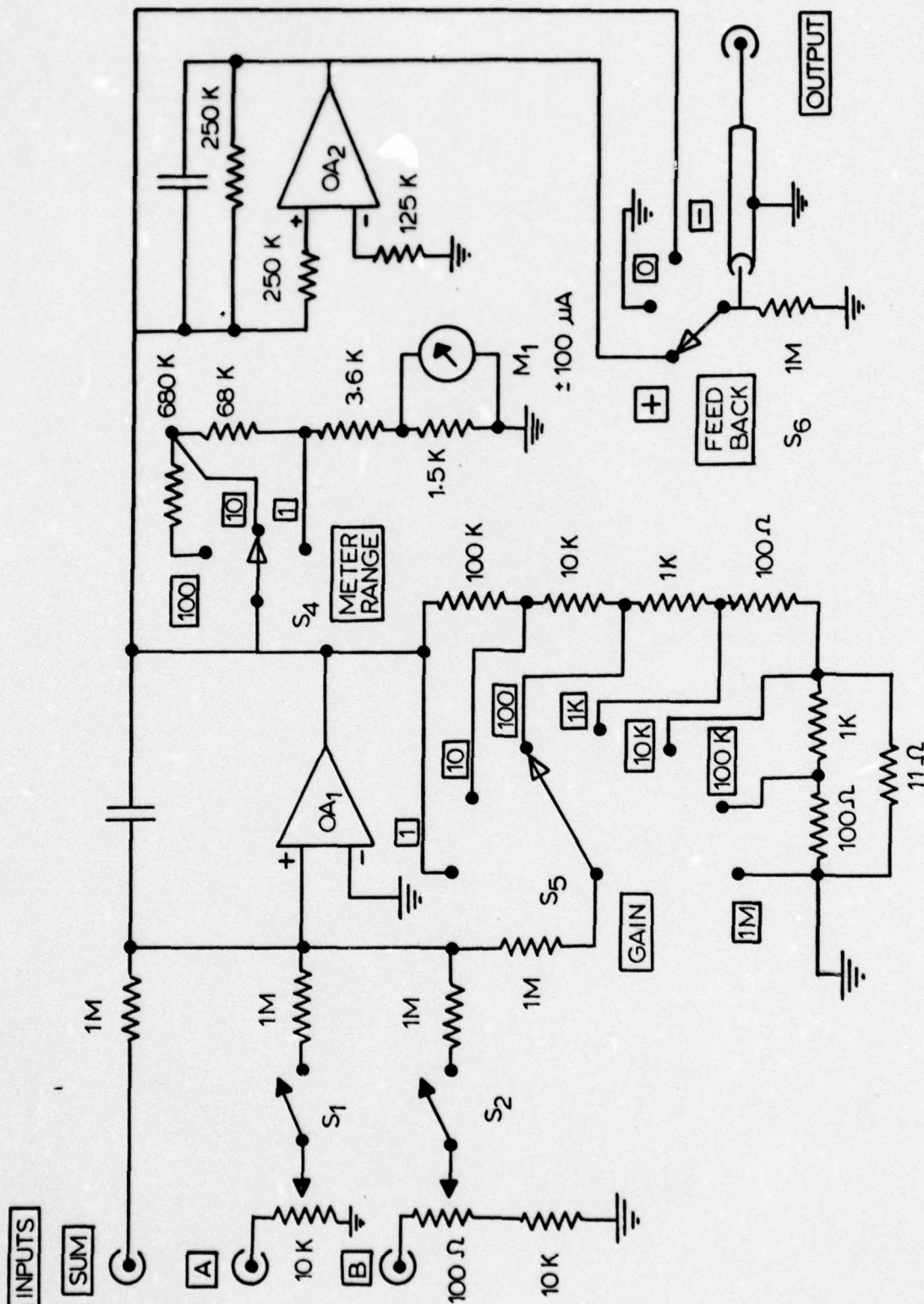switch S_6 is in the off or "0" position, the two-position attenuator is in

Figure III-4. Schematic diagram of comparing circuit (after Kaelberer, 1977).

the 3 db position, and the klystron repeller voltage is adjusted to put
the klystron frequency at ω_r. In practice, one simultaneously adjusts the
fine control on the repeller supply for a minimum (assuming the signal
crystal has negative polarity), and the fine attenuator in the reference
arm to make this minimum fall at zero on M_1. Since the dc gain can be
increased to 10^6, the precision with which the nulling can be accomplished
is limited not by the comparing circuit, but by the ability of the operator
to keep the klystron operating right at the resonant frequency of the
cavity. This ability is limited, in part, by the short term stability of
the repeller voltage.

After the crystal inputs have been nulled as described above, the
system may be locked on to the cavity half power or 3 db points at f_+ or
f_- as follows:

(1) The two-position attenuator is moved to the 0 db position, with
the gain of OA_1 no higher than 1 K.

(2) The feedback switch S_6 is moved to either the "plus" or "minus"
position.

(3) The gain of OA_1 is increased to 1 M. At this stage, the system
is locked onto the appropriate 3 db point of the cavity and $f_\pm$ may be read
directly from the counter. Note that OA_2 is simply a unity gain inverter
to change the sign of the repeller feedback when S_6 is in the "plus" posi-
tion. The 1 MΩ resistor from the pole of S_6 to ground is important for
reasons of safety. It keeps the repeller power supply from floating
dangerously above ground during switching.

Teledyne-Philbrick model 1022 high voltage FET operational amplifiers are
used for both OA_1 and OA_2. These op amps provide a maximum voltage output
swing of $\pm$ 100 V. This wide range is used because the correction voltages

when using low Q wide bandwidth cavities in near-resonance effective

linewidth measurements can be rather large. For the present high field

ΔH_{eff} measurements, the wide range was not needed, since the correction

voltages generated at the output were generally less than $\pm$ 1 V. The wide

range of correction voltage does present a potential problem, however, which

should be noted. It is possible, by having the feedback switched on when

the crystals are not nulled, to generate a feedback voltage which could

push V_R' below V_B (see Fig. III-2). To avoid this possibility, which would

burn out the klystron, care was taken to keep the gain of OA_1 low whenever

the crystals were unbalanced or when S_6 was used to put feedback in or take

feedback out.

The final comments of this section concern the problem of crystal

tracking. During the course of a measurement, the power levels at the

crystals will change due to different measuring fields, different sample

temperatures, or frequency shifts of the klystron. It is important, there-

fore, to ensure that the two diodes track each other reasonably well in an

incremental sense. This tracking should be insensitive to small changes in

power. This is the function of the resistive input circuitry for inputs

"A" and "B" in Fig. III-4 which preceeds switches S_1 and S_2. Given average

voltage operating points for the two crystals, the two potentiometers are

adjusted until the null is insensitive to small power level changes for the

system.

E.   MICROWAVE CAVITY ASSEMBLY AND TEMPERATURE CONTROL

In designing the microwave cavity for high field effective linewidth measurements, three requirements must be met. First, a high Q is necessary to measure the small shifts that occur in Q and f at high fields due to the magnetic sample. Second, it is necessary to stabilize the cavity temperature, since small changes in temperature will also shift the cavity frequency. Third, the cavity design must include provisions for varying the sample temperature so that ΔH_{eff} can be measured as a function of temperature. The importance of cavity temperature stability for measurement accuracy led to the adoption of a design in which the cavity was stabilized at 20°C by a temperature regulated water jacket, and the sample temperature was controlled by a Varian gas flow type temperature regulator. The Q was optimized by using a cavity in the cylindrical TE_{011} mode, constructing the cavity of OFHC copper, and keeping the irises as small as possible.

Figure III-5 shows a cross section of the cavity, approximately at full scale. The cylindrical axis is vertical in the figure. The various parts of the cavity are enumerated in Table III-1. The cavity proper is 38.1 mm long and 39.88 mm in diameter (inside dimensions) and is formed by the cavity body (part A) and the cavity cover plate (part B). The cavity is made of OFHC (oxygen free high conductivity) copper; the high electrical conductivity of the material contributes to the high Q (Q $\sim$ 25000) of the finished cavity. The input and output irises are located oppositely, centered on the curved faces of the cavity body. The diameter of both irises is 3.97 mm.

Standard $\frac{1}{2}$" x 1" X-band copper waveguide (C) is soldered into the cavity body. The thickness of the cavity wall at each iris is 0.762 mm where the waveguides are joined. The outer ends of the waveguide sections
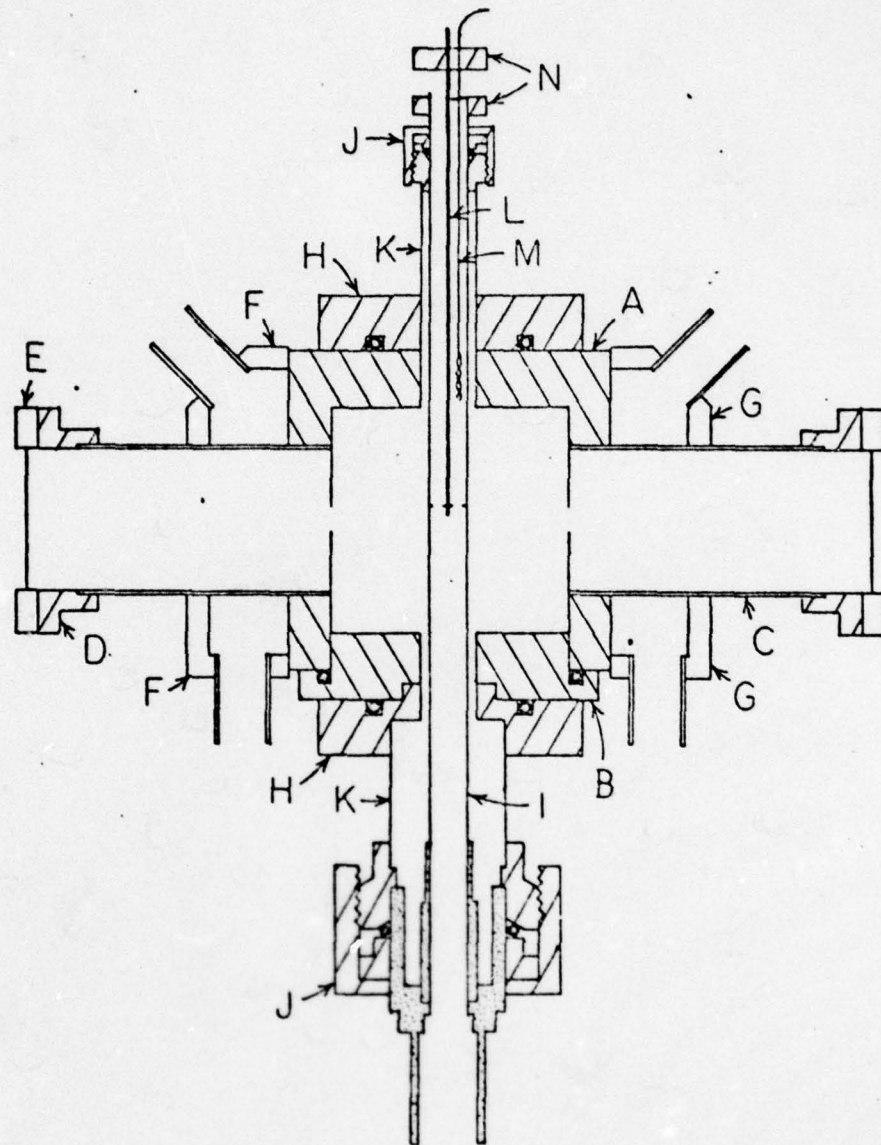
Figure III-5. Cross section of the TE_{011} high Q OFHC copper cylindrical cavity used to study the temperature dependence of the high field effective linewidth (after Kaelberer, 1977).

TABLE III-1. Cavity Components and Materials.

Label in Fig. III-5	Description	Material
A	Cavity body	OFHC copper
B	Cavity cover	OFHC copper
C	Waveguide	copper
D	UG-39/U flange	brass
E	Pressure window	quartz
F,G	Water manifold	plexiglass
H	Sample tube support assembly flange	brass
I	Sample tube	rexolite
J	Quick-connect fitting	brass
K	Thermal isolation tube	stainless steel
L	Sample rod	rexolite
M	Thermocouple	copper-constantan
N	Positioning block	brass

are soldered to UG 39/U flanges, indicated by D. The cavity is supported between the pole caps of the magnet by the waveguide.

To stabilize the temperature of the cavity, a water-jacket arrangement is used on the two sides of the cavity from which the waveguide sections emerge as indicated by F and G in the figure. The manifold is supplied with water at 20°C by the system shown in Fig. III-6. The system has three basic elements: the temperature control unit, a large thermally isolated reservoir, and the cavity manifolds.

The circulator is a Lauda model K-2/R constant temperature circulator. It contains a refrigeration section which allows the temperature of the circulating liquid to be controlled down to -10°C. A heater in the circulator is connected to the control unit. It reheats the liquid when necessary to keep the temperature in the desired range. With the heater alone, temperatures up to 150°C can be obtained. The control regulation of the system is better than ± 0.02°C. The unit also contains a pump to circulate the water through the external system.

Water from the circulator enters a 15ℓ sealed vacuum storage dewar. This dewar serves as a reservoir to smooth out the short term water temperature fluctuations generated by the 5 second control loop of the circulator. Water from the top of the reservoir is forced through the cavity manifolds connected in series, and then flows back to the circulator unit. All parts of the water circuit are thermally insulated; the water flows through insulated foam tubing connecting the three subsystems. The total length of the tubing is about 8 m. The remaining four sides of the cavity are also insulated: 1.59 mm of foam separates the cavity from the pole faces of the magnet, and foam insulation is packed around the sample tube assembly and water connections shown in Fig. III-5.
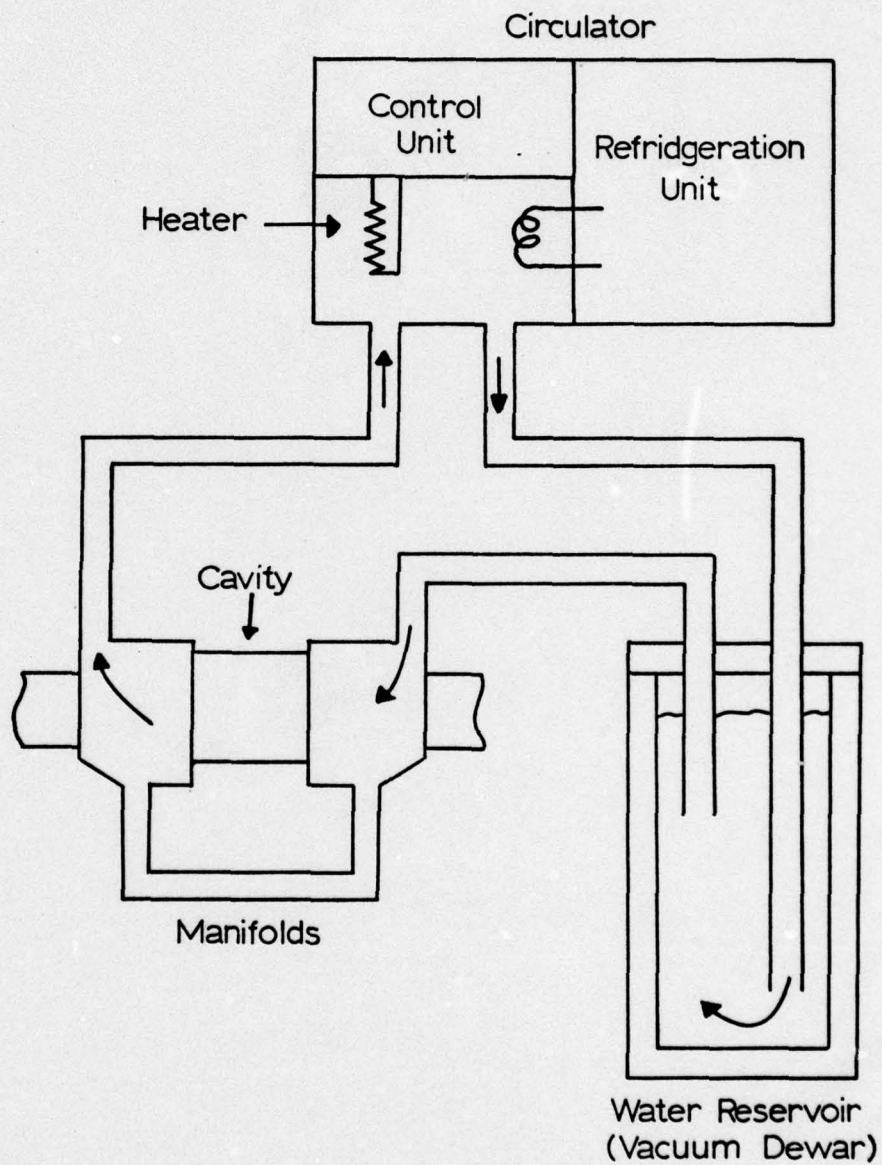
Figure III-6. Water stabilization system for cavity
temperature control at 20°C (after
Kaelberer, 1977).

The cavity can be operated at any temperature between 0°C and 100°C. However, the best temperature is that of the immediate environment of the cavity, which is about 20°C. When the temperature of the cavity changes, the internal dimensions change and shift the cavity frequency by about 1.5 kHz/0.01°C for the present OFHC cavity. It was found that, with the circulator connected directly to the cavity and bypassing the reservoir, the frequency fluctuates by about 2 to 3 kHz with a 5 sec. period. This period corresponds to the on-off cycle time of the heater in the circulator. The magnitude of the frequency change corresponds to a temperature change of 0.02°C, which is consistent with the regulation of the circulator. With the reservoir connected between the circulator and the cavity manifolds, the short term fluctuations in frequency were reduced by a factor of 10. The long term drift was on the order of 300 Hz/minute.

The third requirement is that there be provisions for varying the sample temperature. This requirement was met by placing the sample in a tube which passes through the cavity axis. By flowing a temperature regulated helium-nitrogen gas mixture through the tube, the sample temperature is maintained at the desired value. The details of the mechanical arrangement are evident from Fig. III-5.

To minimize heat flow from the cavity environment to the cooling gas, the cavity is evacuated and the sample tube-cavity connections are made with stainless steel tubing, labeled K in Fig. III-5. These tubes are attached to the cavity by the o-ring sealed flanges labeled H. The outer ends of the tubes are soldered to the quick-connect fittings labeled J. The access holes in the cavity are 9.53 mm diam, as in the top stainless steel tube. The botton tube is 19.05 mm diam. The flange H, tube K, and fitting J make up the sample tube support assembly. These two assemblies are removable to facilitate modifications.

To maintain a vacuum within the cavity, the two sample-tube support assemblies are fitted to the cavity with o-ring. At the ends of the wave-guide sections, pressure windows (labeled E) are fitted to the flanges with a grease seal. Finally, the quick-connects labeled J seal to the sample tube I with o-rings. The cavity, connecting waveguides, and stainless steel support tubes are then evacuated by a mechanical pump.

The sample tube I in Fig. III-5 is made of Rexolite, a microwave dielectric supplied by Atlantic Laminates, 174 N. Main Street, Franklin, New Hampshire, 03235. The material is optimum in this application because of its rather low dielectric constant, about 2.5, as well as its low micro-wave loss. The low dielectric constant is important because the sample tube must pass through the cavity in a region where the microwave electric field is nonzero. Any dielectric will tend to degrade the pure TE_{011} mode and hence lower the Q. The use of the Rexolite sample tube, machined down to 6 mm o.d. with a 1.59 mm-2.38 mm wall, minimizes this degradation and keeps the cavity Q well above 20,000. At the bottom of the sample tube, various sizes of Rexolite rod, machined and epoxied together, form the portion which is shaded in Fig. III-5. This design isolates the sample tube somewhat from the rubber o-ring seal in the bottom quick-connect. This helps to prevent the seal from freezing during low temperature operation. At the top of the cavity, such isolation is not possible. Temperatures as low as 100°K have been achieved without freezing either o-ring seal. If the tube is cooled or heated too quickly, however, the o-rings do begin to leak.

The sample is inserted down the sample tube from the top. For ferrite test sample spheres, on the order of 2-3 mm in diam., the samples are simply glued on the end of a 1 mm Rexolite rod which is extended down into

the sample tube. The rod has a three-spoke spacer disk which centers the rod and the sample in the tube. The sample rod is secured by a brass collar, labeled N in Fig. III-5, to achieve proper, reproducible positioning of the magnetic sample in the cavity.

The flow of temperature regulated cooling gas is provided by means of a Varian variable temperature accessory normally used in conjunction with EPR systems. Figure III-7 diagrams the essential components of the system. A mixture of about 10% helium gas and 90% nitrogen gas flows into a cooling dewar containing liquid nitrogen. The mixture avoids liquification of the gas in the cooling coils. The gas, then at about 77°K, flows through an insulated gas flow tube, past a heater coil and sensor, and then into the Rexolite sample tube. The sensor and heater are connected to the Varian control unit and serve to maintain the temperature at a value set on the dial of the control unit.

The only essential modification of the Varian system is that the sample tube is coupled to the end of the insulated gas flow tube. That quartz gas flow tube could not be directly inserted into the cavity, as it is the Varian EPR system, because the degradation in the Q was simply too great. Because of unavoidable heat leaks, the longer gas flow path from the sensor to the sample, and the less-than-optimum thermal isolation of the Rexolite tube from the cavity environment at 20°C, the sample temperature is about 10° warmer than the dial indication on the Varian unit. This differential is also a function of the gas flow rate and the temperature.

The sample temperature is monitored by a copper constantan thermo-couple, labeled M in Fig. III-5. The junction is positioned just above the inside of the cavity so as not to disturb the cavity fields. The
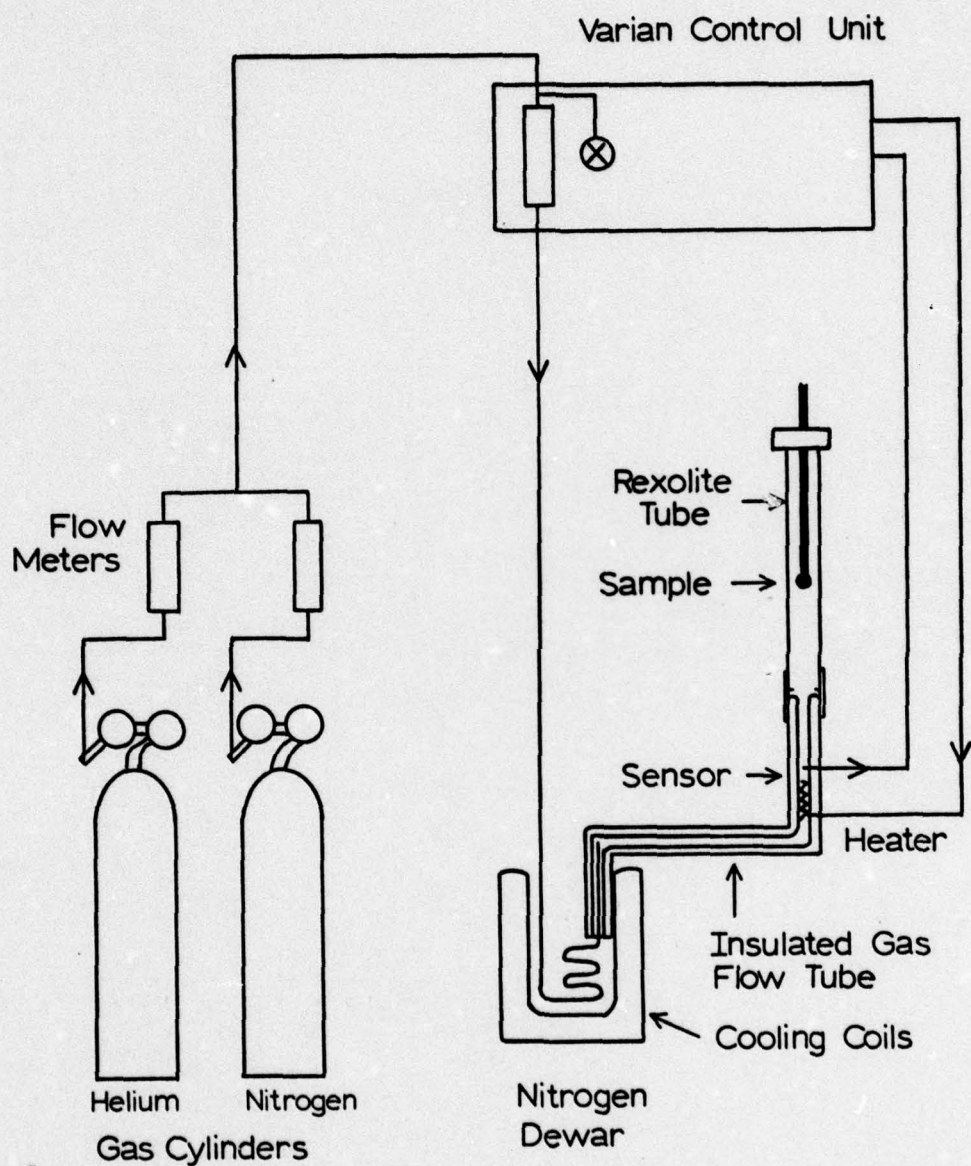
Figure III-7. Gas flow sample temperature control system for high
field effective linewidth measurements.

thermocouple reference junction is immersed in the 20°C water bath of the K-2/R circulator. Comparison of the thermocouple readings with those from a thermocouple placed at the sample location in the center of the cavity indicate that the sample is about 2° cooler than the measured value just outside the cavity, for the lowest temperature attained. In actual operation, it was found that higher gas flow rates were needed for lower temperatures. Regulation to within a few degrees during the course of a single temperature run (10-20 min) was routinely possible.

CHAPTER IV

THE SPIN-WAVE LINEWIDTH TECHNIQUE

A.   INTRODUCTION

High power effects in ferrites are based on the existence of coupling between any microwave field acting on the material and the spin-wave modes. The simplest such effect is termed parallel pumping. In typical parallel pumping experiments, a linearly polarized microwave field is applied parallel to the static field. Because of the volume dipolar interaction, spin-waves propagating in any direction other than parallel to the static field ($\theta_k = 0°$) are elliptically polarized. For such spin waves, the z-component of the magnetization has a dynamic component at twice the spin precession frequency. It is this component that couples to the parallel pump polarization field. The subject is discussed extensively by Sparks (1964) and Patton (1975).

The present chapter is intended to serve as a brief introduction to the basic concept of spin-wave instability processes and the spin-wave linewidth technique. Chapter V will describe the measurement system developed under the ARO grant.

B. SPIN-WAVE INSTABILITY PROCESSES

The basic idea of spin-wave instability processes is quite simple.
Assume a bath of spin-wave states excited to their thermal level. The
available magnon states obey the dispersion law

$$\omega_k/\gamma = \left[(H_i+Dk^2)(H_i+Dk^2 + 4\pi M_o Sin^2\theta_k)\right]^{\frac{1}{2}} , \qquad (IV.1)$$

where ω_k is the spin-wave frequency, H_i is the static internal field,
D is an exchange parameter on the order of 5×10^{-9} Oe-cm^2, k is the spin-
wave wave number, and θ_k is the angle between $\bar{k}$ and the applied field.
If a microwave pump field is applied at ω, this field can couple to the
z-component of the dynamic magnetization of spin-waves at $\omega_k = \omega/2$. The
effect of this pump field will be to increase the magnon occupation numbers
of the available spin-waves <u>above</u> their thermal statistical values. If the
power level is small, the pumped modes will relax back to thermal amplitudes
as fast as they are pumped. At some critical power level, the power input
to the modes will exceed the rate at which energy can be lost due to relaxa-
tion and some spin-wave amplitudes will begin to increase beyond their thermal
values. The power into any spin-wave mode is proportional to some coupling
coefficient P_k multiplied by the mode occupation number N_k. The power
out of the mode due to relaxation, given by the usual transition probability
formula, is proportional to $\eta_k \cdot (N_k - \bar{N}_k)$, where η_k is the spin-wave
relaxation rate and $\bar{N}_k$ is the thermal equilibrium occupation number. The
time dependence of N_k for this energy flow situation is

$$N_k \propto e^{\kappa t} \qquad (IV.2)$$

with

$$\kappa = P_k - \eta_k \,. \tag{IV.3}$$

If P_k exceeds η_k, κ is positive and the mode occupation number grows exponentially. The microwave field amplitude at which $P_k = \eta_k$ is satisfied is the spin-wave instability threshold field h_c. Of course, the mode amplitude cannot increase indefinitely. At some point the amplitude is limited by other interactions. From the theory of Morgenthaler (1960) and Schlömann, et al. (1960), one obtains

$$h_c = (\omega/\omega_m) \, \Delta H_k / Sin^2 \theta_k \tag{IV.4}$$

where

$$\Delta H_k = 2\eta_k/\gamma$$

expresses the spin-wave relaxation rate in linewidth units, analagous with $\Delta H_{eff} = 2\eta_o/\gamma$ for the effective linewidth. The quantity ΔH_k is termed the spin-wave linewidth.

The experimentally observed threshold field h_{crit} is the minimum value of h_c when all the available spin-waves at $\omega_k = \omega/2$ are considered. From Eq. (IV.1), it is clear that all θ_k values are available if the static internal field H_i is less than a critical value

$$H_c = [(2\Pi M_o)^2 + (\omega/2\gamma)^2]^{\frac{1}{2}} - 2\Pi M_o. \tag{IV.5}$$

In this field region, $0 < H_i < H_c$, the minimum threshold is for $\theta_k = 90°$. This is intuitively reasonable, since spin-waves propagating at right angles to the static field direction have the largest dipolar induced ellipticity and hence the strongest parallel pump coupling. If the static internal field exceeds $H_\infty = \omega/2\gamma$, there are no available spin-wave states and h_{crit} is infinite. For $H_c < H_i < H_\infty$, the minimum threshold is for the largest

available θ_k value at $\omega_k = \omega/2$. This θ_k^{max} is specified by

$$Sin^2 \theta_k^{max} = (\omega/2\gamma)^2 - H_i^2)/(H_i - 4\pi M_b) . \qquad (IV.6)$$

Note that the k-value of the minimum threshold spin-wave is given by

$$k^2 = (H_c - H_i)/D \qquad (IV.7)$$

for $H_i < H_c$, and $k \approx 0$ for $H_c < H_i < H_\infty$.

In a typical experiment, the ferrite sample is biased at a sequence of static field values from $H_i = 0$ to $H_i = H_\infty$. At each field one measures the sample susceptibility χ'' as a function of the microwave field amplitude h_{rf} at the sample position. As long as the power level is below threshold, $h_{rf} < h_{crit}$, the value of χ'' is very small, corresponding to that expected for a sample biased far below resonance with a microwave pump parallel to the static field. As h_{rf} exceeds h_{crit}, one observes an abrupt increase in χ''. The break point for properly calibrated data is taken as an empirical determination of h_{crit}. When h_{crit} is measured as a function of the static field, one obtains what is commonly called a "butterfly curve". The term arises because the early data on single crystal YIG resembled the profile of butterfly wings. The data for $H_i < H_c$ may be used to calculate the spin-wave linewidth ΔH_k as a function of wave-number k. As will be discussed more extensively in   Chapter VII, the k-dependence of the spin-wave linewidth provides important clues to the physical relaxation process or processes responsible for η_k.

C.   MICROWAVE CAVITY PARAMETERS

The central experimental problem is to arrange a microwave system so that measurements of χ'' versus h_{rf} can be made accurately and easily. In practice, the measurements are based on microwave perturbation theory. The samples for high power measurements are generally smaller than those needed for ΔH_{eff} and a straightforward application of perturbation theory is adequate. One usually calibrates the microwave power source so that the power incident on the cavity P_{inc} is known. This power parameter can be used to calculate h_{rf} at the sample position. The usual procedure is to measure the reflection coefficient Γ as a function of the incident power P_{inc}. The measured Γ is then used along with other power independent cavity parameters to calculate χ''. The threshold field h_{crit} is then simply read off of a plot of χ'' versus h_{rf}. The entire procedure is repeated at each field of interest to obtain a butterfly curve of h_{crit} versus H_i. It is seen that a large number of tedious measurements is required. In some situations, the measurement system can be automated to some degree (Patton and Green, 1971).

The relationships between the measured parameters Γ and P_{inc}, and the desired parameters χ'' and h_{rf} are determined by the type of cavity and the location of the sample within the cavity. For the work reported here, a rectangular TE_{101} reflection cavity was used. The sample was mounted approximately one sample diameter above the cavity bottom. At this location, the sample was nearly at the maximum microwave magnetic field, but was far enough from the cavity bottom to avoid sample imaging effects.

The relationships between χ'' and h_{rf}, and Γ and P_{inc} contain the loaded Q of the cavity

$$Q_L \equiv \frac{\omega E}{P_t} \tag{IV.8}$$

where ω is the frequency in radians per second, E is the energy stored in the cavity, and P_t is the total power dissapated in the cavity, the sample, and the iris. From the definition of P_t it follows that

$$\frac{1}{Q_{Lo}} = \frac{1}{Q_c} + \frac{1}{Q_i} , \tag{IV.9}$$

and

$$\frac{1}{Q_{Ls}} = \frac{1}{Q_{Lo}} + \frac{1}{Q_s} , \tag{IV.10}$$

where Q_c, Q_i, and Q_s are the effective Q values which represent the losses connected with the cavity walls, the iris, and the sample, respectively. Thus, Q_{Lo} is the loaded Q of the cavity without a sample present and Q_{Ls} is the loaded Q of the cavity with a ferrite sample present. These two Q values may be related to the corresponding reflection coefficients Γ_s for the cavity-with-sample and Γ_o for the cavity-without-sample,

$$Q_{Ls} = Q_{Lo} \left(\frac{1 \pm 10^{-\Gamma_s/20}}{1 \pm 10^{-\Gamma_o/20}} \right) \tag{IV.11}$$

The (+) and (−) signs in Eq. (IV.11) refer to over- and under-coupled cavities, respectively. Note that Q_{Lo} and Γ_o are constant cavity parameters, independent of the sample properties or microwave power level. The Q_{Ls} and Γ_s values, in contrast, will vary with sample properties and power.

In obtaining the needed expressions for the increase in χ'' from the low power below threshold value, $\Delta\chi''$, and the microwave field amplitude h_{rf} at the sample position, as a function of the incident microwave power on the

cavity P_{inc}, it is important ot remember that the measured parameter is Γ_s versus P_{inc}. The perturbation theory result for χ'' in Chapter II yields $\Delta\chi''$ directly in terms of the appropriate Q values,

$$\Delta\chi'' = \frac{2V_c g}{V_s}\left(\frac{1}{Q_{Ls}} - \frac{1}{Q_{Ls}^{max}}\right) , \tag{IV.12}$$

where Q_{Ls}^{max} is the loaded Q of the cavity-with-sample when the power level is <u>below</u> <u>threshold</u> and Q_{Ls} is the loaded Q of the cavity-with-sample at any specific power level. Below threshold, $Q_{Ls} = Q_{Ls}^{max}$ is satisfied and $\Delta\chi''$ is zero. Above threshold, Q_{Ls} decreases due to the nonlinear effects discussed in Section III.B, and $\Delta\chi''$ increases. For a rectangular cavity, as used in the high power spectrometer, the g parameter from perturbation theory is given by

$$g = \frac{1}{8}\left[1 + (\ell/a)^2\right] , \tag{IV.13}$$

where ℓ is the cavity length and a is the cavity width. In terms of the cavity reflection coefficients, $\Delta\chi''$ is given by

$$\Delta\chi'' = \pm\frac{2V_c g}{V_s}\left(\frac{1 \pm 10^{-\Gamma_o/20}}{Q_{Lo}}\right) \times$$

$$\left[\frac{10^{-\Gamma_{Ls}^{\ell o}/20} - 10^{-\Gamma_{Ls}/20}}{(1 \pm 10^{-\Gamma_{Ls}/20})(1 \pm 10^{-\Gamma_{Ls}^{\ell o}/20})}\right] . \tag{IV.14}$$

Here, Γ_{Ls} is the measured cavity reflection coefficient (in db) at a particular power level, $\Gamma_{Ls}^{\ell o}$ in the measured reflection coefficient (in db) at very low power levels below threshold, and the ($\pm$) signs are for over- and under-coupled cavities respectively.

The microwave magnetic field amplitude at the sample position h_{rf} is related to the energy stored in the cavity E_c by

$$h_{rf}^2 = 4\pi E_c / g V_c , \tag{IV.15}$$

and E_c is directly related to the loaded Q of the cavity, Q_{Ls}.

$$E_c = \frac{Q_s Q_c}{Q_s + Q_c} \left(\frac{P_c + P_s}{\omega} \right) \tag{IV.16}$$

Here, P_c is the power transmitted to the cavity,

$$P_c + P_s = P_{inc} (1 - 10^{-\Gamma_{Ls}/10}). \tag{IV.17}$$

Thus, measurement of P_{inc}, Γ_{Ls}, and Q_{Ls} lead directly to the determination of h_{rf}. This analysis, while straightforward from the above equation, is not satisfactory in terms of the measurement procedure because only Γ_{Ls} is measured as a function of P_{inc}. The loaded Q of the cavity-with-sample, Q_{Ls}, is not measured explicitly. It would be better to have an explicit relational expression between h_{rf} and Γ_{Ls} in which no other parameters depend on P_{inc}. This is easily obtained by use of Eqs. (IV.9 - IV.11)

$$h_{rf}^2 = \left[\frac{8\pi}{\omega g V_c} \frac{Q_{Lo}}{1 \pm 10^{-\Gamma_o/20}} \right] \left[\left(1 - 10^{-\Gamma_s/20} \right) \left(1 \pm 10^{-\Gamma_s/20} \right) \right] \cdot P_{inc}. \tag{IV.18}$$

As before, the ($\pm$) are for over- and under-coupled cavities, respectively. The first square-bracket-term contains the constant cavity-without-sample parameters, while the second square-bracket-term contains the measured cavity reflection coefficient.

The spin-wave instability threshold h_{crit} is determined from a plot of $\Delta\chi''$ vs. h_{rf}. Typical data are characterized by a low-power baseline region in which $\Delta\chi''$ is independent of h_{rf}, and a high-power linear region in which $\Delta\chi''$ is proportional to h_{rf}. The threshold field h_{crit} is determined from such a plot, as the microwave field at which the extrapolation of the high-power linear portion of the curve intersects the low-power baseline.

The above analysis provides the working equations to obtain h_{crit} and ΔH_k from data of cavity reflection coefficient as a function of incident power. The details of the measurement system are described in Chapter V.

CHAPTER V

SPIN-WAVE LINEWIDTH SPECTROMETER FOR

THE TEMPERATURE RANGE 88-368 K

A.   INTRODUCTION

The previous chapter describes a procedure by which measurements of

the reflection coefficient as a function of incident power for a microwave

cavity containing a magnetic sample can be used to obtain the spin-wave

linewidth.   This chapter will describe the spin-wave linewidth spectrometer

which was developed under the ARO grant.

The initial need to establish a spin-wave linewidth system quickly and

cheaply has resulted in the development of an inexpensive pulsed high-power

microwave spectrometer with variable temperature capability.   The high-

power source utilizes a suitably adapted MIT Model 3 *hard-tube pulse modulator*

which is inexpensively available on the surplus market.   The temperature

control system allows the sample temperature to be maintained at any tem-

perature between 88 K and 368 K.   The cavity temperature remains fixed at

77 K, independent of the sample temperature.   This is very desirable since

it renders the cavity parameters Q_{Lo} and Γ_o independent of sample temperature.

The microwave measurement system is functionally described in Section V.B.

This section also includes descriptions of the microwave calibration and

measurement procedures.   Section V.C. covers the details of the microwave

measurement system components.   The temperature control system for the

cavity is functionally described in Section V.D.   Instrumentation details

are provided in Section V.E.

B. MICROWAVE MEASUREMENT SYSTEM

The microwave measurement system consists of a reflection spectrometer which may be driven by a high power pulsed source for the determination of spin-wave linewidth, from data on P_{inc} and Γ_s , or a low power cw source for the determination of the intrinsic cavity, Q, Q_{Lo}.

The spectrometer is shown in Fig. V-1. It consists of three branches: (1) the reference arm, (2) the reflected arm, and (3) the cavity arm. The reference arm is used to monitor the power which is incident upon the cavity. The reflected power arm is used to monitor the power reflected by the cavity arm. It also contains a cavity wavemeter for frequency determination. The cavity arm consists of the cavity and the waveguide shorting switch. The cavity arm may be readily opened in front of the cavity so that the cavity may be replaced by a microwave power meter or a blank iris plate. Additional components provide isolation and easy power level adjustment at appropriate points in the system.

A block diagram of the low power source appears in Fig. V-2. The source consists of a klystron and klystron power supply; and a frequency stabilization system comprised of the klystron stabilizer and repeller voltage correction box. The system also contains a frequency counter for determination, with the klystron frequency locked to the stabilizer, of the klystron output frequency.

Figure V-3 is a block diagram of the high power source. Twenty killowat pulses are produced by the magnetron, which is driven by the pulse modulator. The modulator is powered by the high frequency 115 V ac supply and the 24 V dc supply. It is triggered by the pulse generator. The magnetron is isolated from the load by an isolator. The attenuator is included to reduce the output power to a level which will not damage components of the microwave spectrometer. The microwave pulses can be diverted into a dummy load, with the
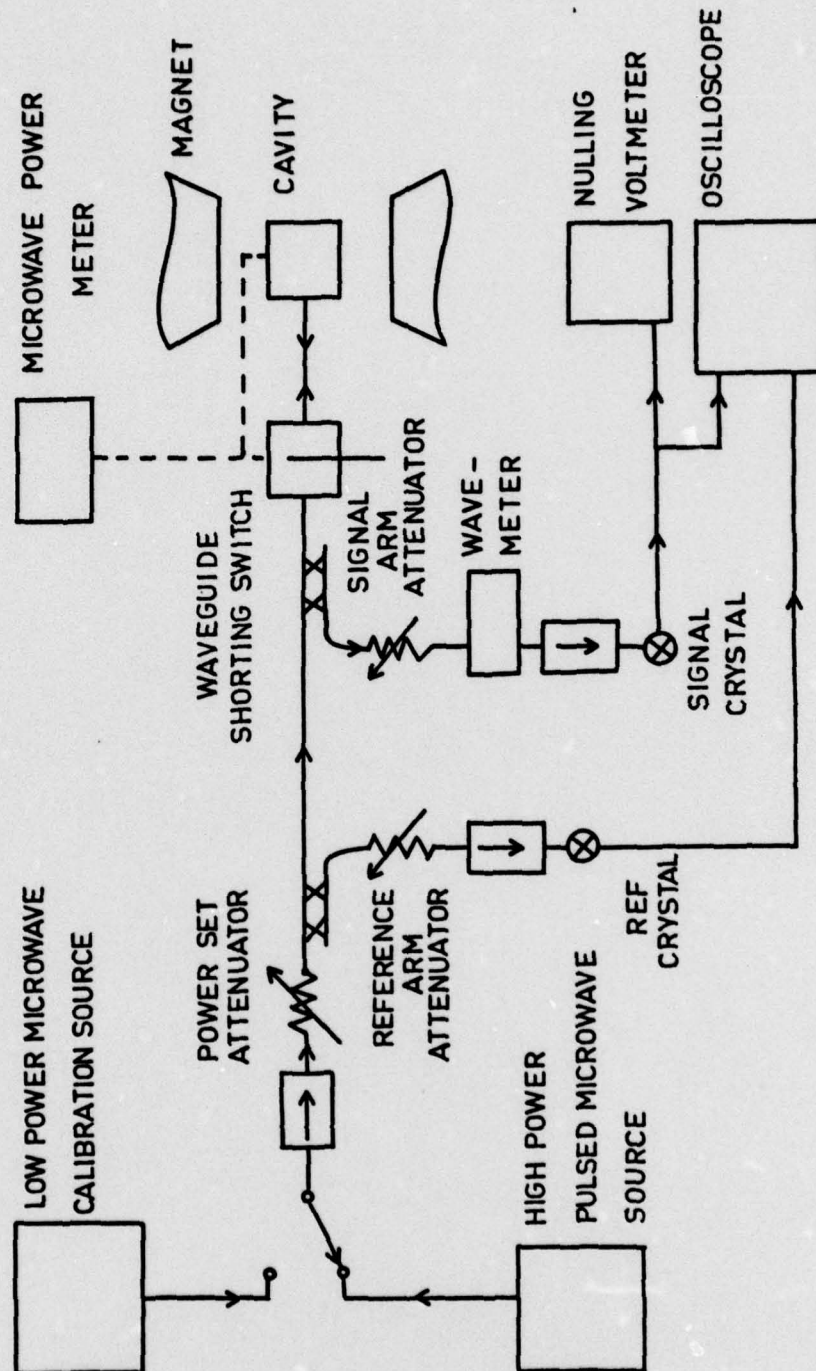
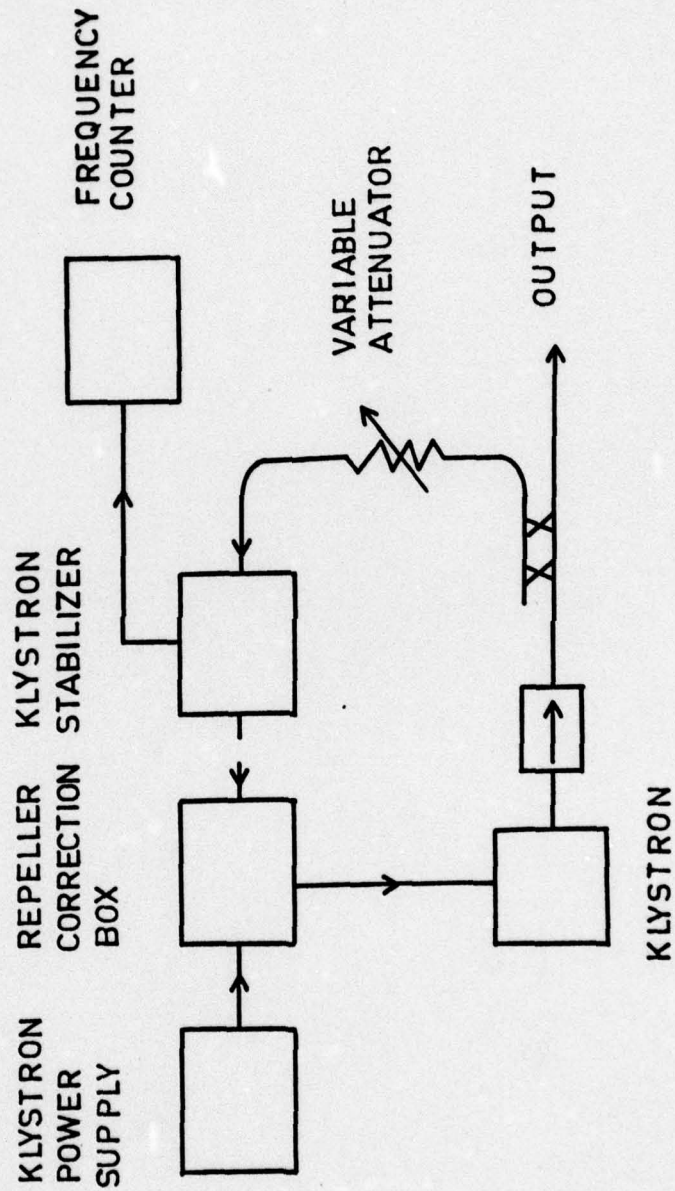Figure V-1. Block diagram of the reflection spectrometer.

54

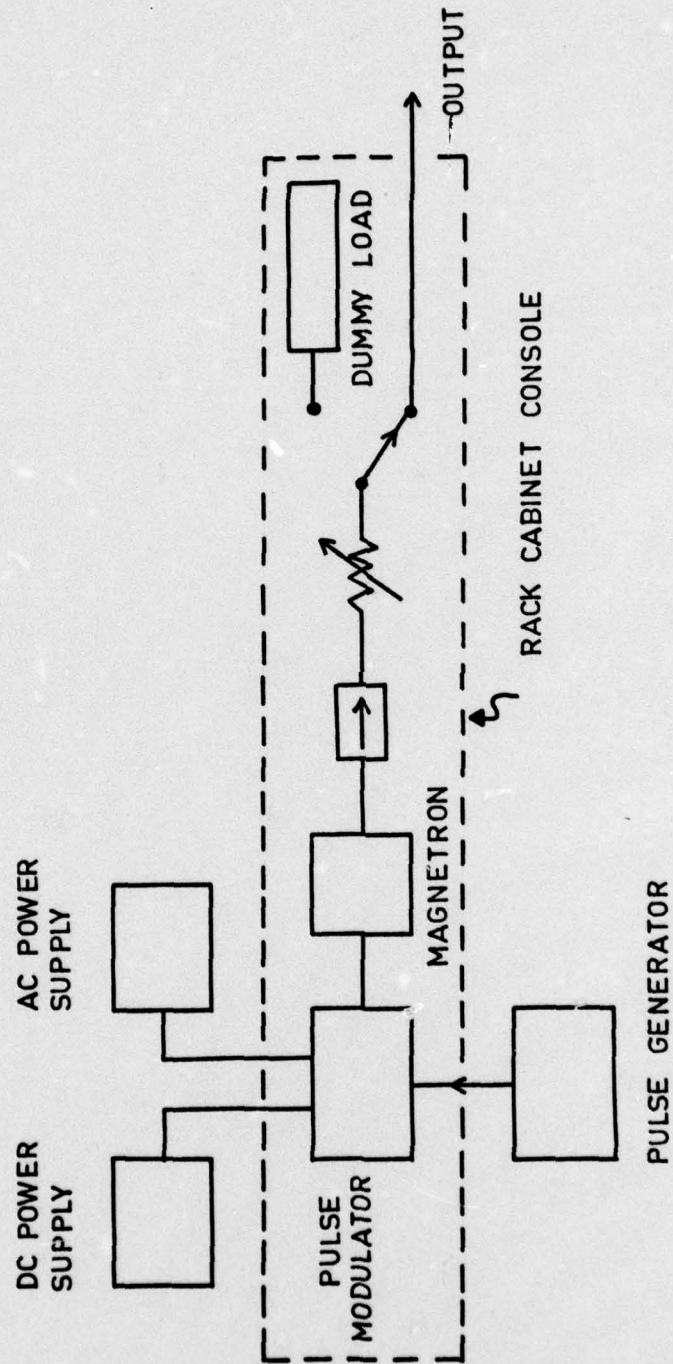Figure V-2. Block diagram of low power-source.

Figure V-3. Block diagram of the high power pulsed microwave system.

microwave dump switch. This allows the spectrometer to be opened up with the high power source in operation.

As described in Chapter IV, the spin-wave instability threshold h_{crit} as a function of static field may be obtained from data on (1) the intrinsic cavity-without-sample parameters Q_{Lo} and Γ_o, and (2) data on the cavity-with-sample reflection coefficient, Γ_s, as a function of the incident power at the various static field values of interest. The following paragraphs describe the specific procedures by which Q_{Lo}, Γ_o, and Γ_s versus P_{inc} are obtained.

The Q_{Lo} and Γ_o parameters are measured with the cavity empty. The cavity temperature is held at 77 K by the system to be described in a later section, and the cavity is evacuated to below one Torr. The Q_{Lo} is, in theory, specified from the determination of the cavity half-power frequencies f_+ and f_- as discussed in Chapter III. For a reflection cavity, the simplest procedure is to tune the klystron to these half-power points by monitoring the cavity reflection coefficient, measure f_+ and f_-, and determine Q_{Lo}. The reflection coefficient at the two half-power points is given by

$$\Gamma_{\frac{1}{2}} = \left[3 - 10 \cdot \log \left(1 + 10^{-\Gamma_o/10} \right) \right] \text{(in db)}, \qquad (V.1)$$

where Γ_o is the cavity-without-sample reflection coefficient (in db) at the cavity center frequency. These measurements are most easily done cw, utilizing the spectrometer with the low power source.

The procedure to determine Γ_o is as follows:

(1) The cavity center frequency is found as that which gives a minimum output of the reflected arm crystal as indicated on the nulling voltmeter.

(2) The klystron frequency control is transferred to the frequency stabilizer where it will remain through the measurement.

(3) The reflected arm precision attenuator is set at 0 db and the nulling voltmeter internal reference is adjusted so that the reflected arm crystal output gives a null reading. Let this reference voltage be defined as V_o. The reflected crystal voltage versus frequency and the operating point "A" at the center frequency f_o and voltage V_o are shown in Fig. V-4(a).

(4) The cavity with its nonremovable iris is disconnected from the system and replaced by a blank iris plate of the same material as the cavity iris. This is to provide a reference incident power corresponding to point "B" in Fig. V-4(a).

(5) The reference arm attenuator is adjusted such that a null reading is again obtained on the voltmeter. The attenuation indicated on the precision attenuator is the cavity-without-sample reflection coefficient Γ_o, in db. This amount of attenuation has, in effect, moved point "B" in Fig. V-4(a) down to "A". In practice, it is wise to put in some attenuation prior to step (4) above, to avoid biasing the crystal at an excessive power.

With Γ_o thus determined, we may proceed with the repeller adjustments to shift the klystron frequency to the cavity half-power points, as determined by putting the reflection coefficient at $\Gamma_{\frac{1}{2}}$. This adjustment is complicated, in practice, by the variation in klystron power with frequency as indicated by the dotted line in Fig. V-4(a). The complications arise from (1) the need to use a nulling procedure in which all measurements are made at the same crystal voltage (V_o for the Γ_o determination described above), in order to avoid crystal tracking errors, and (2) the use of the blank iris plate to provide the reflected power reference at the frequency of the measurement.

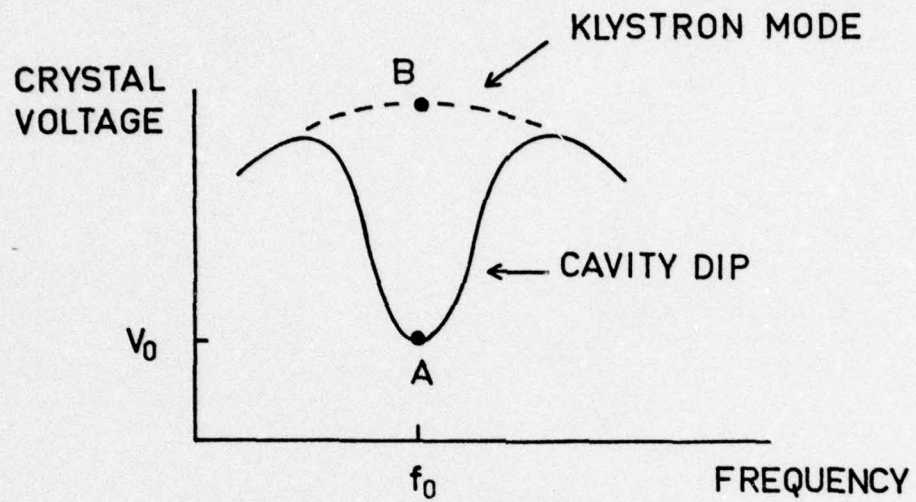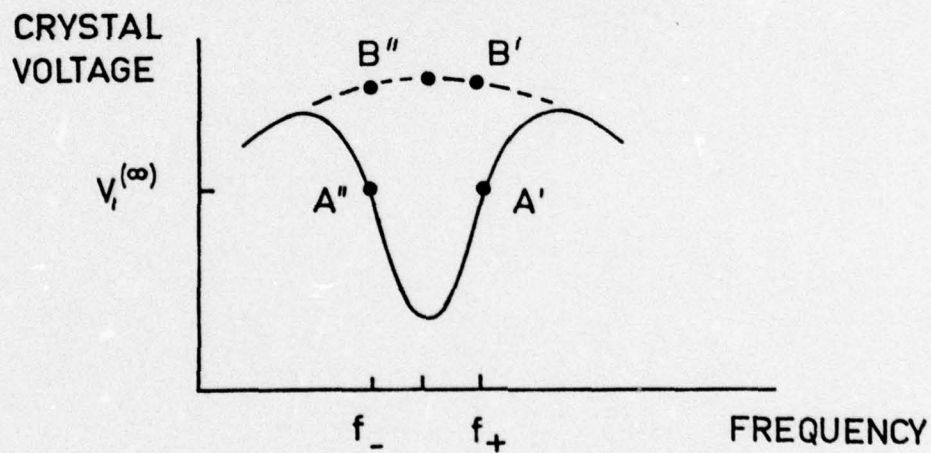The basic procedure is illustrated in Fig. V-4(b). It is essentially

58

Figure V-4. Schematic representation of the reflected power versus frequency for the cavity in place (solid line) and the blank iris plate (dotted line).

the reverse of the Γ_o determination routine, since we know $\Gamma_{\frac{1}{2}}$ and need to set the klystron to f_+ (or f_-). Following the Γ_o operations described above, the attenuator is changed to $\Gamma_{\frac{1}{2}}$ and the nulling voltmeter is reset to null out the crystal voltage at a value V_1. This means that point "B" is attenuated by $\Gamma_{\frac{1}{2}}$ to the reference level V_1. If we were to now (1) reconnect the cavity, (2) set the attenuator to zero, and (3) adjust the reflector voltage for a null on the voltmeter, the klystron frequency would be at f_+ (or f_-). These frequencies could then be measured with the counter and Q_{Lo} determined. However, the variation in incident power with frequency causes points B' and B" to be lower than B, in terms of crystal voltage with the blank iris plate in place. This means that the initial reference setting, based on point B is not quite correct. An iterative procedure is used to accurately determine f_+ and f_-. The procedure is as follows:

(1) Assume that steps (1) – (5) in the Γ_o measurement have been done.

(2) The reflection coefficient $\Gamma_{\frac{1}{2}}$ is calculated by Eq. (V.1).

(3) The reflection arm precision attenuator is set to $\Gamma_{\frac{1}{2}}$ and the voltmeter reference is set to null the crystal voltage. Call this voltage $V_1^{(1)}$.

(4) The cavity is reconnected, and the attenuator is set at zero.

(5) The klystron is now tuned away from f_o, up in frequency or down in frequency for f_+ or f_- determinations, respectively, until a null is again obtained on the voltmeter. At these frequency points, the power reflected from the cavity is $\Gamma_{\frac{1}{2}}$ db down from the power at point "B". If the klystron output were independent of power, these points would correspond to f_+ or f_-. The true half power points are the settings where the reflected power is $\Gamma_{\frac{1}{2}}$ db down from the power levels at B' and B". Thus, the above settings, denoted by $f_+^{(1)}$ and $f_-^{(1)}$, are only

first approximations to the cavity half power points. From here, an iterative scheme is needed to determine f_+ and f_-.

(6) With the klystron at $f_+^{(1)}$ or $f_-^{(1)}$, the cavity is agian replaced by the blank iris plate and the attenuator reset to $\Gamma_{\frac{1}{2}}$.

(7) Because of the power level variation from B to B' or B", the voltmeter will not be at null and a readjustment of the null reference to $V_1^{(2)}$ is required to null the crystal.

(8) The cavity is now reconnected, the attenuator reset to zero, and the repeller readjusted to obtain a null at $f_+^{(2)}$ or $f_-^{(2)}$.

(9) As the above steps (6) – (8) are repeated through several cycles, the $f_+^{(m)}$ and $f_-^{(m)}$ values will converge to the true half power points of the cavity.

While the above procedures to determine Γ_o and $Q_{Lo} = (f_+ + f_-)/2(f_+ - f_-)$ are somewhat tedious, it is to be noted that they need be done only once for a given cavity operating at a given temperature. They can be repeated at timely intervals to check calibration, but need not be done for every sample.

The remaining experimental parameters are just Γ_{Ls} as a function of P_{inc}. These parameters are measured under high power pulsed operation by comparing the power reflected of the waveguide short to that reflected by the cavity. The power meter is used to obtain the absolute power reference. The step-by-step procedure is as follows:

(1) The cavity is evacuated, and the desired sample temperature established.

(2) The magnetic field is set at the desired level.

(3) The pulsed source is tuned to the cavity frequency.

(4) The power measuring head is inserted into the cavity arm, in place of the cavity. The reference arm precision attenuator is set at 0 db. The main power attenuator is adjusted so that the indicated average power corresponds to a peak power of one watt. For square pulses the average power P_{av} and peak power P_{pk} are related by,

$$P_{av} = F \cdot \Delta T \cdot P_{Pk} \qquad \qquad (V.2)$$

Where F is the pulse repetition rate in Hz and ΔT is the pulse width in seconds. The level of the transmitted pulse is noted on the oscilloscope. This will be the power reference level throughout the measurement.

(5) The cavity is reconnected to the cavity arm, and with the shorting switch opened.

(6) With the reflected arm precision attenuator set at 0 db, the reflected pulse is adjusted to a convenient level on the oscilloscope. This will be referred to as the cavity reference level.

(7) The shorting switch is closed and the reflected arm precision attenuator is adjusted to return the reflected pulse amplitude to the cavity reference level on the oscilloscope. The attenuation indicated on the reflected arm precision attenuator is the cavity reflection coefficient in db.

The preceding steps yield one raw-data point (Γ_{db}, P_{inc}) in the butterfly curve. The power may now be increased by increasing the attenuation of the reference arm precision attenuator and decreasing the attenuation of the main power attenuator such that the power reference level is maintained on the reference pulse as indicated on the oscilloscope. The incident power is given in dbw by the attenuation of the reference arm precision attenuator. With the power reset, the next point on the butterfly curve is generated by repetition of steps (3), (6) and (7).

From the intrinsic cavity parameters Γ_o and Q_{Lo}, and Γ_{Ls} versus P_{inc}, plots of $\Delta\chi''$ versus h_{rf} are generated as described in Chapter IV. From these plots, h_{crit} is determined and butterfly curves of h_{crit} versus static field

may be obtained. The spin-wave linewidth ΔH_k may then be calculated from parallel pumping theory.

C. MICROWAVE MEASUREMENT SYSTEM DETAILS

The reflection spectrometer in Fig. V-1 contains three variable atten-
uators. The reference and reflected arms utilize Hewlett-Packard model
X382A precision variable attenuators for the determinations of P_{inc} and
the various reflection coefficient parameters of Section B. They also
contain non-precision variable attenuators to adjust the power levels at
the crystal detectors. Because the reference level for P_{inc} is established
by the precision attenuator in the reference arm, virtually any variable
attenuator capable of 0-30 db attenuation and high pulse power can be used
for the power set attenuator. Two Hewlett-Packard model X375A attenuators
were used here.

Isolation is needed throughout the microwave circuitry to reduce power
reflections from various impedance mismatches. All isolators shown in Fig.
V-1 are of the resonance type with isolation factors of 10-20 db. Directional
couplers with 10-20 db coupling coefficients were used to couple the reflected
and reference arms to the main line, because they also provide good isolation.
The use of a 20 db coupler in the reference arm also ensures minimal loading
of the high power source.

The requirements of the waveguide short differ for cavity calibration,
and for spin-wave linewidth measurement. Both measurements require that
the short be repeatable. However, it is desirable for cavity calibration that
the short approximate the losses of the real cavity iris plate. This is not
important with the measurement of spin-wave linewidth, since the spin-wave
linewidth is derived only from changes in reflection coefficient. Therefore
the short used for cavity calibration consisted of a brass plate soldered
into a UG 39/U waveguide flange. For spin-wave linewidth measurement, a
Hewlett-Packard X930A waveguide shorting switch was found to be satisfactory.

The cavity wavemeter used in the reflected arm is a Hewlett-Packard X532B. It is used to find the harmonic (N of Eq. V.1) of the crystal oscillator when using the low power source. It is also useful in tuning the magnetron to the cavity frequency.

The reflected and signal crystals are 1N23 microwave diodes. They are mounted in Hewlett-Packard X485B tunable detector mounts. These mounts allow the electric field at the crystal to be maximized. Termination of the diodes with 470 Ω resistors was necessary to prevent severe distortion of the pulse shape.

The one watt peak incident power reference level was set using a General Microwave 454A thermolelectric power meter, in conjunction with an X420C thin-film thermocouple detector. The thin-film thermocouple detection system offers lower drift than systems employing thermoresistive detectors. The X420C power head was matched to the line with a Hewlett-Packard X870A slide-screw tuner.

The oscilloscope can be virtually any unit with a dual trace vertical capability. The unit most often used was a Tektronix model 585 with a type 81 adapter and a type CA plug in. Typical settings were .5 mV/div. vertical and 1 μ sec/div. horizontal. For cavity calibration, the reflected arm signal crystal was reconnected from the oscilloscope to a John Fluke model 803BR differential voltmeter.

The D.C. magnetic field was provided by a Pacific Electric Motor model 8A-HI-B 8 inch electromagnet. The magnet was powered by an Alpha Scientific model 3051 power supply. The magnet was used without pole caps, giving a 4" gap in which the cavity and dewar assembly were positioned such that the D.C. magnetic field was parallel to the r.f. magnetic field. The D.C. field at the sample was measured with a Bell model 640 differential gaussmeter. As used with this system, the gaussmeter afforded a minimum field resolution of 5 Oe.

The low power microwave source in Fig. V-2 utilizes a Varian X-13 reflex klystron identical to that described in Section III.D. A resonance type isolator with a 20 db isolation factor is used to isolate the klystron from power reflections. The klystron is powered by a Hewlett-Packard 716B klystron power supply. This supply provides a constant repeller voltage for CW operation. For fm operation, the supply can modulate the repeller voltage with internally generated sawtooth or square waves, or with other externally generated waveforms.

Klystron frequency stabilization can be achieved with the klystron power supply in the cw mode, by feeding a portion of the klystron output back into the microwave ysstems model MOS klystron stabilizer. Here it is mixed with a harmonic of the stabilizer's crystal oscillator, to an intermediate frequency of 40.884 Mhz. The phase of this IF signal is then compared with that of the crystal oscillator. Any phase difference results in a repeller correction voltage of appropriate sign, which is added in the repeller voltage correction box to the repeller voltage of the klystron power supply.

When locked to the stabilizer, the klystron can be tuned by tuning the crystal oscillator of the stabilizer. The klystron frequency is related to that of the crystal oscillator by

$$F = Nf_{osc} \pm 40.884 \times 10^6 \qquad (V.3)$$

where N is the harmonic of the crystal oscillator which is either 40.884 Mhz below or above the klystron frequency. The crystal oscillator frequency is monitored on the Hewlett-Packard 5300A frequency counter.

The pulser and all microwave components related to the high power microwave source of Fig. V-3 are contained in the rack cabinet shown in Fig. V-5. The pulse modulator is mounted upright as shown in in Fig. V-6.
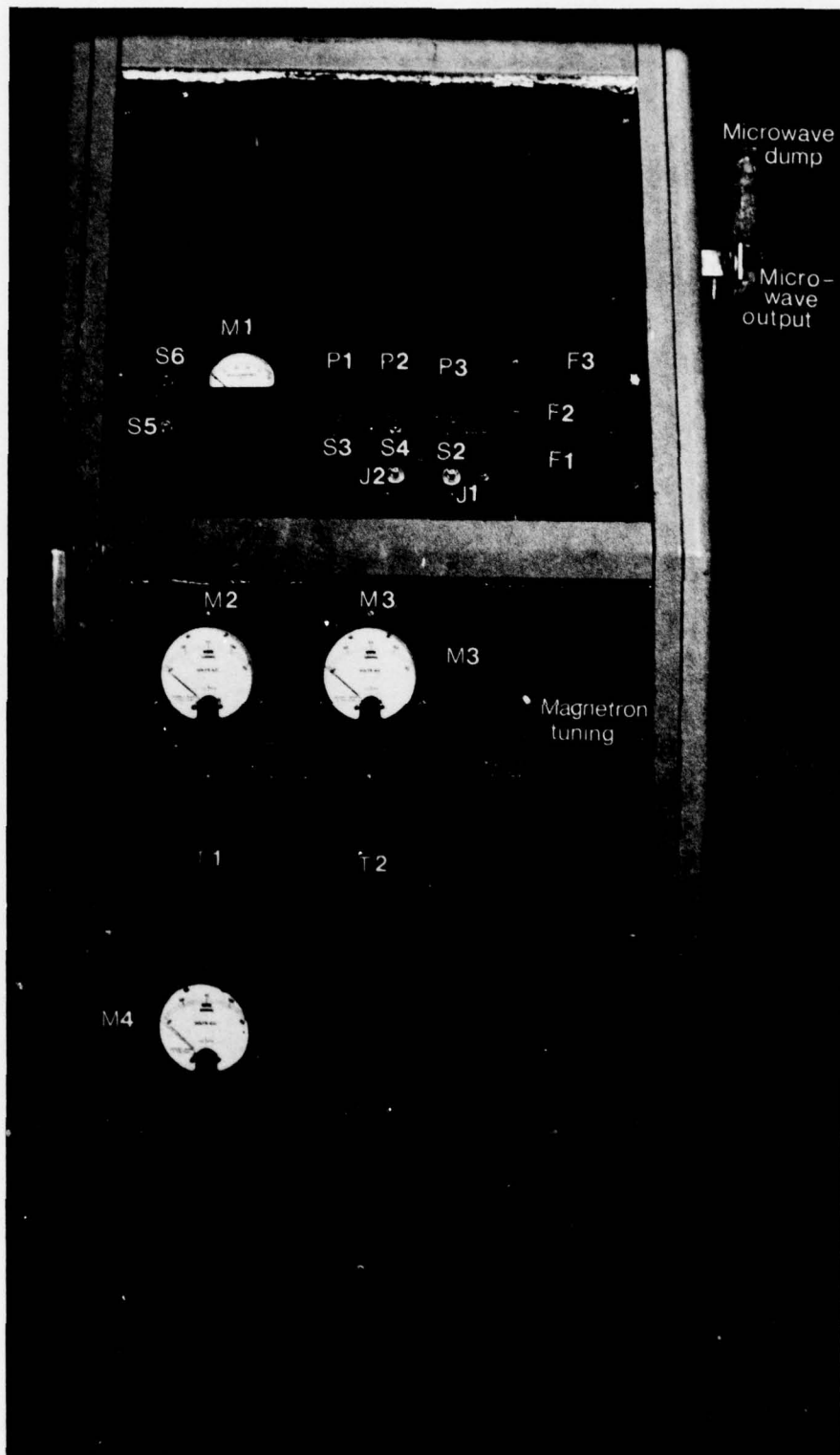
Figure V-5. Photograph of the pulse modulator high power magnetron rack console.
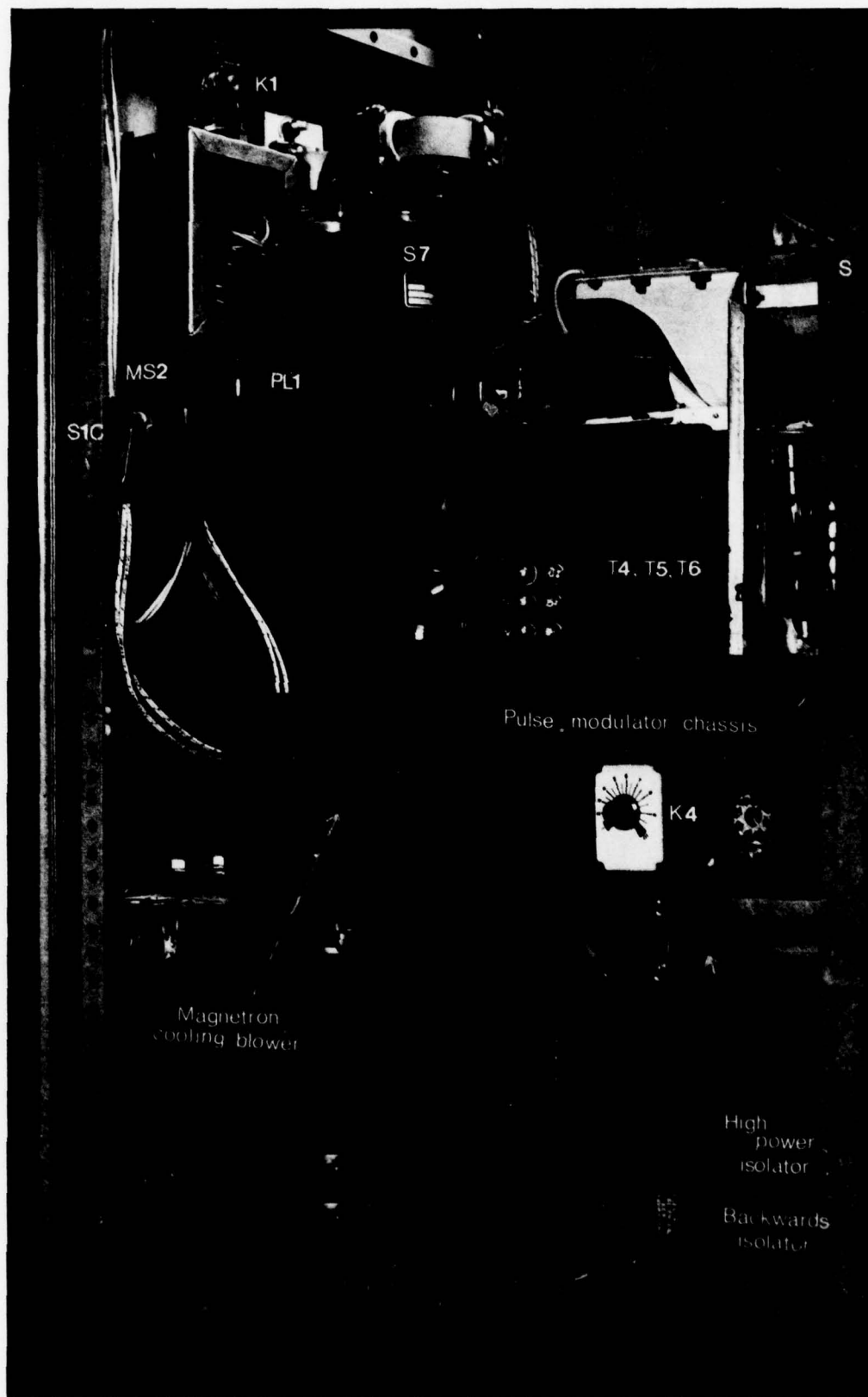
Figure V-6. Photograph of the pulse modulator installation.

68

Upright mounting was found to be necessary because of the oil filled high voltage transformer. The magnetron and isolator are affixed to the pulser as shown in Fig. V-7. The microwave dump switch is bolted to the cabinet, and supports the dummy load and output wave guide. The attenuator is bolted to the waveguide between the isolator and dump switch.

The magnetron is a Raytheon type 2J51. It is tunable over the range 8.5 to 9.6 GHz. This is accomplished by copper shunts which can be moved into or out of the cavities in the anode block (Collins, 1948). The 2J51 has removable magnetic shunts which permit operation at pulse voltages and currents from 10 kV and 10 A to 15 kV and 15 A. It is capable of nearly 65 kW peak output power. As employed here, the output is about 20 kW. The magnetron is driven by a hard tube pulse modulator which is described below.

The attenuator must reduce the peak pulsed power from 20 kW to about 1 kW. Because of the power levels involved, the attenuator consists of a resonance type isolator connected backwards. At 9 GHz this gives about 13 db attenuation.

The microwave dump switch is a Bogart model SA511U SPDT waveguide switch. It is connected so that, in the normally-off state, power is fed to the spectrometer. Application of 24 V dc causes it to switch power to the dummy load.

The hard tube pulse modulator provides high voltage pulses across the magnetron. It does this by charging a capacitor, and then partially discharging it through the magnetron. A greatly simplified but typical schematic of a hard tube modulator, shown in Fig. V-8, serves to illustrate how this is accomplished. A pulse is applied to the input of the driver, D which produces a square pulse of greater amplitude. This pulse turns on the switch tube which allows the storage capacitor C to discharge through the magnetron. When the switch tube returns to the off state, the capacitor is
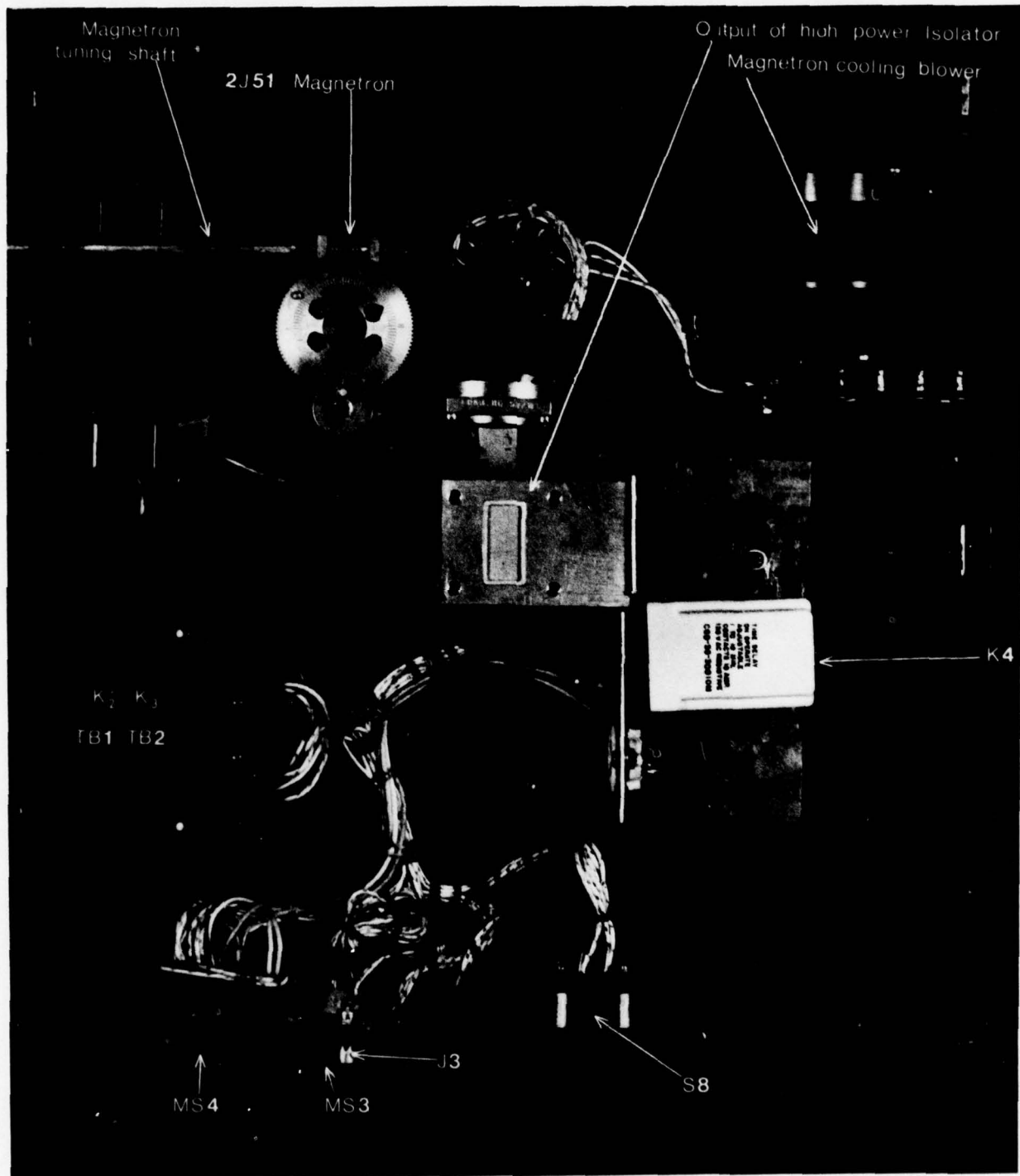
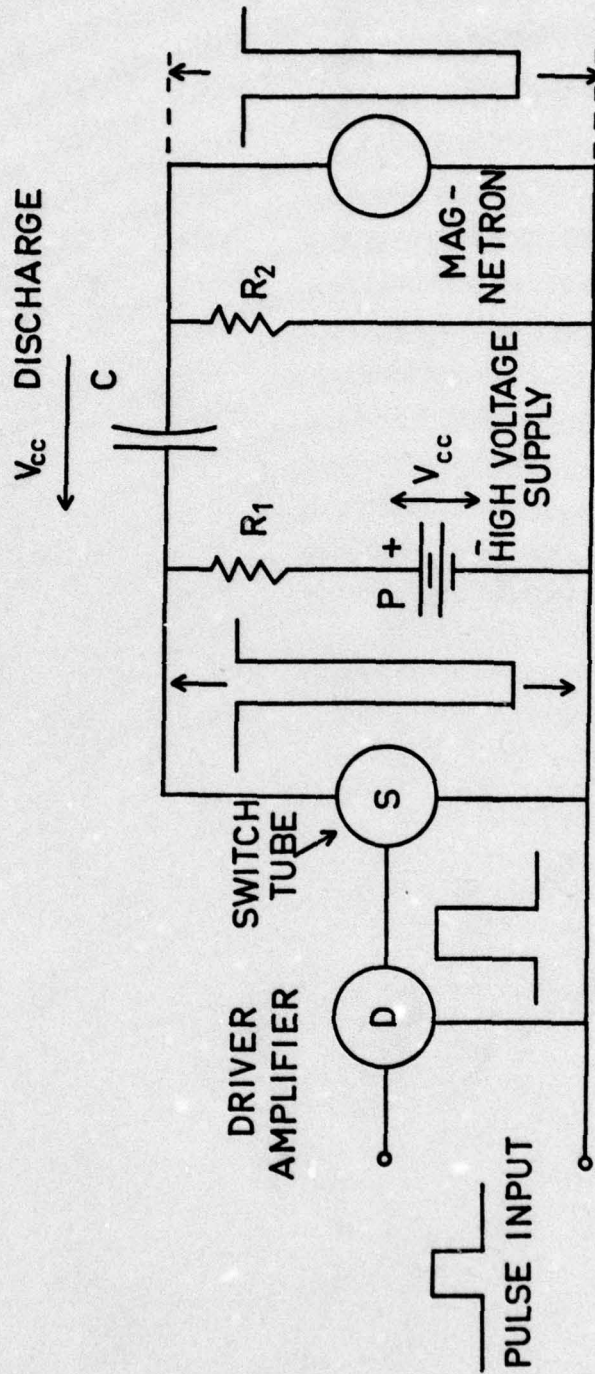Figure V-7. Magnetron and isolator configuration.

Figure V-8. Simplified schematic of the hard tube modulator.

recharged to V_{cc} through R_1 and R_2 by the high voltage power supply P.

The pulse modulator used here is an MIT Model 3, which was designed for airborne radar use in the 1940's. This unit was chosen because (1) it is available very cheaply on the surplus electronics market, and (2) it is described in considerable detail, including oscillographs of typical waveforms, by Glasoe and Lebacqz (1948). The unit was designed to drive a 725A magnetron, which is electrically similar to the 2J51. The 2J51 is mechanically compatible with the modulator requiring only that a hole be drilled in the chassis to admit the magnetron tuning shaft.

The Model 3 was produced and is available in two versions designated Mark I and Mark II. Both were designated to supply 12 kV 12 amp pulses of 0.5, 1 and 2 μsec with a maximum duty cycle of 0.001. Both pulsers require an input pulse of at least 100 V, the shape of which is not critical. The Mark I requires an ac power input of 115 V at 400-2000 hz. The Mark II has a more restricted frequency range of 800-1600 Hz. Both models require 24 V dc to operate the relays and blowers. The storage capacitance of the Mark II is 0.15 μf, three times that of the Mark I. Therefore, the voltage droop of the Mark II pulse is only one third that of the Mark I. This is an important consideration for spin-wave linewidth work, and is especially so where the pulse duration is to be extended. For this reason, the unit used here is a Mark II.

The operation of the Model 3 pulser can be understood in terms of Fig. V-8, and the schematic diagram shown in Fig. V-9. The driver stage in the Model 3 consists of an 829 dual tetrode operated as a blocking oscillator. This produces a square pulse whose shape is independent of that of the trigger pulse. The duration of this pulse is determined by the electrical length of the particular L-C approximate delay line chosen. The output of the blocking oscillator is inverted in the pulse transformer, and
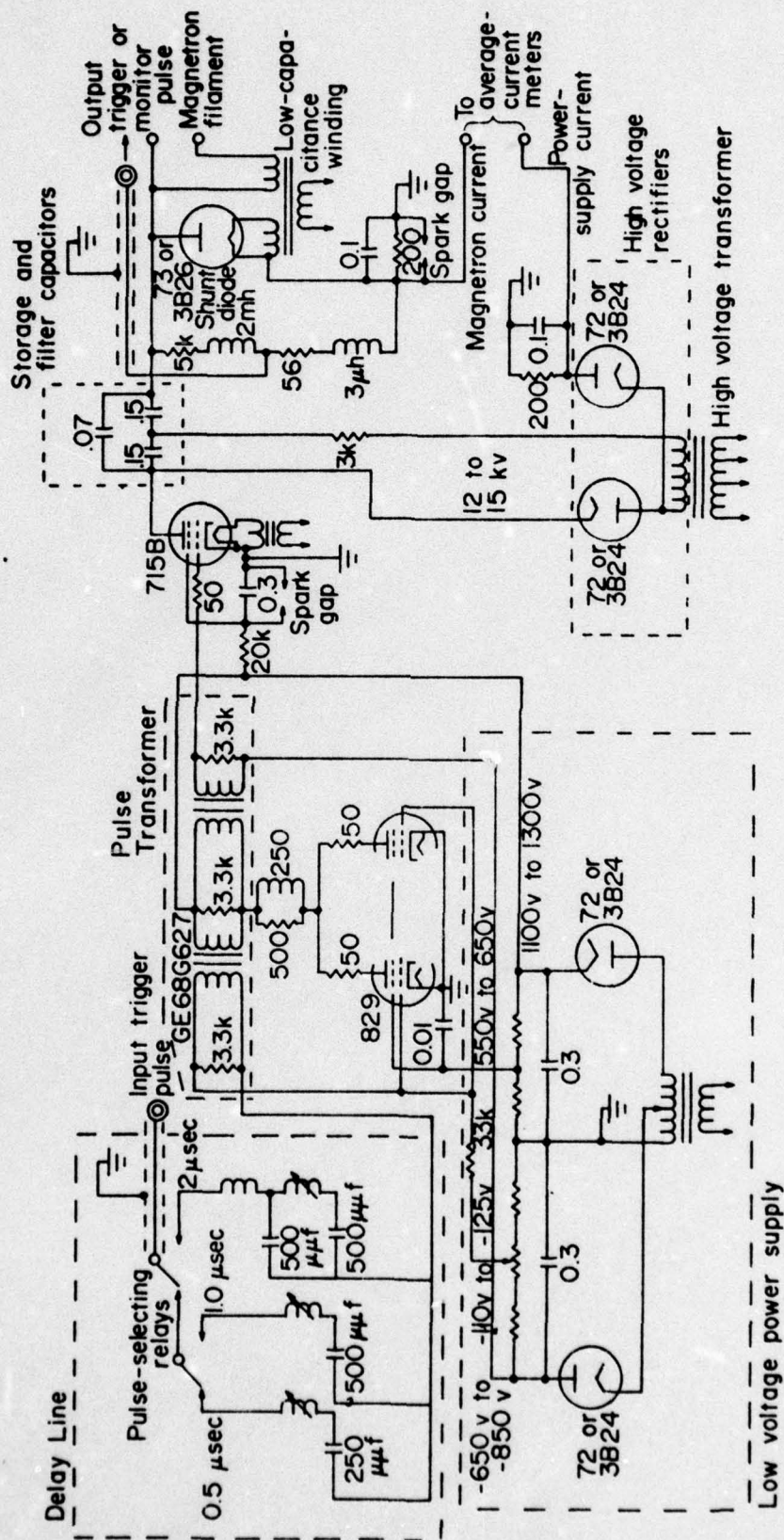
Figure V-9. Schematic diagram of the MIT Model 3 pulse modulator.

is used to turn on the 715B switch tube. The driver is powered by the low voltages for the switch tube.

The high voltage power supply consists of the high voltage transformer, the rectifier tubes, the filter capacitor network, and various resistors and inductors which isolate the power supply during the pulse. The power supply is connected as a voltage doubler in which the filter capacitors also act as the storage capacitor. The shunt diode is provided to dump the inductive overshoot at the end of the pulse due to the 2 mh inductor. Some adjustment of the high voltage is provided by taps on the primary of the high voltage transformer and by an 8 ohm variable resistor (not shown) which is in series with the primary.

The Model 3 pulser can be used without modification for spin-wave line-width measurement. This requires only the fabrication of appropriate control circuitry. However, the unit was not originally designed for such work and therefore has some shortcomings. These have been eliminated by various modifications. The shortcomings and associated modifications are described in the following paragraphs.

Pulses of $\frac{1}{2}$ and 1 µsec duration are of little use for spin-wave line-width measurement. Much more desirable would be pulses of 2 to 4 µsec. Therefore the delay line of the blocking oscillator has been modified to give pulses of 2, 3 and 4 µsec. This was accomplished by replacing the $\frac{1}{2}$ µsec delay line with the 1 µsec line from another Model 3, and reconnecting the pulse selecting relays.

As supplied, the Model 3 has no protection against accidental energizing of the high voltage circuitry before a sufficient warm up has occurred. This was remedied by routing the power to the high voltage circuitry through a time delay relay.

The frequency stability of the magnetron is quite sensitive to the anode voltage. As previously discussed, some anode voltage adjustment was provided in the original design. For spin-wave linewidth measurement however, additional adjustment is desirable. Therefore, the high voltage was rendered continuously adjustable by connecting the high voltage primary to a variac.

The original pulser was wired so that power to the magnetron fillament was cut off during operation. The magnetron cathode was to be heated entirely by back bombardment. However, back bombardment was found to be insufficient to sustain operation of several 2J51's. Therefore, the magnetron filament primary was reconnected to remain on during operation. Furthermore, the filament voltage was made adjustable by powering the filament primary off of a variac.

The ripple from the high voltage power supply produces noticeable jitter on the microwave pulse amplitude. Therefore, it would be desirable to synchronize the pulses with the ripple. Synchronization will be accomplished with a system which is presently under construction. This system will be triggered at the power supply frequency, off of the switch tube filament winding. The resulting pulse train will be divided by n, where n can be chosen between one and 1000, to give trigger pulses at a submultiple of the power supply frequency. These pulses will then be amplified and applied to the driver stage.

The following discussion provides a detailed description of the pulser as modified, and of the associated control circuitry. Figures V-10 to V-13 comprise a complete schematic diagram. Various components shown in these figures are identified in Table V-1.

Figure V-10 covers the external control circuitry which is located in the cabinet, and on the front panels. Wiring between the cabinet, front

panels, and the pulser is routed through plugs to facilitate access. Power
is brought into the cabinet through a nine pin MS connector labeled MS1.
It is then routed through the safety interlock system to octal plug PL1,
which supplies power to the upper front panel. The safety interlock system
consists of relay K1, which is controlled by microswitches S1A, S1B, and
S1C. The microswitches are mounted so that they open whenever a panel or
cabinet door is opened, and thereby cut off all power to the front panels
and the pulser. Also mounted to the cabinet is the microwave dump waveguide
switch S7.

Power is supplied to the pulser by the upper front panel, on which are
mounted the standby and operate switches S3 and S4, and the pulse input
jack J1. Also mounted on the upper front panel are: the pulse duration
selector switch S5, the average current meter M1 and meter switch S6,
d-c fuse F1, standby fuse F2, operate fuse F3, standby and operate indicator
lights P1 and P2, pulse monitor jack J2, the high voltage primary resistor,
and microwave dump actuator switch S2 and pilot lite P3. When completed,
the synchronous trigger chassis will be mounted in the front panel. It will
be powered and will receive its trigger signal through MS8, and will drive
the pulser through J4.

The lower front panel contains variacs T1 and T2. The output voltages
of the variacs are displayed on meters M2 and M3. Meter M4 indicates the
a-c line voltage. The magnetron tuning shaft emerges through the lower
panel.

The pulser is diagrammed as three subsystems: the control system, the
high voltage system, and the driver system.

The control system is shown in Fig. V-11. It is located on the under-
side of the pulser chassis. The layout of components is shown in Fig. V-7.
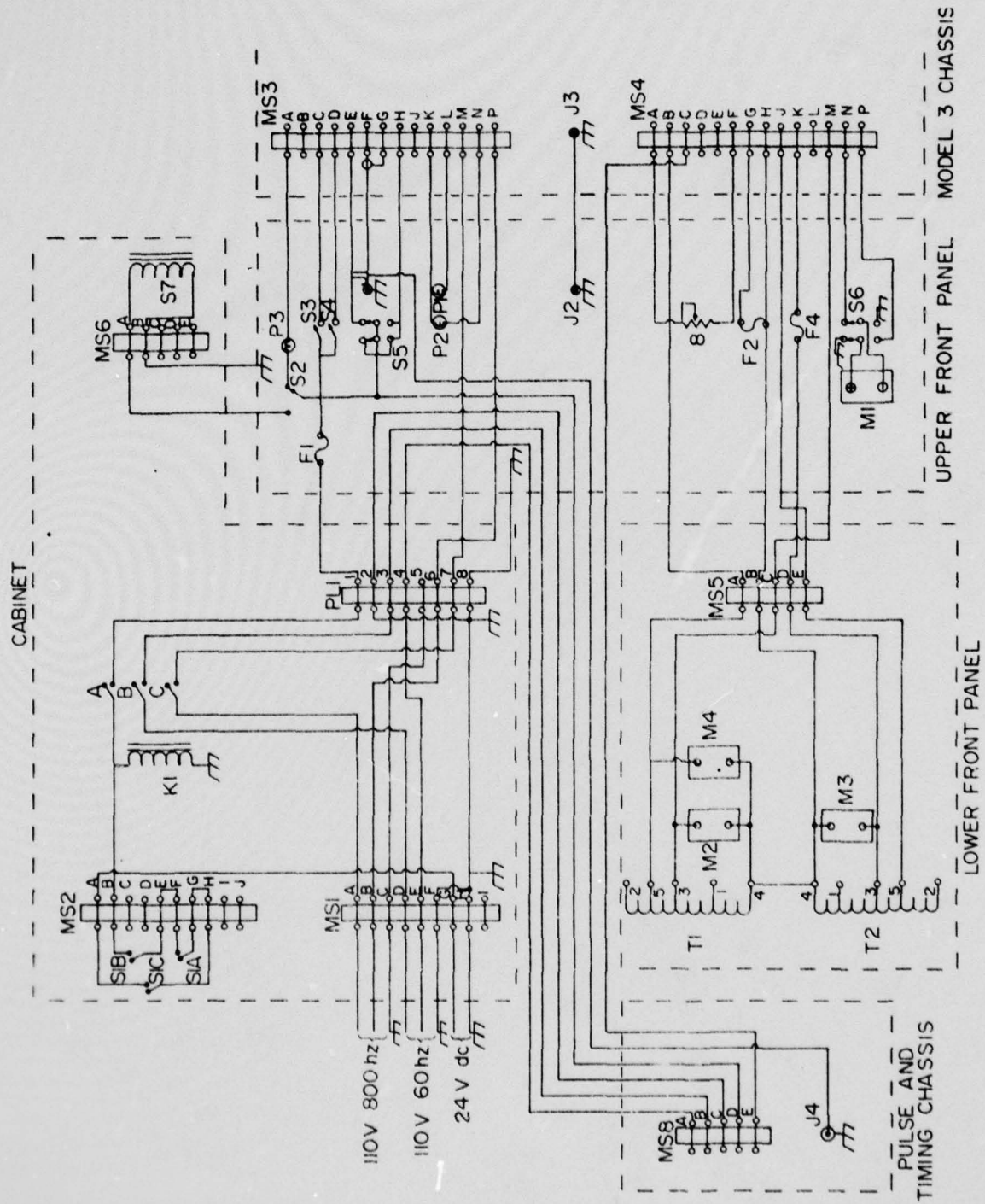
76

Figure V-10. External control circuitry for the modified pulse modulator.
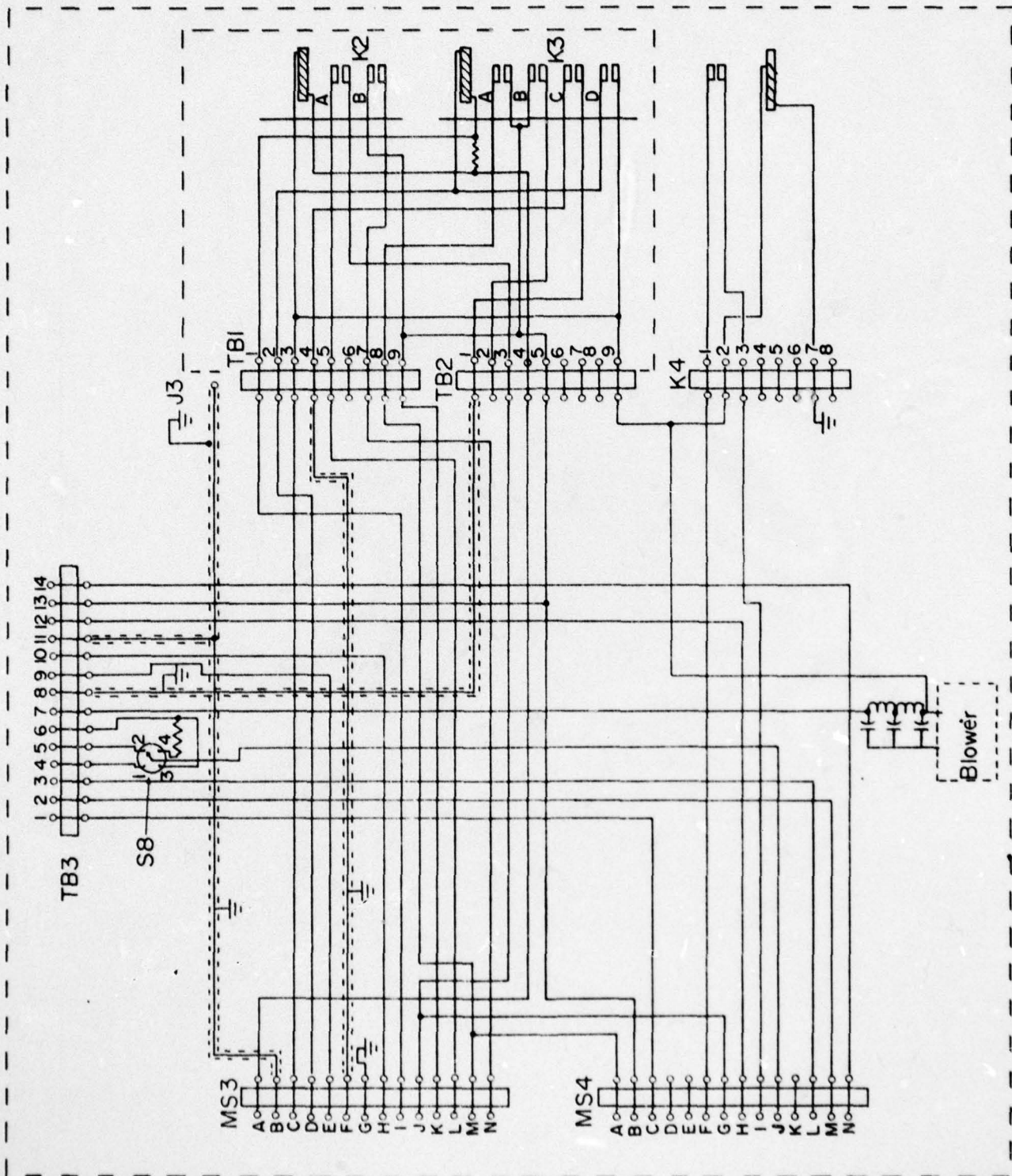
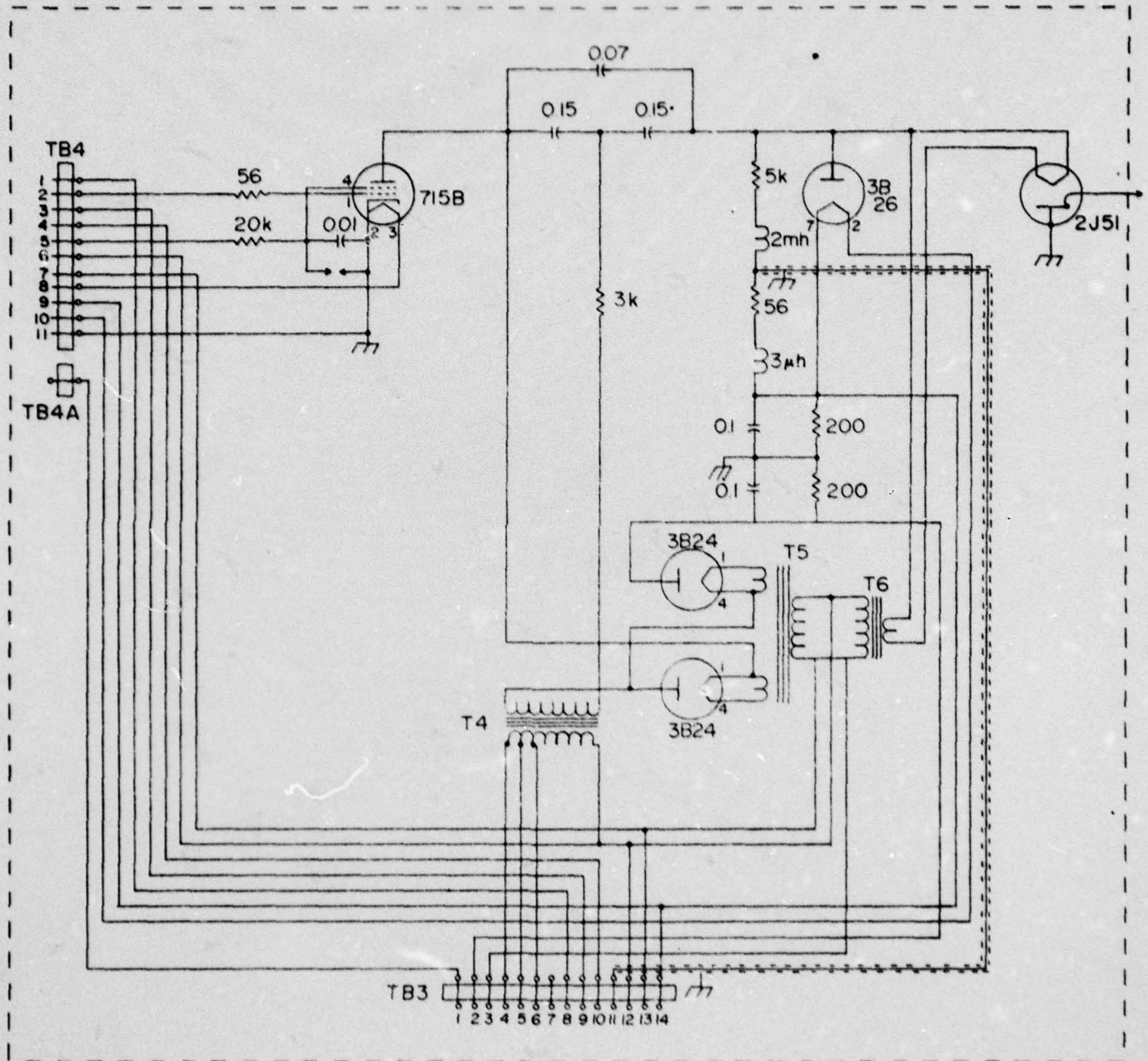Figure V-11. Control subsystem for the modified pulse modulator.

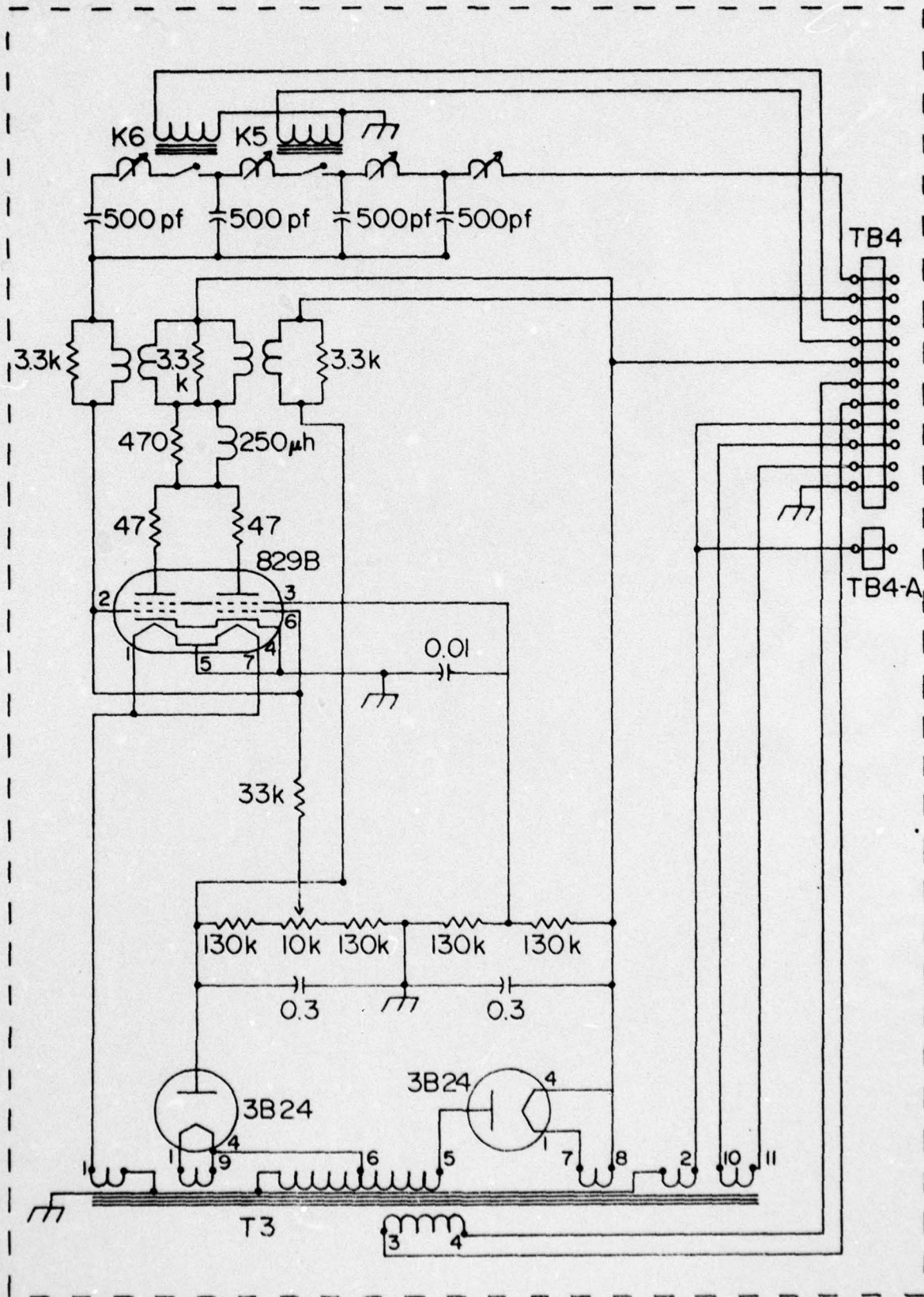Figure V-12. High voltage system for the modified pulse modulator.

Figure V-13. Driver and low voltage power supply for the modified pulse modulator.

Table V-1. Functions of Components Shown in Figs. V-10 to V-13.

Switch	Figure	Function
S1A,B,C	V-10	Safety Interlock Switches
S2	V-10	Microwave Diverter Actuator
S3	V-10	Standby Switch
S4	V-10	Operate Switch
S5	V-10	Pulse Duration Selector Switch
S6	V-10	Average Current Monitor Switch
S7	V-10	Microwave Diverter Waveguide Switch
S8	V-10	High Voltage Primary Tap Selector

Fuse	Figure	Function
F1	V-10	DC Control Fuse
F2	V-10	Standby Fuse
F3	V-10	High Voltage Fuse

Pilot Light	Figure	Function
P1	V-10	Standby Pilot Light
P2	V-10	Operate Pilot Light
P3	V-10	Microwave Status Pilot Light

Relay	Figure	Function
K1	V-10	Safety Interlock Relay
K2	V-11	Standby Control Relay
K3	V-11	Operate Control Relay
K4	V-11	High Voltage Time Delay Relay
K5	V-13	Pulse Selecting Relay
K6	V-13	Pulse Selecting Relay

Meter	Figure	Function
M1	V-10	Average Current Meter
M2	V-10	Magnetron Filament Primary Voltmeter
M3	V-10	High Voltage Primary Voltmeter
M4	V-10	Line Voltmeter

Jack	Figure	Function
J1	V-10	Pulse Input Jack
J2	V-10	Front Panel Pulse Monitor Jack
J3	V-10	Pulser Pulse Monitor Jack
J4	V-10	Trigger Pulse Output Jack

The control system consists primarily of relays K2 and K3 which control the distribution of power through TB3 to the driver and high voltage circuits. It also contains time delay relay K4. This is connected in series with the high voltage primary to prevent activation of the high voltage prior to a sufficient warmup. The control system is connected to the upper and lower front panels through MS3 and MS4. MS3 is the original 14 pin MS connector. MS4 is also a 14 pin MS connector which was added to give additional front panel access to pulser circuitry.

The driver and high voltage systems are located on the top side of the pulser chassis. They are connected to the control circuitry through TB3. The high voltage system is shown in Fig. V-12. It consists of the switch tube and high voltage power supply. The driver is mounted in a separate subchassis which also contains the low voltage power supplies. The driver and low voltage power supply are diagramed in Fig. V-13, and are connected to the high voltage system and to TB3 through TB4.

The magnetron is shown in Fig. V-12 with the high voltage system. It is screwed to the chassis so that the body lies beneath the chassis as shown in Fig. V-7, and the filament connections lie above it. The magnetron tuning shaft passes through the chassis and exits the cabinet through the upper right hand corner of the lower front panel.

Power is supplied to the pulser by external ac and dc power supplies. The characteristics of the 24 V dc supply are not critical. The 115 V ac is supplied at 800 - 1000 Hz by a Sorenson model FCR 250 frequency changer.

Until the synchronous triggering circuitry is completed, trigger pulses will continue to be generated externally. As previously noted, the shape of the trigger pulses is not critical. A military type TS-592A/UPM-15 pulse generator is currently used to provide 120 V 1 μsec pulses at a typical repetition rate of 200 Hz.

Actual operation of the high power pulses is as follows. The pulser is put into the standby condition by closing standby switch S3. This energizes standby relay K2, which turns on the low voltage power supply, all filaments, and the magnetron cooling blower. Closing S3 also initiates the timing cycle of the time delay relay K4. The grid bias of driver tube is adjusted to cut the tube off in the standby mode.

After a three minute time delay, the pulser can be put into the operate mode by closing operate switch S4. This energizes relay K3, which supplies power to the primary of the high voltage transformer, and connects the input pulses at J1 to the driver.

The desired pulse duration is selected with S5. In the center off position, both relays K5 and K6 are open, giving a 2 µsec pulse. Switching to the 3 µsec position closes K5. In the 4 µsec position both K5 and K6 are closed.

The average magnetron and power supply currents can be monitored at meter M1. In the power supply current mode, switch S6 connects M1 in series with the high voltage power supply. In the magnetron current mode, M1 is connected in series with the capacitor charging circuit. It is assumed that the average capacitor charging current is equal to the average magnetron current. The average magnetron current is typically 6 ma.

The magnetron filament voltage and the high voltage are adjusted with variacs T1 and T2, which control the voltages at primary windings of the magnetron filament and high voltage transformers. These primary voltages are indicated on meters M2 and M3. The line voltage into the pulser is adjustable at the ac power supply and is indicated by M4. These voltages are adjusted to minimize the variation in magnetron frequency across the pulse.

The magnetron is tuned by rotating the mechanical tuning shaft clockwise for increasing frequency.

The microwave dump waveguide switch is operated from switch S2 on the front panel. Closing S2 diverts the microwave power into the dummy load, and extinguishes the microwave status light P3.

D.   CAVITY AND TEMPERATURE CONTROL SYSTEM

The cavity and temperature control system is shown schematically in Fig. V-14. The cavity is held in contact with a liquid nitrogen bath, and is evacuated through the pumping manifold. The vacuum space extends from the pumping manifold to the bottom of the sample stand tube. The sample is positioned on the sample stand assembly, approximately one sample diameter from the cavity bottom. The sample stand assembly is thermally isolated from the cavity, and is mechanically and thermally isolated from the liquid nitrogen bath. It contains a thermocouple to measure the sample temperature and a heater to control sample temperature.

The thermocouple controls the heater through the temperature control system. A voltage which corresponds to the sample temperature is generated by the thermocouple and reference junction. This voltage is compared in the potentiometer with a voltage which corresponds to the desired sample temperature. The difference between the desired and actual voltages is indicated and amplified by the microvoltmeter. If the sample temperature is less than that which is desired, the heater power is increased by an amount which is proportional to the temperature difference.

The design of the cavity and temperature control systems affords the following desirable features.

(1) The cavity temperature remains constant at 77 K, independent of sample temperature. This means that the cavity calibration is the same at all temperatures.

(2) The sample stand can be removed without warming up the cavity. This facilitates rapid change of samples.

(3) The sample temperature can be maintained for long periods of time within 0.05 C of any temperature between 77 and 377 K.
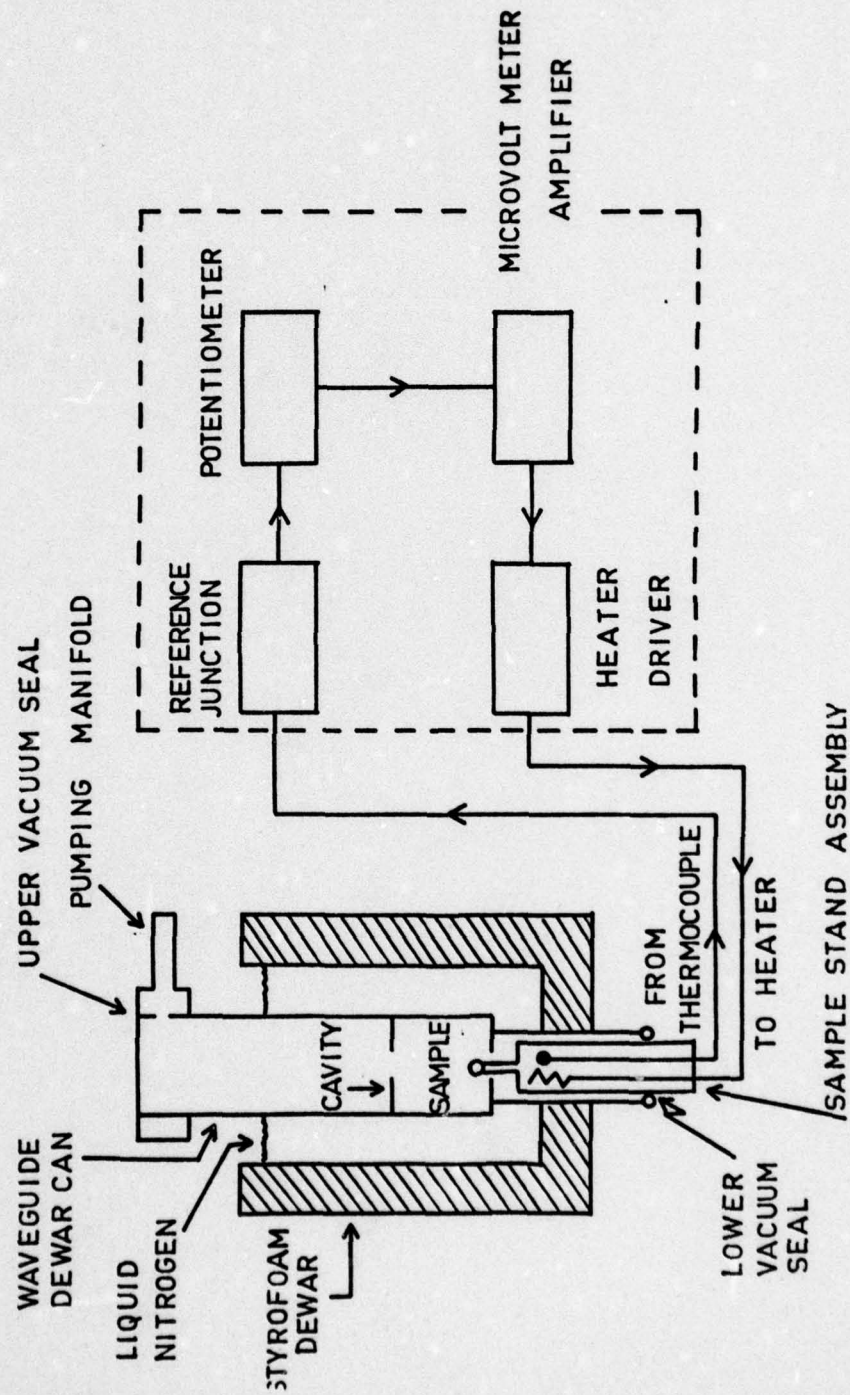
Figure V-14. Cavity and temperature control system for the high power spectrometer.

The desired sample temperature is obtained as follows:

(1) The cavity is pumped out and is brought into equilibrium with the liquid nitrogen bath.

(2) The potentiometer is standardized.

(3) The potentiometer source voltage is set to that which corresponds to the desired temperature.

(4) The heater-driver ambient and gain controls are adjusted such that the thermocouple voltage fluctuations lie within 1 μv of the programmed voltage.

E.   CAVITY AND TEMPERATURE CONTROL

The details of the cavity, dewar, and sample stand assemblies are shown
in Figs. V-15 to V-17. The cavity and dewar are soldered together to form
a single unit. The sample stand assembly is a separate unit which can be
removed from the cavity-dewar assembly. Figure V-15 depicts the top of the
overall assembly including the waveguide top and pumping namifold, and the
top of the dewar. The center of assembly including the cavity, the dewar
bottom, and the top of the sample stand assembly appear in Fig. V-16.
Figure V-17 shows the details of the lower vacuum seal and the lower portion
of the sample stand. The various components shown in these three figures
are identified in Table V-2. A description of these components follows.

The TE_{101} cavity consists of the cavity body (part A), the bottom plate (part
B), and iris plate (part C). The cavity body is a 24.5 mm piece of 25.4 mm
x 12.7 mm bronze waveguide. The iris plate and cavity bottom are brass.
The bottom plate is 1.25 mm thick, with a 3 mm sample insertion hole. The
iris plate is 0.635 mm thick, and has a 6 mm coupling hole. These dimensions
result in a cavity which, at 77 K, resonates at 8.882 GHz, has a Q of
approximately 2500, and is overcoupled with a reflection coefficient of
20 db.

Both the iris plate and bottom plate are silver soldered to the cavity
body. This is necessary because the A-B joint must carry the entire dewar
and sample holder assemblies. It is also desirable because it allows the
cavity to be soft soldered as a unit into a standard UG39/U waveguide flange
for iris calibration, and then to be removed intact and soft soldered into
the system without effect on the calibration. Early attempts at silver
soldering the cavity were unsuccessful due to the formation of voids in the
solder which drastically lowered the Q of the cavity. The problem was
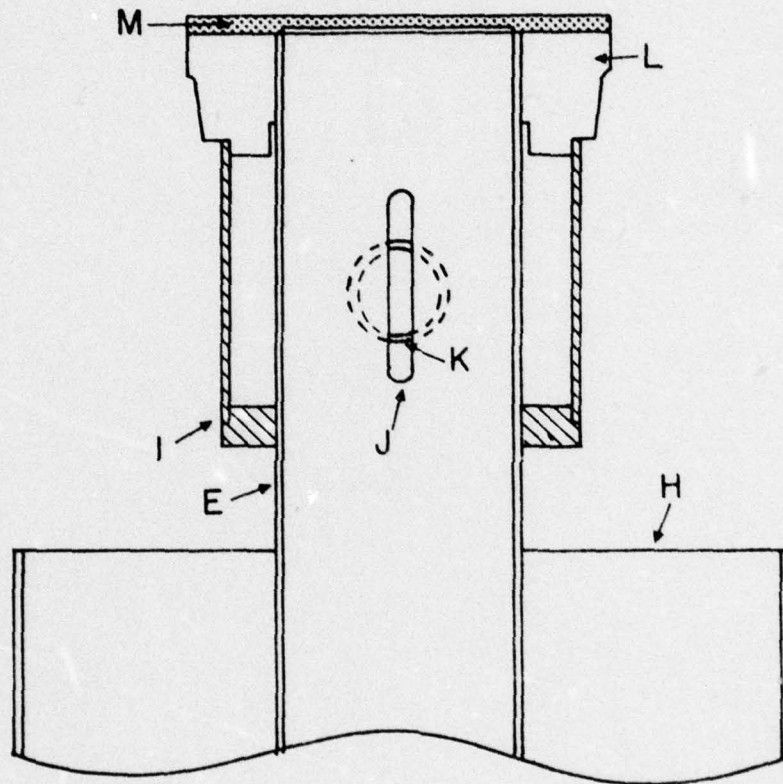solved by maintaining the entire cavity assembly at near the solder melting

Figure V-15. Top portion of the cavity assembly showing the top of the dewar, the upper vacuum seal, and the pumping manifold.
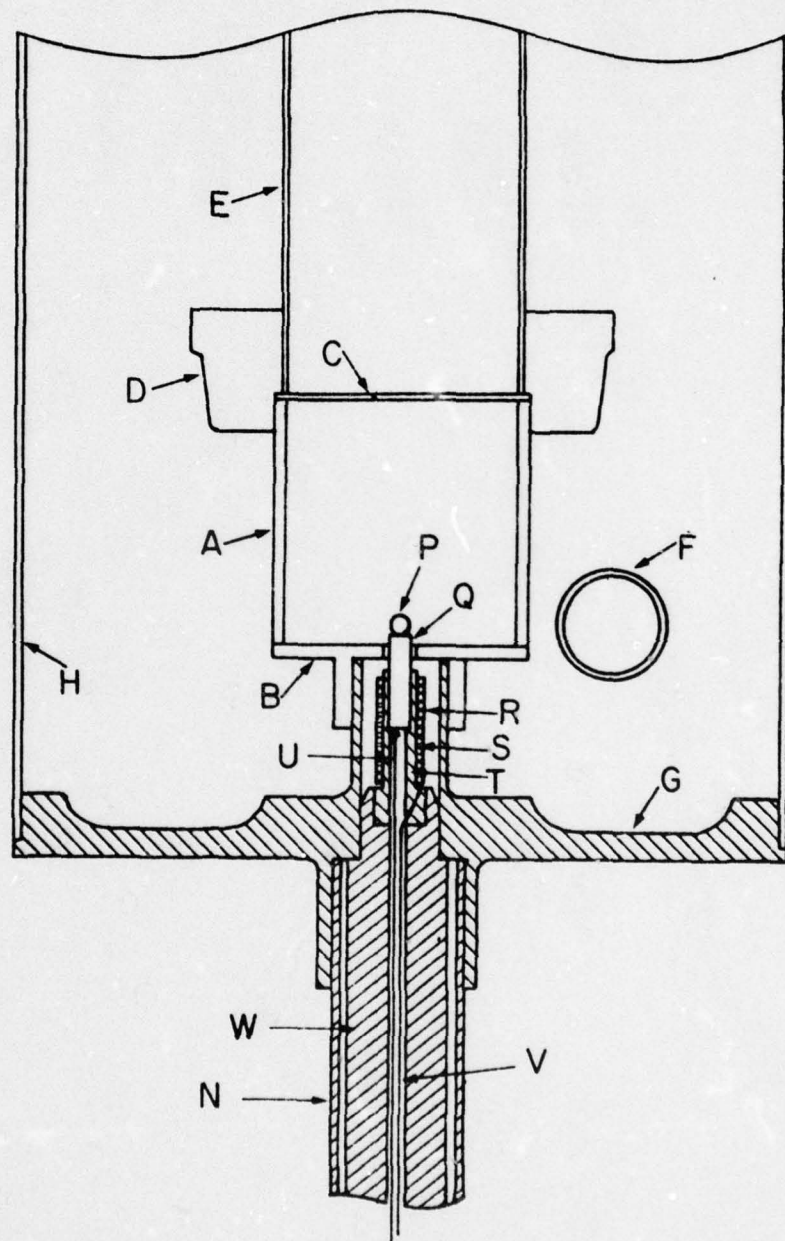
Figure V-16. Middle portion of the cavity assembly showing the cavity, the bottom of the dewar, and the upper portion of the sample.
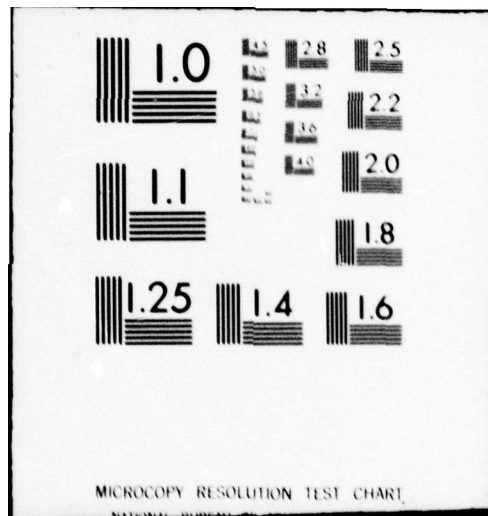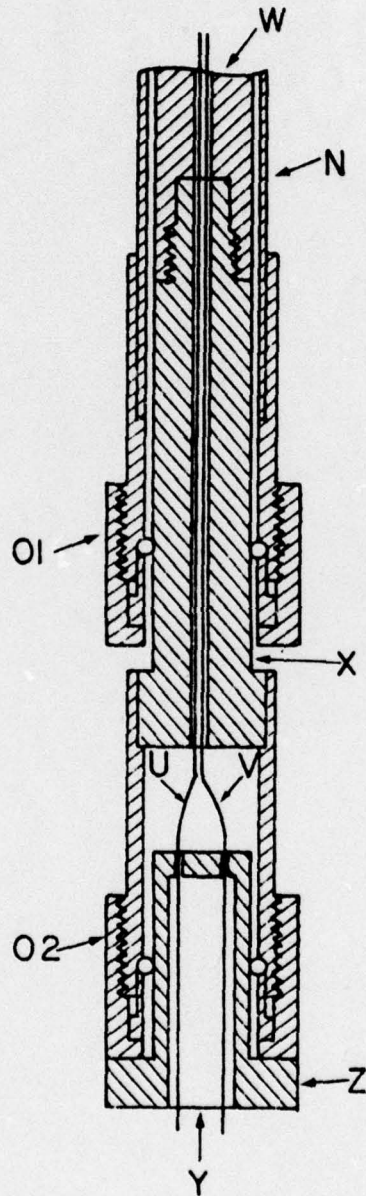
MICROCOPY RESOLUTION TEST CHART

Figure V-17. Bottom portion of the cavity assembly showing the lower sample stand and the lower vacuum seal.

Table V-2. Spin-wave Linewidth Cavity Components and Materials.

Label in Figs. V-15 to V-17	Description	Material
A	Cavity Sides	Bronze
B	Cavity Bottom Plate	Brass
C	Cavity Iris Plate	Brass
D	Lower Waveguide Flange	Brass
E	Thin-wall Waveguide	Stainless Steel
F	Hall Probe Shield Tube	Stainless Steel
G	Dewar Bottom	Stainless Steel
H	Dewar Can	Stainless Steel
I	Pumping Manifold	Brass
J	Waveguide Pump-Out Slot	
K	Manifold Outlet Pipe	Copper
L	Upper Waveguide Flange	Brass
M	Waveguide Pressure Window	Mica
N	Thermal Isolation Tube	Stainless Steel
$\emptyset 1, 2$	Quick Connect	Brass
P	Sample	
Q	Sample Mount Rod	Type I Diamond
R	Heater Insulator	Heat Shrink Tubing
S	Heater Winding	Manganin Wire
T	Heater Barrel	Copper
U	Thermocouple	Copper-Constantan
V	Heater Leads	Copper
W	Upper Base	Nylon
X	Lower Base	Brass
Y	Feed-Through Potting	Epoxy
Z	Feed-Through Body	Lucite

point, with a propane torch, while running the solder with an acetylene flame.

The waveguide (Part E) is 0.38 mm wall stainless steel. It is silver soldered at the top and bottom into UG39/U brass waveguide flanges which have been milled out to the outside waveguide dimensions. The top flange has also been turned on the back side to form the top of the copper pumping manifold, which is soft soldered together. The waveguide is coupled to the pumping manifold through a 1.5 mm slot (Part J) milled in the guide. The upper vacuum seal is made with a mica window (Part M) which is sandwiched between the top flange, and the flange of a short piece of waveguide (not shown). This upper piece of waveguide has a waveguide quick-connect on its top flange. This arrangement allows the entire assembly to be disconnected from the spectrometer without disrupting the cavity vacuum.

The dewar assembly consists of the dewar can (Part H), the dewar bottom (Part G), the thermal isolation tube (Part N), the Hall probe shield tube (Part F) and the quick-connect $\emptyset 1$. All joints have been soft soldered. The dewar assembly, from the top of the can to near the quick connect, is encased in styrofoam for thermal insulation. The Hall probe shield tube allows the Hall probe to be placed near the sample. The low temperature inside this tube requires that the probe be encased in Lucite, and that measurements be of short duration. Quick-connect $\emptyset 1$ forms the lower vacuum seal about the sample holder assembly.

The sample sits on a diamond finger (Part Q). The diamond is a natural type I stone, which has been ground to an average cross-sectional dimension of 1.65 mm. The diamond was obtained from Diamond Abrasive Corp., 2 West 48th St., New York, NY 10036. Diamond was chosen for this application because it produces minimal dielectric loading of the cavity with maximal thermal conductivity.

The thermal conductivity of type I diamond is at least twice that of copper (Burgemeister, 1975) over the entire temperature range of the apparatus. The dielectric loading due to the diamond lowered the Q of the cavity by about 100.

The diamond is soldered with indium to the copper heated barrel, which is noninductively would with 0.15 mm manganin wire. The heater winding (Part S) is encased in heat shrink tubing (Part R). The copper constant on thermocouple junction (Part U) is embedded in wakefield grease at the base of the diamond.

The heater assembly is pressed into the nylon upper base (Part W) which in turn is threaded onto the brass lower base (Part X). Quick-connect $\emptyset 2$ is soldered to the lower base. The thermocouple and heater leads are routed through the centers of the upper and lower base, and through the potting (Part Y) of the lucite plug (Part Z). Quick-connect $\emptyset 2$ and plug Z comprise the sample stand vacuum seal, and facilitate alterations to, or repair of the wiring.

The temperature control system consists of a thermocouple electronic reference junction, a potentiometer, a microvoltmeter, and a heater driver. The electronic reference junction is an Omega model CJ. The potentiometer is a Leeds and Northrup model K3. The microvolt meter is a John Fluke model 845AB. It provides an adjustable recorder output of up to one volt at full scale meter deflection. Thus, in addition to continuously indicating the thermocouple-potentiometer difference voltage, V_d, the microvolt meter also acts as an amplifier with a gain of

$$G_m = \frac{1V}{V_{full\ scale}} \tag{V-4}$$

The heater driver schematic diagram appears in Fig. V-18. Voltage follower stage A_1 acts as a buffer to prevent loading of the microvoltmeter.
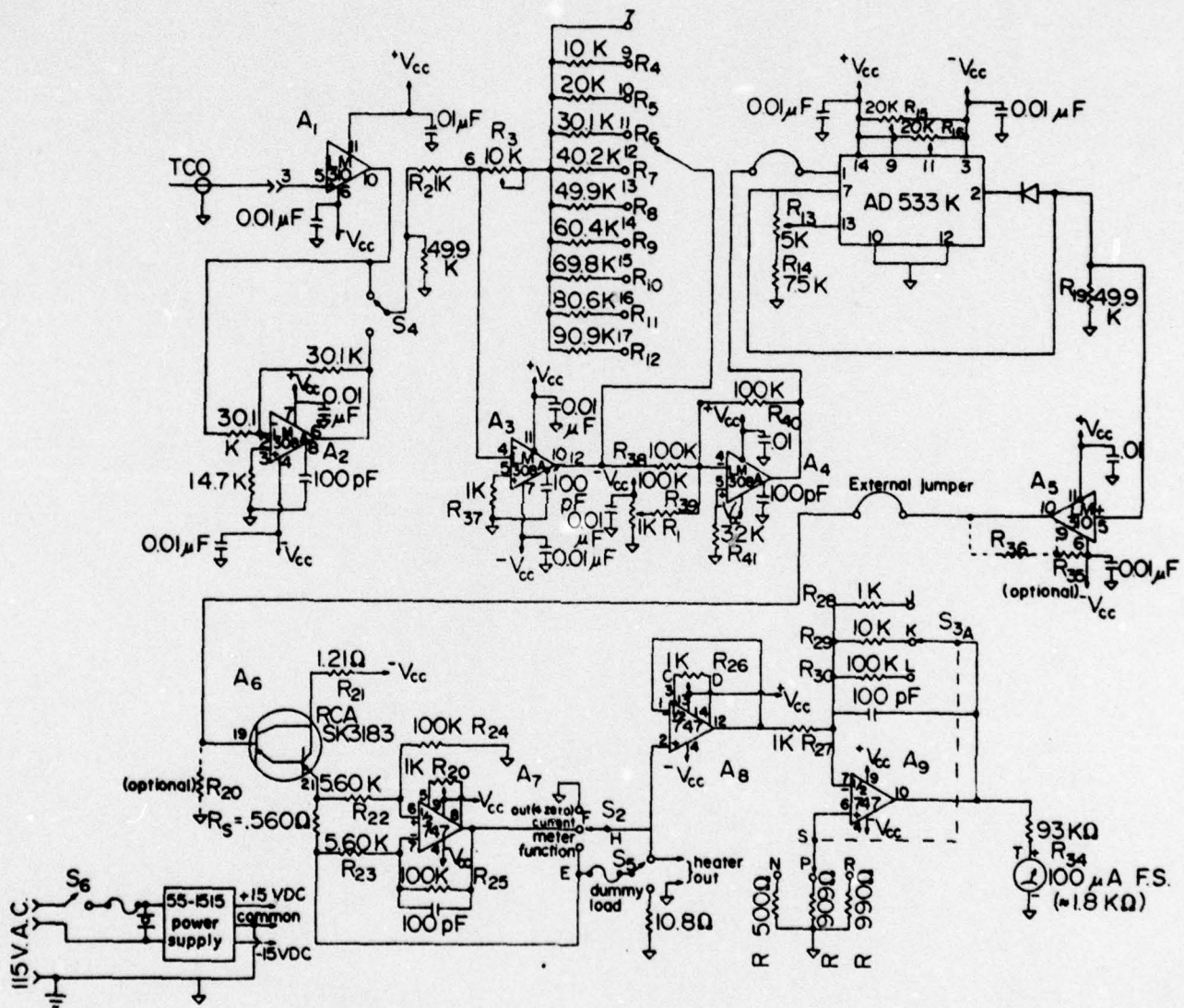
94

Figure V-18. Schematic diagram of the heater driver unit for the temperature control system.

Stage A_2 acts as a unity gain inverter which allows reversal of the input
polarity. Stage A_3 yields a voltage gain, G_2, which is continuously variable
from one to one hundred. Stage A_4 has a gain of unity, and is used to supply
an offset voltage, V_{os}, to the input of the Analog Devices AD533K multiplier
chip. The AD533K is connected to give the transfer function

$$V_{out} = -[10V_{in}]^{\frac{1}{2}} . \tag{V-5}$$

Voltage follower A_5 acts as a buffer between the AD533K and the output
stage A_6. The output stage consists of a monolithic Darlington pair con-
nected as an emitter follower, which serves as a current amplifier. Stages
A_7 through A_9 provide amplification for the panel meter.

The combined voltage gain due to stages A_1, A_2, A_4, A_5 and A_6 is
approximately unity. Thus, the power to that heater is realted to the
thermocouple-potentiometer difference voltage by

$$P_{out} = \frac{10}{R_H} [G_m G_3 V_d + V_{os}] . \tag{V-6}$$

The offset voltage, V_{os}, results in a continuous heater output. This is
necessary if stabilization at the programmed temperature is to be achieved
with a finite loop gain $G_m G_2$. In fact, it is desirable to adjust $(10/R_H)V_{os}$
as nearly as possible to (but less than) the power required to maintain the
desired temperature. This minimizes the loop gain requirement and thereby
minimizes the fluctuation about the programmed temperature. With the system
described here, fluctuations in V_d can easily be held to less than one
microvolt. This corresponds to a temperature fluctuation of less than 0.05 C.

CHAPTER VI

RELATION BETWEEN MICROSTRUCTURE AND EFFECTIVE LINEWIDTH IN

POLYCRYSTALLINE YTTRIUM IRON GARNET

A.   POROSITY DEPENDENCE

Polycrystalline YIG materials prepared with a systematic variation in porosity were used. They were supplied to the principal investigator by Dr. J. J. Green, Raytheon Research Division, Waltham, Mass. They were prepared from yttrium oxide with rare-earth impurity content below 0.1 ppm. Samples of different porosity were obtained by a variation in sintering time and/or temperature. Porosity determinations were made from weight and diameter measurements on individual spheres. The error bars for these determinations are on the order of a few percent. The porous samples are tabulated in Table VI-1. It is to be noted that there is a qualitative but not a quantitative correlation between these measured pore/void porosities and those inferred from the measured magnetization values. The differences could be due to several factors, including the relatively large errors in the weight-volume porosity values and the fact that second phase content would show up differently in the two measurements, depending on the magnetic properties of the second phase. Nonmagnetic second phases would contribute to the density but not to the magnetization. Magnetic second phases would also increase the magnetization. At any rate, the porosities in Table VI-1 should be taken as qualitative, relative parameters only.

The calibration procedure requires an accurate determination of the saturation induction for a given sample at a given temperature. Representative data are presented in Fig. VI-1. The magnetization data were obtained with a conventional vibrating sample magnetometer. In the effective linewidth evaluations to follow, these empirical values will be used in the calibration procedure as discussed in Chapter III.

Table VI-1. Porous YIG Samples.

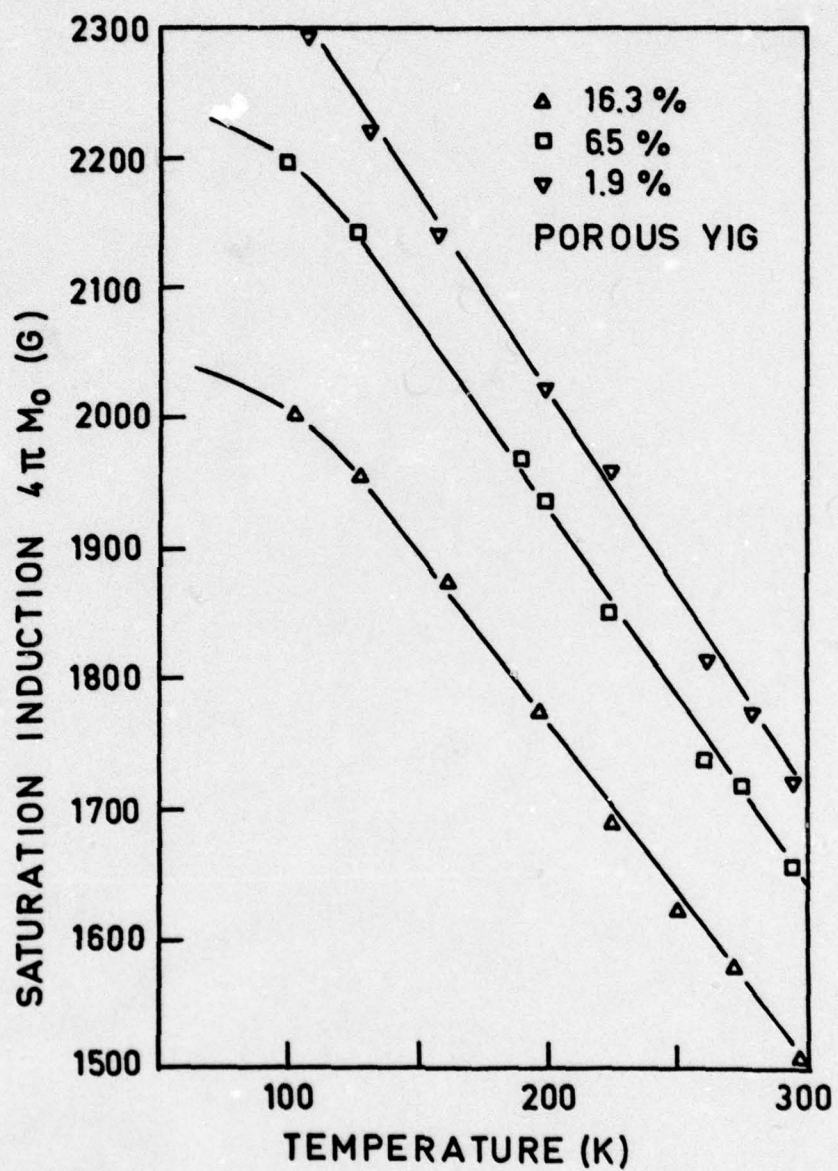| Diameter (mm)	Weight-Volume Porosity (%)	Saturation Magnetization $4\pi M_o$ at 300 K (G)
2.310	<0.5	1750
2.007	1.9	1710
1.800	5.5	1640
1.882	6.5	1640
1.736	9.7	1610
1.959	12.4	1590
1.996	16.3	1500

Figure VI-1.   Saturation induction versus temperature for representative porous YIG samples.

Figure VI-2 presents data on the average high field effective linewidth in the range from 6 to 9 kOe as a function of temperature, for four samples. The dense YIG has the lowest high field ΔH_{eff}, on the order of 0.5 Oe, which is essentially independent of temperature. It is to be emphasized that such ΔH_{eff} values correspond to extremely small susceptibilities on the order of 10^{-5}, at the very limit of resolution for our ultrasensitive system. These ΔH_{eff} values are comparable with those obtained with single crystals. Thus in the dense, large grain limit (>30μ), polycrystals do indeed exhibit off-resonance losses comparable with those found in single crystals.

The data show, however, that the effective linewidth exhibits a large increase with porosity. The magnitude of the increase scales with porosity, but the temperature dependence is qualitatively the same for all the porous samples. Data were not obtained at temperatures above room temperature, but the results for the three porous samples in Fig. VI-2 appear to extrapolate down to the ΔH_{eff} of the dense YIG at about 330 K. It is also noteworthy that the shape of ΔH_{eff} vs. temperature in each case is quite similar to that for magnetization versus temperature for a magnetic phase with a Curie temperature on the order of 330 K. It is tempting, therefore, to associate the additional loss with some as-yet undetermined magnetic second phase content that increases with porosity. These considerations will be explored in more detail in Section C of this chapter.
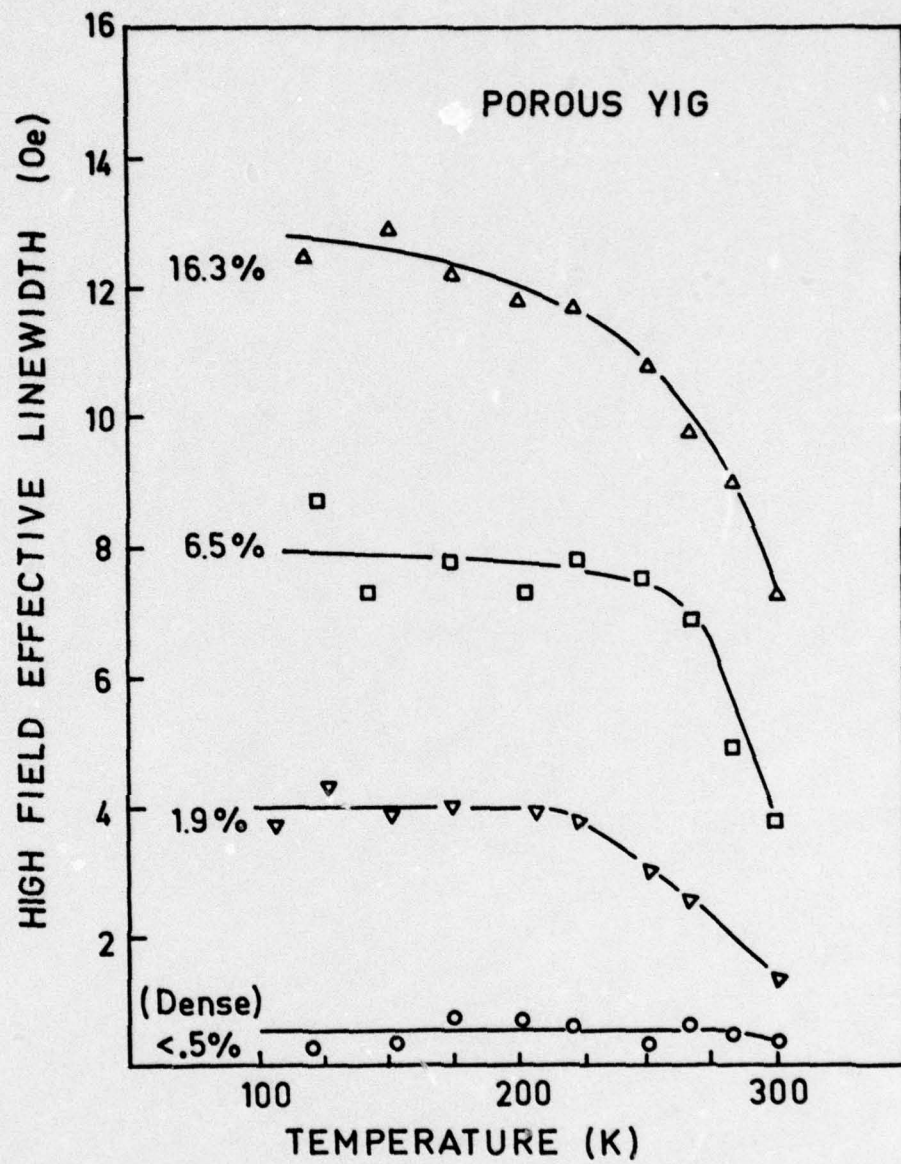
Figure VI-2. High field effective linewidth for porous YIG materials as a function of temperature.

B.   GRAIN SIZE DEPENDENCE

Systematic measurements of ΔH_{eff} versus temperature were also performed on a series of polycrystalline YIG materials with a systematic variation in grain size from over 30 μ for the dense YIG down to 1 μ for YIG prepared by hot pressing techniques. The samples used in this survey are tabulated in Table VI-2. The 30 μ sample is the same as the dense (< 0.5% porosity) sample discussed in Section A. The others were prepared by a sequence of treatments as follows: (1) the starting material was prepared by hot pressing to obtain an average grain size of 1 μ. (2) Cubes were then cut from the starting material and annealed for various times and temperatures to induce grain growth. (3) Each cube so treated was polished lightly on one face, an etch pattern was then used on that face, and a photomicrograph was made to determine the average grain size for that specific cube. (4) The cube was then ground to a sphere, annealed to remove surface strains, and used for the microwave measurements. These operations were done under the supervision of E. Maguire at Raytheon Research Division. It is to be noted that the grain growth during annealing of hot pressed samples is often accompanied by a change in porosity. The 3.2 μ sample in Table VI-2 appears to be near theoretical density, as inferred from $4\pi M_0 \sim 1750$ G. The other samples in the fine grain series have varying degrees of porosity up to about 6%.

The temperature dependence of the high field effective linewidth is shown in Fig. VI-3 for four of the fine grain samples. The results are qualitatively similar to those for the porous samples. As the average grain size decreases, one obtains an increase in ΔH_{eff}. The data for all samples appear to extrapolate to the dense YIG value of 0.5 Oe at about 330 K. The temperature dependence at low temperature appears to be somewhat

Table VI-2. Fine Grain YIG Samples.

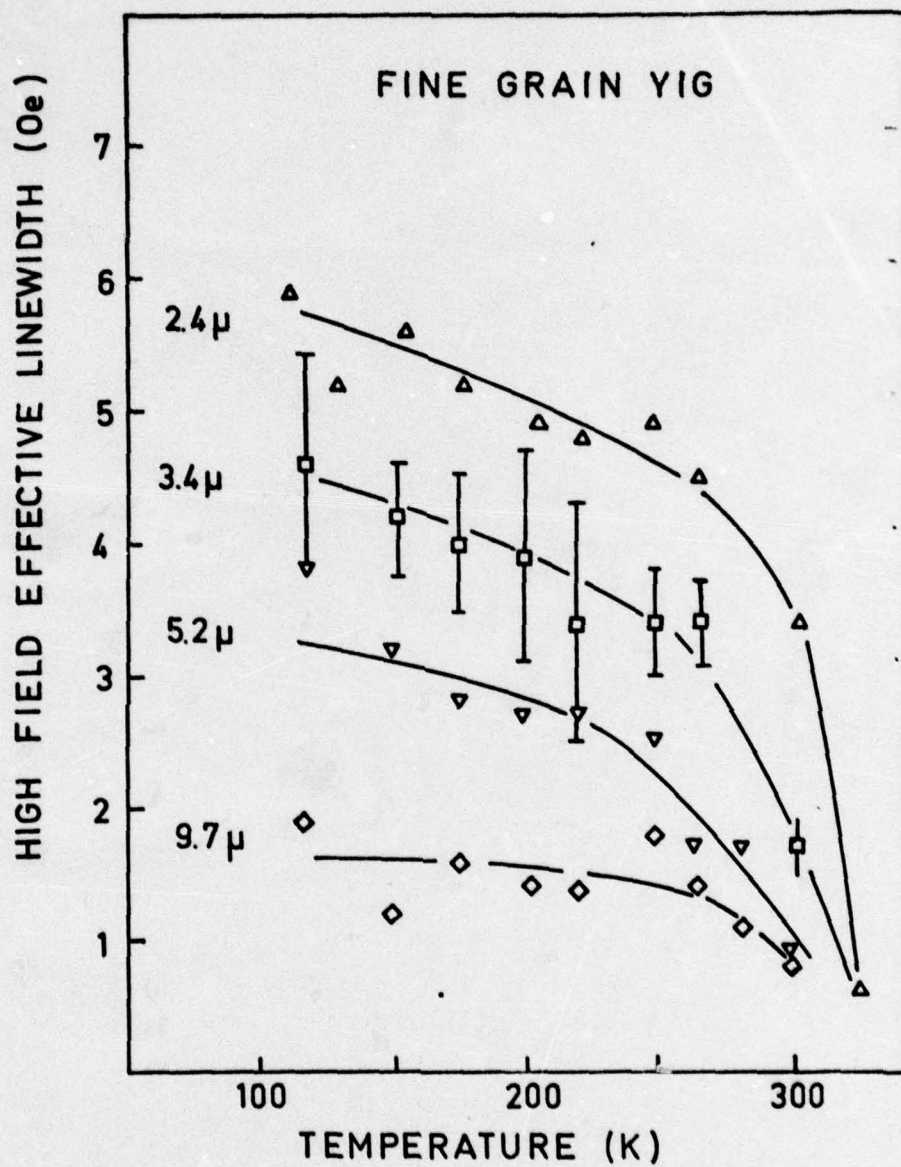| Diameter (mm)	Average Grain Size (μ)	Saturation Magnetization $4\pi M_o$ at 300°K (G)
1.796	1	1640
2.164	2.4	1680
2.604	3.2	1750
2.891	3.4	1710
2.090	5.2	1670
2.304	9.7	1640
2.310	30	1750

Figure VI-3. High field effective linewidth for fine grain YIG as a function of temperature.

stronger than for the porous samples. Otherwise, the same comments are applicable to these fine grain YIG data.

In Figure VI-4, the ΔH_{eff} values at 300 K and at 100 K are plotted versus grain size on a log-log plot. The variation at both temperatures is approximately

$$\Delta H_{eff} \propto a_o^{-1} , \qquad\qquad (VI.1)$$

where a_o is the average grain size. This inverse grain size dependence at room temperature is different from the $a_o^{-\frac{1}{2}}$ dependence previously reported (Patton, 1970; Kaelberer and Patton, 1977). The new result is certainly more reasonable in light of the a_o^{-1} dependence at low temperature. The revised grain size dependence at 300 K is due to the refined data analysis, based on an empirical calibration procedure rather than cavity perturbation theory, as discussed in Chapter III.
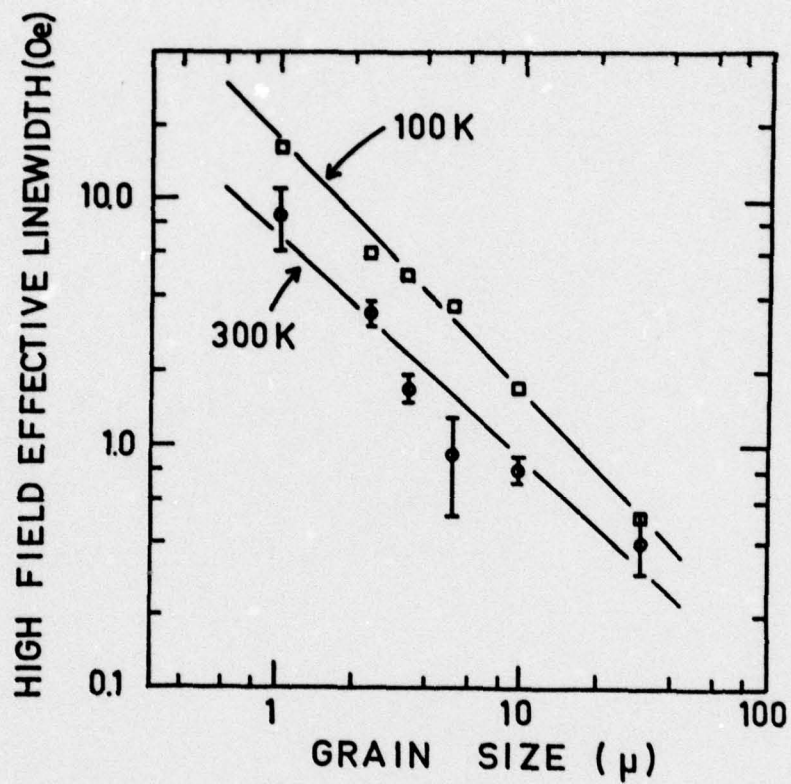
Figure VI-4.   Grain size dependence of the high field effective
                linewidth at 300 K and 100 K.

C. RELAXATION MECHANISMS

Two models have been suggested to be relevant to the off-resonance ΔH_{eff} in polycrystals. A process in which the anisotropic magnetostriction leads to phonon excitation was proposed by Schlömann (1971). He calculated a linewidth which varies as $(\lambda_{100} - \lambda_{111})^2/M$, where λ_{100} and λ_{111} are magnetostriction coefficients measured along the [100] and [111] directions, respectively. He obtained a numerical value of less than 0.1 Oe for strain free YIG at 10 GHz, which is much too small to explain the magnitude of ΔH_{eff} observed here. It was suggested that the mechanism could yield larger linewidths in polycrystals which are not strain free.

The present data provide a further test of the magnetostriction mechanism. Compared to its room temperature value, the $(\lambda_{100} - \lambda_{111})^2/M$ factor in the theory doubles at 250 K and increases seven-fold at 100 K. The data for the fine grain series do show an increase by about a factor of two in going from 300 K to 250 K for the 3.4 μ, 5.2 μ, and 9.7 μ samples, which could be a manifestation of the magnetostriction process. Below 250 K, however, the data do not show the continuous steep increase predicted by the model. Similar remarks apply to the data for the 1.9% and 6.5% porous samples.

The second mechanism which has been proposed is the transit time mechanism. The basic idea is that the lifetime of the excited mode is limited by the transit time of the traveling wave associated with the mode between grain boundaries. The grain size is the approximate mean free path for such waves between scattering interactions in which the magnon is assumed to be destroyed. For spin-waves, the transit-time-limited lifetime is easily evaluated from the group velocity,

$$\bar{v}_g = \nabla_k \, \omega_k \, ,$$

(VI.2)

with the spin-wave frequency ω_k given by

$$\omega_k = \gamma[(H_i + Dk^2)(H_i + Dk^2 + 4\Pi M_o \sin^2 \theta_k)]^{\frac{1}{2}} . \tag{VI.3}$$

Here k represents the spin-wave wave number, H_i the internal static field parallel to M_o, D is an exchange parameter on the order of 5×10^{-9} Oe-cm^2 for YIG, and θ_k is the spin-wave propagation angle relative to the static field. For low k spin-waves, one obtains

$$\bar{V}_g = \gamma Dk \, (2\gamma H_i/\omega_k) \, \hat{e}_k$$
$$+ \, (\gamma H_i/k)(\gamma 4\Pi M_o \sin\theta_k \cos\theta_k)/\omega_k \cdot \hat{e}_{\theta_k} , \tag{VI.4}$$

for $k >> 1/d$, where d is the sample size. The $\hat{e}_k$ component is linear in k, while the $\hat{e}_{\theta_k}$ component varies as $1/k$. The spin-wave transit time is just $a_o/|V_g|$, so that the transit-time-limited linewidth is

$$\Delta H_{tt} = 2|Vg|/\gamma a_o . \tag{VI.5}$$

Such a result, with a a_o^{-1} variation, a linear k dependence at moderate k values and an inverse k dependence at low k values, is in good agreement with the spin-wave linewidth data of Patton (1970). These results will be considered in more detail in Chapter VII. Of interest here is the applicability of the model for ΔH_{eff}. For a near-uniform mode, an upper limit on the group velocity can be estimated from magnetostatic mode theory to be

$$|V_g|_o \propto \Delta\omega/\Delta k \propto \gamma 4\Pi M_o/(2\Pi/d) . \tag{VI.6}$$

The corresponding effective linewidth would vary according to

$$(\Delta H_{tt})_o = C \cdot 4\Pi M_o \cdot d/\Pi a_o . \tag{VI.7}$$

The $|Vg|$ estimate applies only to samples biased near ferromagnetic resonance, and would probably need to be modified for the high field region under consideration here. The point to be emphasized is that Eq. (VI.7) can constitute a sizeable linewidth contribution, due to the $4\pi M_o d/a_o$ combination. Hence, the transit-time mechanism cannot be discounted by arguing that $k \sim 2\pi/d$ is small, $|Vg|$ from the $\hat{e}_k$ term in Eq. (VI.4) is small, and hence ΔH_{tt} is small.

The present data provide a means to test the dependences predicted in Eq. (VI.7). The only agreement is in the a_o^{-1} dependence, which can also be explained by other considerations to be discussed shortly. The observed ΔH_{eff} at high field is independent of the sample size and does not scale with $4\pi M_o$. Note that all of the data extrapolate to the residual $\Delta H_{eff} \sim$ 0.5 Oe value at about 330 K, a temperature well below the YIG Curie temperature of 560 K. Thus, it appears that a transit-time mechanism cannot adequately account for the observed high field ΔH_{eff} in polycrystalline yttrium iron garnet.

It is also clear from the data that impurity related relaxation processes are not responsible for the observed ΔH_{eff}. Recall that all samples were prepared with starting powders of the same purity. Any impurity process, therefore, should show up equally for all the samples. In addition, there is no evidence for the peak in the linewidth at low temperature that is usually found in impurity relaxation.

We have so far arrived at the following considerations:

(1) ΔH_{eff} varies as a_o^{-1} in the relatively dense fine grain samples and is an increasing function of porosity. The porosity dependence quite probably includes a grain size effect as well.

(2) For all of the porous and fine grain samples, ΔH_{eff} as a function of temperature is quite similar to a magnetization curve for a magnetic phase with $T_c \gtrsim 330$ K.

It is conceivable that small amounts of some residual magnetic phase exist in the grain boundaries between crystallites. Such a phase would likely affect the microwave relaxation to some extent and show up in the relatively small high field effective linewidth measurements. Such a contribution is consistent with the observed a_o^{-1} grain size dependence of ΔH_{eff}, since the grain boundary surface area per unit volume varies as a_o^{-1}. It is also to be noted that we are discussing a relatively small effect, one that is usually masked by other contributions in the conventional FMR experiment. If a residual magnetic phase at the grain boundaries is the origin of the large ΔH_{eff}, it would not be expected to influence the spin-wave linewidth appreciably. These considerations will be discussed in the next chapter.

CHAPTER VII

RELATION BETWEEN MICROSTRUCTURE AND SPIN-WAVE LINEWIDTH

IN POLYCRYSTALLINE YTTRIUM IRON GARNET

The central objective of the grant was to study the dependence of the loss parameters ΔH_{eff} and ΔH_k upon microstructure in polycrystalline ferrite materials. The preceeding chapter summarizes the effective linewidth results. The present chapter summarizes the limited data which have been obtained so far on the high power properties and ΔH_k. The large amount time devoted to the development of the needed instrumentation for ΔH_k and ΔH_{eff} imposed limitations on the amount of actual ferrite data. Further work on the complete series of materials considered in Chapter VI is in progress. Complete high power results will be reported at a later date. The data discussed below are limited to the 6.5% porous sample of Chapter VI.

Figures VII-1, VII-2 and VII-3 present the experimental "butterfly" curves for the 6.5% porous sample at three temperatures, 88 K, 228 K, and 368 K, respectively. These data show that h_{crit} at a given temperature is independent of field below the critical static field $H_c^{(e)}$. This $H_c^{(e)}$ is interpreted as the static field limit for $k \neq 0$ spin waves. This also means that the spin-wave linewidth ΔH_k is constant, at any given temperature, for $H_o < H_c^{(e)}$. Recall that the static fields in the above figures are external fields. The field $H_c^{(e)}$ is higher than the field H_c of Eq. (IV.5) by $4\pi M_{av}/3$ for spherical samples, where $4\pi M_{av}$ is the average magnetic induction of the porous sample at the indicated temperature.

Note also that $H_c^{(e)}$ appears to decrease by about 100 Oe in going from 88 K to 368 K. From Eq. (IV.5) and demagnetization field considerations, the static external field limited for $k = 0$ spin waves $H_c^{(e)}$ is
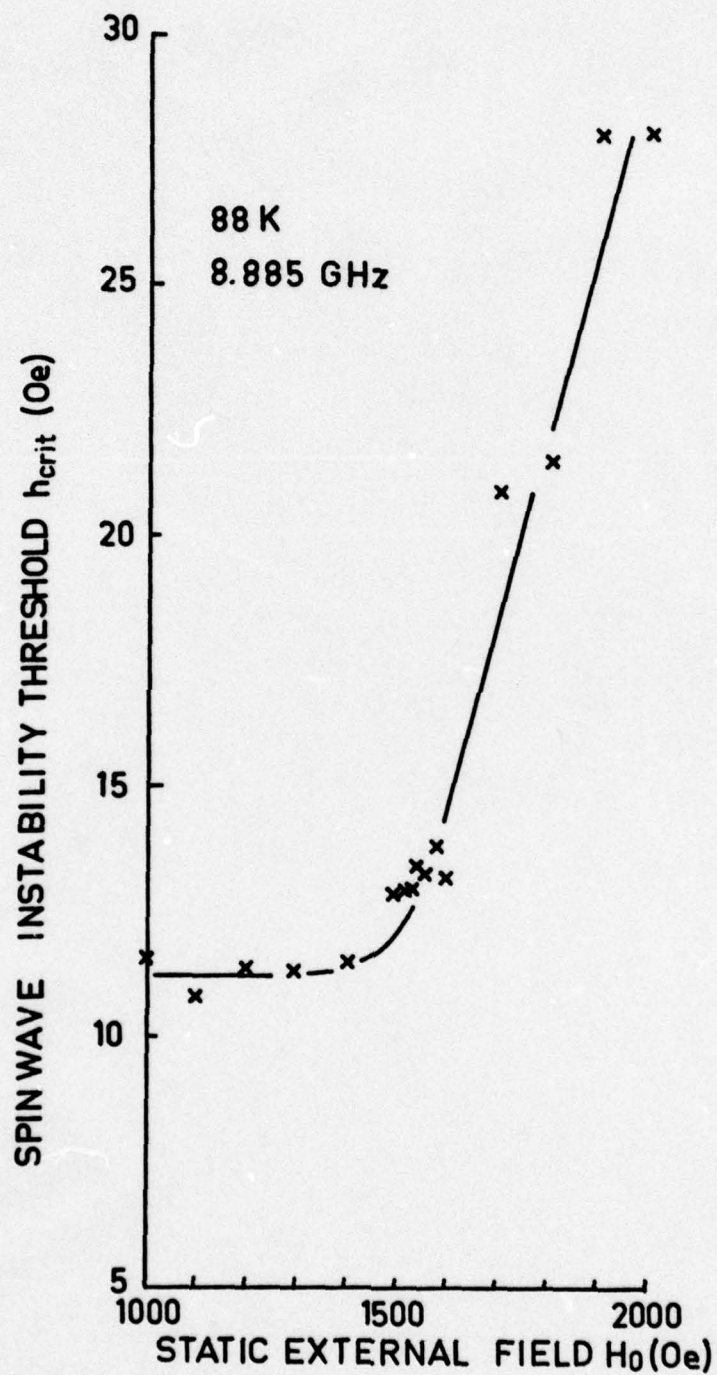
Figure VII-1. Butterfly curve of the instability threshold h_{crit} versus static external field H_0 for the 6.5% porous YIG material at 8.885 GHz and 88 K.
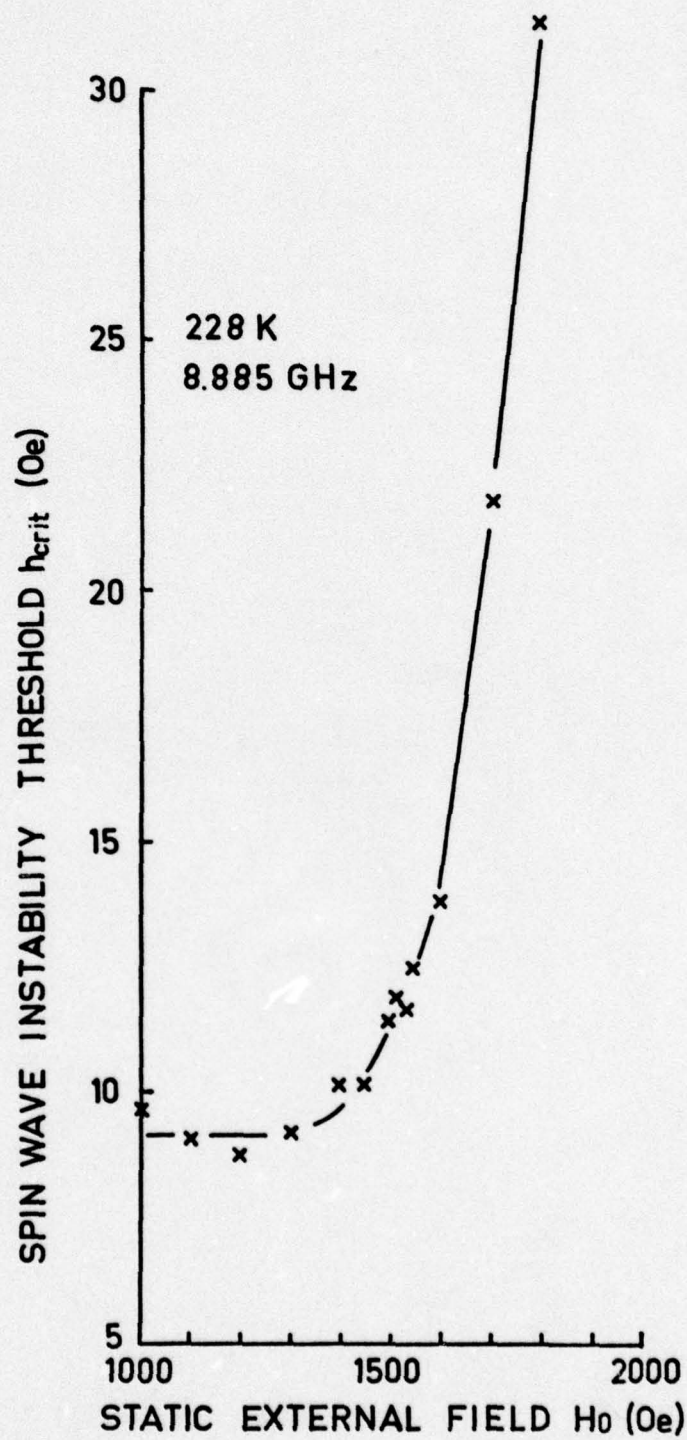
Figure VII-2. Butterfly curve of the instability threshold h_{crit} versus static field H_o for the 6.5% porous YIG at 8.885 GHz and 228 K.
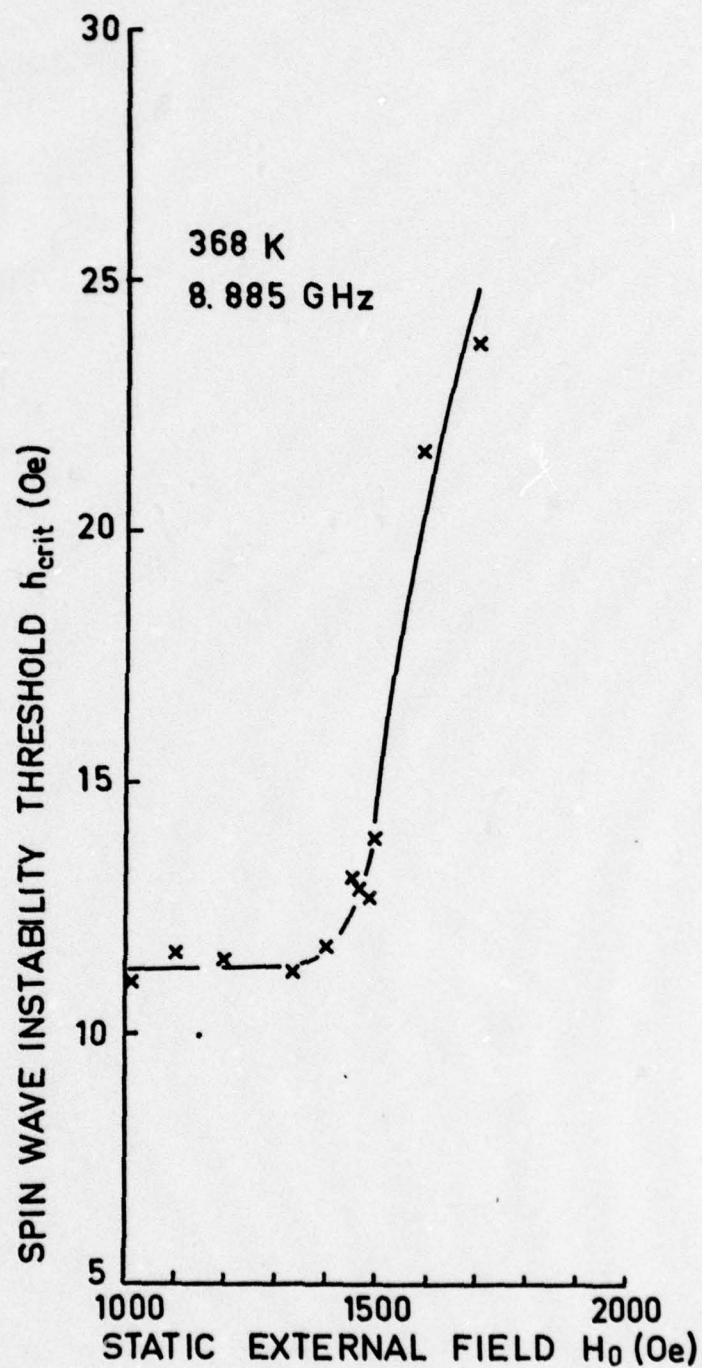
Figure VII-3. Butterfly curve of the instability threshold h_{crit} versus static field H_o for the 6.5% porous YIG material at 8.885 GHz and 368 K.

114

$$H_c^{(e)} = [(2\Pi M_o)^2 + (\omega/2\gamma)^2]^{\frac{1}{2}} - 2\Pi M_o + 4\Pi M_{av}/3 \qquad (VII.1)$$

The intrinsic magnetization M_o is related to the average magnetization M_{av} by

$$M_{av} = M_o \cdot p/100 , \qquad (VII.2)$$

where p is the porosity in per cent. The above result for $H_c^{(e)}$ is valid for single grain instability processes. Otherwise, M_o in Eq. (VII.1) should be replaced by some value on the order of M_{av}. For small porosities such distinctions are not too importnat in the present context. They can be important in the interpretation of high power data to obtain ΔH_k versus k, as will be discussed shortly. At any rate, the 100 Oe shift in going from 88 K to 368 K implies a change in $4\Pi M_o$ of about 600 - 700 Oe, in reasonable agreement with the known temperature dependence of the saturation magnetization for YIG.

Consider now the temperature dependence of the spin-wave linewidth ΔH_k for $k > 0$, as inferred from the h_{crit} data. From Chapter IV, we have

$$h_{crit} = (\omega/\gamma 4\Pi M_o) \cdot \Delta H_k \qquad (VII.3)$$

for parallel pumping with $H_o < H_c^{(e)}$ and instability processes within single grains. In obtaining ΔH_k versus temperature, the dependence of M_o on temperature must be taken into account. Table VII-1 summarizes the pertinent variables for nine temperatures between 88 K and 368 K. The $<h_{crit}>_{av}$ values below $H_o = 1400$ Oe. The $4\Pi M_o$ values are from the literature. The resulting values for $<\Delta H_k>_{av}$ are plotted in Fig. VII-4 as a function of temperature. The results are rather interesting. There appears to be a gradual, linear increase in ΔH_k with decreasing temperature from 368 K down to 120 K, and a much more rapid increase at lower temperatures.

Table VII-1. Temperature Dependence of the High Power Threshold, Saturation
Magnetization and the Spin-wave Linewidth ΔH_k.

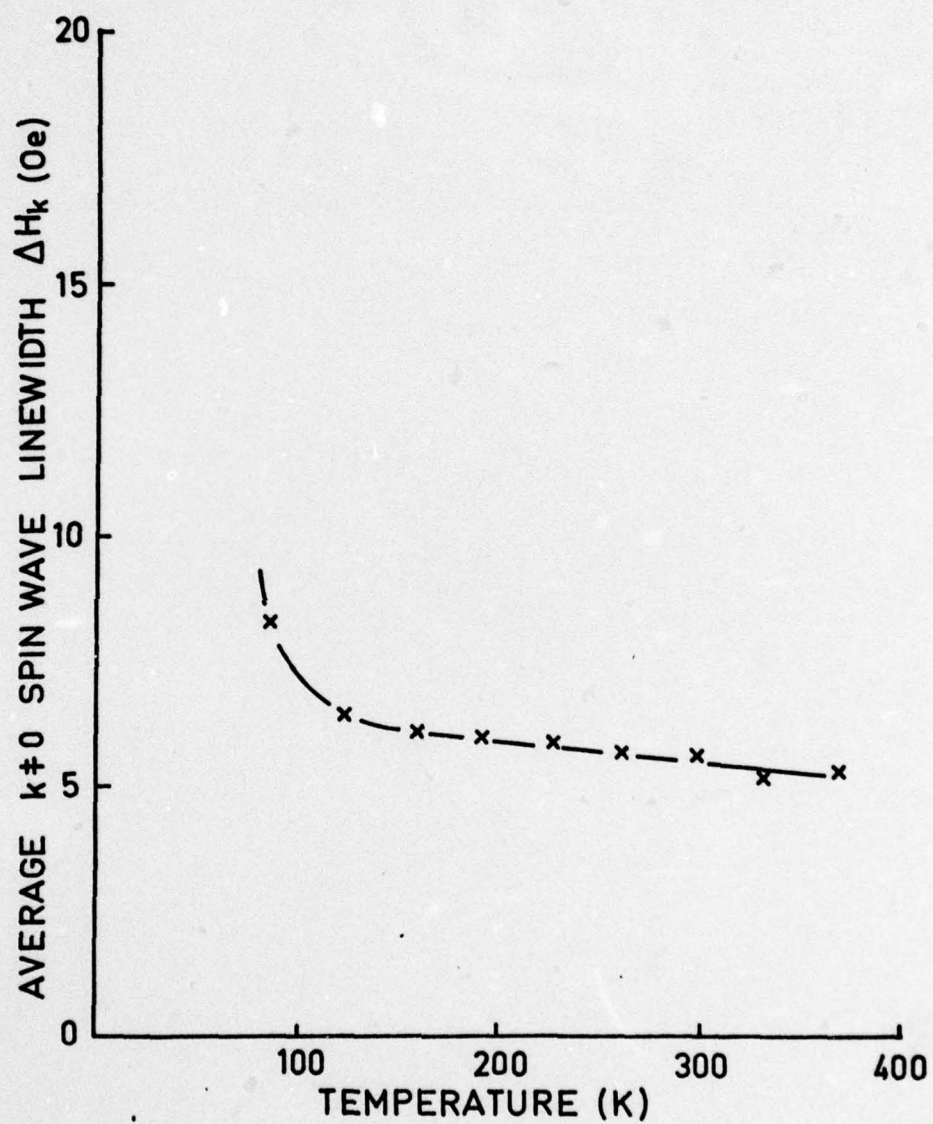| Temperature T (K)	Threshold h_{crit} (Oe)	Induction $4\pi M_o$ (G)	Spin-wave Linewidth ΔH_k (Oe)
88	11.3 ± 0.3	2300	8.2
123	9.0 ± 0.3	2250	6.4
158	8.7 ± 0.4	2200	6.0
193	8.8 ± 0.5	2100	5.8
228	9.4 ± 0.5	2000	5.9
263	9.5 ± 0.5	1880	5.6
298	10.1 ± 0.3	1760	5.6
333	10.3 ± 0.6	1580	5.1
368	11.4 ± 0.3	1460	5.3

Figure VII-4. Temperature dependence of the spin-wave linewidth ΔH_k for $k > 0$ in the 6.5% porous YIG at 8.885 GHz.

More data are needed in the 77 - 120 K range to establish this low tempera-
ture increase. Such measurements for this sample, as well as the other
samples of Chapter VI, are in progress. It would also be worthwhile to
extend the data to helium temperatures, to see if the increase continues,
or if ΔH_k peaks at some temperature below 88 K.

What do the above limited results mean? Strong conclusions would be
premature at this point, but several aspects of the data still deserve
comment.

(1) In the first place, the temperature dependence of ΔH_k appears to be
quite different from that for ΔH_{eff}. There is clearly no effect related
to the 300 K temperature evident in Chapter VI. This is somewhat consistent
with the grain-boundary second phase model proposed in Chapter VI as a pos-
sible explanation of the ΔH_{eff} results. For single-grain instability
processes, that second phase material would not affect ΔH_k.

(2) The constant h_{crit} (and ΔH_k) for $H_o < H_c^{(e)}$ at any given temperature
is different from the previous reported results of Patton (1970). The
previous data, which was limited to room temperature, suggested that h_{crit}
was dependent on H_o as to yield an inverse k-dependence for ΔH_k at low k
and a linear k-dependence at high k. The turnover point in k appeared
to increase with decreasing grain size. All of these effects appeared to
be consistent with the so-called "transit time" model alluded to in Chapter
VI. All of these results appear to now be in question!

(3) The realization, noted in conjunction with Eq. (VII-1), that a dis-
tinction should be made between M_o and M_{av} for single grain instability
processes may help to explain the previously inferred inverse k-dependence
for ΔH_k. In that analysis, the average magnetization was used instead of
M_o to calculate $H_c^{(e)}$. From Eq. (VII.1) it is seen that this leads to a

118

value which is too high, since M_o is bigger than M_{av}. The resulting

analysis then incorrectly associate the initial increase in h_{crit} (and

hence ΔH_k) with field above the correct $H_c^{(e)}$ with a decrease in k. This

problem deserves further study.

CHAPTER VIII

MICROWAVE PROPERTIES OF ARC PLASMA SPRAYED

LITHIUM FERRITE MATERIALS

A. INTRODUCTION

Recent interest in the use of arc plasma sprayed (APS) lithium ferrite materials for phased array radar applications (Babbitt, 1975) has shown the need for a study of the basic microwave properties of these APS materials. The APS process is an economical and promising method for the preparation of ferrite materials for device applications. Two important considerations are: (1) the insertion loss of the device, (2) the microwave power handling capability of the material.

Prototype phase shifters have been produced and evaluated in device configurations. However, very little basic microwave data have been reported for these materials. The present chapter reports on measurements of (1) effective linewidth (ΔH_{eff}) versus static field at 10 GHz and (2) spin-wave linewidth (ΔH_k) versus field over the parallel pumping region (0 - 1.7 kOe) at 9.2 GHz. These basic data represent the first such comprehensive measurements on arc-plasma sprayed lithium ferrite materials.

The effective linewidth concept was introduced to provide a meaningful loss parameter for ferrite materials biased at fields outside of the resonance region (Kohane and Schlömann, 1968). Phase shifters generally operate at remanence magnetization. Thus, the low field ΔH_{eff} is the relevant loss parameter. The region around resonance (manifold region) is usually characterized by a large increase in ΔH_{eff} due to anisotropy and/or porosity related inhomogeneous broadening or two-magnon scattering. The field dependence of ΔH_{eff} in this region is related to the ferrite microstructure. At high field ΔH_{eff} is generally taken as a measure of the intrinsic losses in

the absence of any two-magnon scattering or inhomogeneous broadening. Room temperature results at 9.9 GHz are reported here for all three field regions.

The spin-wave linewidth is the relaxation rate of spin-wave modes, expressed in linewidth units, which are parametrically pumped when the microwave field amplitude exceeds some critical value h_{crit}. For $h >$ h_{crit}, the material losses and the related insertion loss increase substantially over the values below h_{crit}. Therefore, h_{crit} is a quantitative measure of the power handling capability of the material. Both h_{crit} and the derived spin-wave linewidth, ΔH_k, exhibit a characteristic field dependence. Results on h_{crit} versus static field, the so-called "butterfly curve" for parallel pumping, have been obtained at room temperature and 8.9 GHz. These data were used to calculate the wave number dependence of ΔH_k. This dependence is related to the ferrite microstructure and to grain size effects in particular.

B. FERRITE MATERIALS

The arc plasma spray (APS) materials were fabricated and supplied by R. W. Babbitt and coworkers at the Army Electronics Command. They consisted of long, rectangular ferrite toroids sprayed directly on dielectric cores. The ferrite material was machined to a thickness of about 1.5 mm. To obtain spherical samples for the basic microwave measurements, cubes of ferrite material were cut from the toroids and ground into spheres of 1.0 - 1.4 mm diameter by a two-pipe lapidary method. The toroids were initially sprayed from two types of powders, Ampex 1202 powder ($Li_{0.79}$ $Fe_{1.63}$ $Ti_{0.57}$ $Mn_{0.03}$ O_4) and Ampex 1200 powder (composition similar to 1202 but with Zn additions). Both powders have saturation magnetizations ($4\pi M_o$) on the order of 1200 G. For comparison, samples were also cut and ground from a conventionally sintered 1200 G substituted lithium ferrite materials, Trans-Tech L-27-J.

Table VIII-1 lists the samples, powder preparation, grain size, and measured $4\pi M_{av}$ for the materials studied. The values of $4\pi M_{av}$ were determined at 8 kOe applied field by standard vibrating sample magnetometry. The $4\pi M_{av}$ values are accurate to ±4%. The small error is due to an uncertainty in the sample volume determinations on the small spheres. The average grain sizes were estimated from electron microscopy photographs.

Table VIII-1. Sample composition and microstructure for the lithium
ferrite materials of this study.

Sample code number	Sample preparation	Average grain size (μ)	$4\pi M_{av}$ (G)
APS C-L-113	Ampex 1202 powder fully reacted	7.4	1240
APS C-L-122	Ampex 1202 powder fully reacted	4.7	1200
APS C-L-163	Ampex 1202 powder spray dried	11.1	1140
APS C-L-130	Ampex 1202 powder fully reacted (no anneal)	-	1210
APS C-L-012	Ampex 1200 powder partially reacted (with Zn addition)	-	1110
APS C-L-077	Ampex 1200 powder spray dried (with Zn addition)	7.3	1220
Trans-Tech L-27-J	Conventional firing	large	1240

C. EFFECTIVE LINEWIDTH

The experimental technique used to measure the effective linewidth was discussed in Chapters II and III. To measure the effective linewidth in the manifold region, from about 3 kOe to 4.5 kOe, a TE_{102} rectangular cavity with a relatively low Q of about 1700 was used. Data were taken at 9.9 GHz and room temperature. Temperature stabilization of the cavity was not necessary. Representative data are shown in Fig. VIII-1. The field dependence of ΔH_{eff} for all the samples is similar to that for dense Ca-V substituted YIG with large magnetocrystalline anisotropy and porous YIG with relatively high porosities (>5%). The APS materials exhibit larger losses than the conventional fired L-27-J, presumably an indication of the increased porosity of materials fabricated by the APS method.

Some correlation with composition and grain size can also be seen in the tabulation of the peak ΔH_{eff} values given in Table VIII-2. The samples are listed in order of decreasing ΔH_{eff}. The four samples with the largest ΔH_{eff} are from the Ampex 1202 powder with no Zn additions. Of this group, the largest value of ΔH_{eff} was measured for the C-L-122 sample which has the smallest average grain size. The two samples, C-L-012 and C-L-077, sprayed from Ampex 1200 powder with Zn additions, have lower peak ΔH_{eff} values. This may be related to a reduction in crystalline anisotropy reported for conventional Zn substituted Li ferrite (Baba et al., 1972). The smallest ΔH_{eff} was found for the conventional, commercially prepared Trans-Tech L-27-J. Although none of the APS materials have effective linewidths as low as the conventionally prepared material, those with Zn additions do appear to have reduced effective linewidths in the manifold region. Although the data are somewhat limited and not completely consistent,
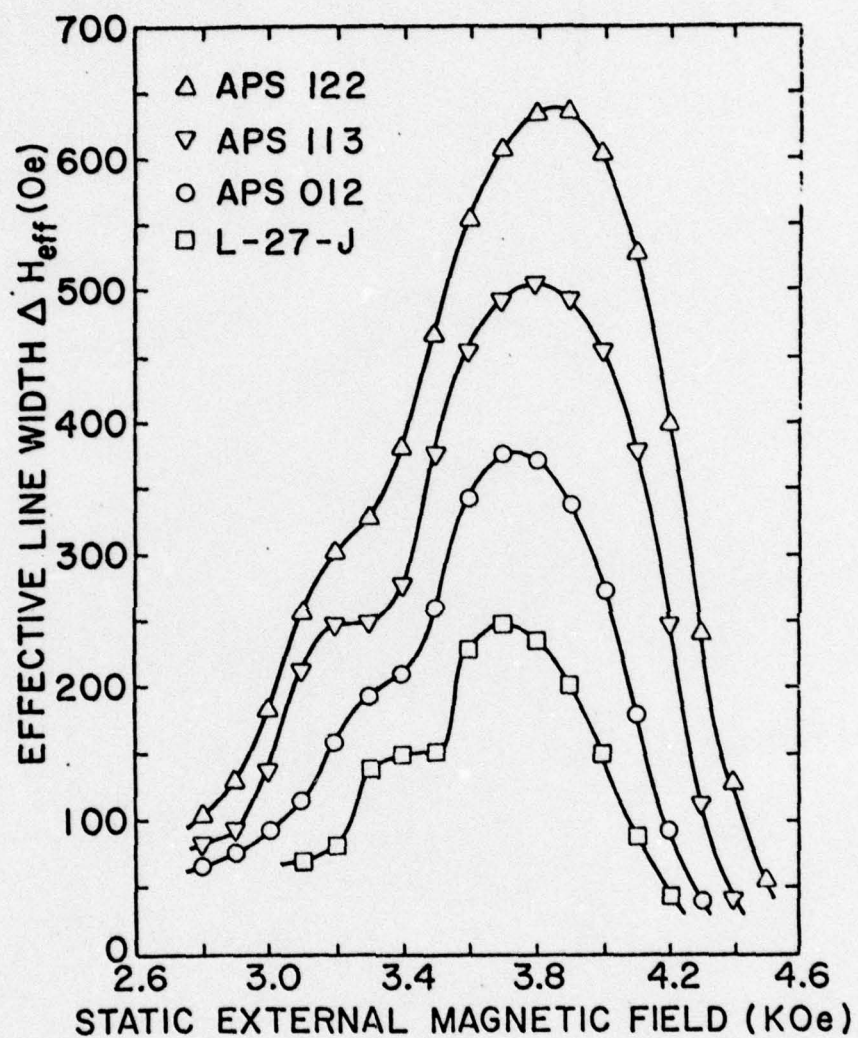
Figure VIII-1. Effective linewidth as a function of static external magnetic field in the manifold region for the lithium ferrite materials.

Table VIII-2. Peak effective linewidth measured in the manifold region, sample composition and average grain size for the lithium ferrite materials.

Sample	Peak H_{eff}(Oe)	Material	Average grain size (μ)
C-L-122	630	APS 1202	4.7
C-L-163	520	APS 1202	11.1
C-L-130	510	APS 1202	-
C-L-113	500	APS 1202	7.4
C-L-012	370	APS 1200 (Zn addition)	-
C-L-077	330	APS 1200 (Zn addition)	7.3
L-27-J	250	Conventional	large

it also appears that a small ΔH_{eff} in the manifold region is related to large average grain size.

Outside the manifold region, at fields below 3 kOe or above 4.5 kOe, two-magnon scattering and inhomogeneous broadening related to low k spin-waves are absent. The relaxation rate is considerably reduced, compared to the values in the manifold region. Very accurate measurements of cavity parameters are necessary to determine the effective linewidth. For these off-resonance ΔH_{eff} determinations, the TE_{011} cylindrical cavity described in Chapter III was used. Measurements were made at 9.8 GHz with the cavity temperature stabilized at 8°C ± 0.04°C.

Representative data outside the manifold region are shown in Fig. VIII-2. These ΔH_{eff} values are smaller than the values measured in the manifold region by a factor of 50. For these off-resonance ΔH_{eff} data, there appears to be no consistent correlation between APS parameters and the losses. The effective linewidths at high field for the APS materials are about 5-10 Oe. The conventionally prepared L-27-J has a high field ΔH_{eff} of about 4 Oe. These values are quite comparable. For fields around 2 kOe, the ΔH_{eff} for all samples is slightly higher than at high field, on the order of 10 Oe. Precise measurements are precluded by the large inhomogeneous broadening contributions which expand the manifold region, and by experimental problems at low fields (< 2 kOe) due to low susceptibilities and small samples.

It is clear, however, that the relevant linewidth parameter for the APS materials in phase shifter applications is on the order of 5-10 Oe. This value is comparable to the low-field ΔH_{eff} for conventionally prepared materials.
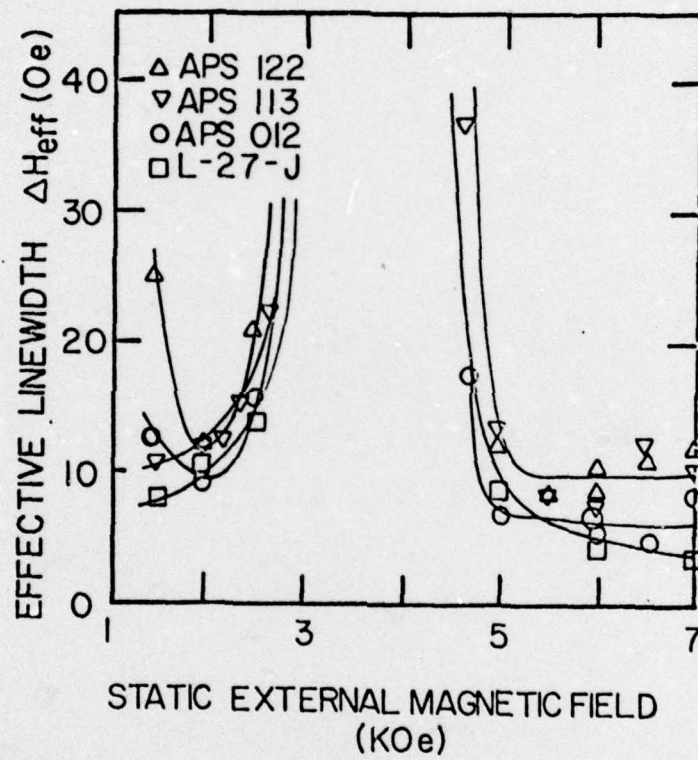
Figure VIII-2.   Effective linewidth as a function of static external
magnetic field outside the manifold region for the
lithium ferrite materials.

D. SPIN-WAVE LINEWIDTH

The microwave threshold field (h_{crit}) for parallel pump spin-wave instability is shown as a function of static applied field in Fig. VIII-3. Here samples C-L-122 and C-L-113, sprayed from Ampex 1202 powder and annealed, exhibit values of h_{crit} only slightly higher than those for the commercial Trans-Tech L-27-J material. The C-L-130 sample, sprayed from 1202 powder but not annealed, has significantly higher values of h_{crit}. The C-L-012 and C-L-077 samples were sprayed from Ampex 1200 powder which contains a small amount of Zn (approximately 0.05 Zn atoms per formula unit). It is to be noted that the magnetization of sample C-L-012 may be quite non-uniform. This non-uniform $4\pi M_s$ is a likely cause of the large microwave threshold field in this sample, compared to the C-L-077. It is clear, however, that both 1200 powder samples exhibit higher thresholds than those of the 1202 powder samples. The following conclusions are suggested by the data of Fig. VIII-3. (1) The results for the 1202 powder samples (C-L-113, C-L-122, C-L-130) indicate that the APS process can produce a significant increase in h_{crit}, most of which is lost upon annealing. (2) Comparison of the 1200 powder samples (C-L-012, C-L-077) with the 1202 powder samples (C-L-113, C-L-122, C-L-130) shows that Zn additions increase the microwave power capability for APS materials, as has been noted for conventionally sintered ferrites. (3) An inhomogeneous magnetization, which can be produced by the APS process as for C-L-012, may be reflected in large apparent h_{crit} values.

The wave number dependence of the spin-wave linewidth (ΔH_k) may be obtained from the Suhl-Schlömann spin-wave instability theory; and the butterfly curve data of Fig. VIII-3. These results are shown in Fig. VIII-4. The sample to sample variation in ΔH_k is qualitatively similar to the variation in h_{crit}, with ΔH_k ($k \to 0$) values ranging from 2.6 Oe for the
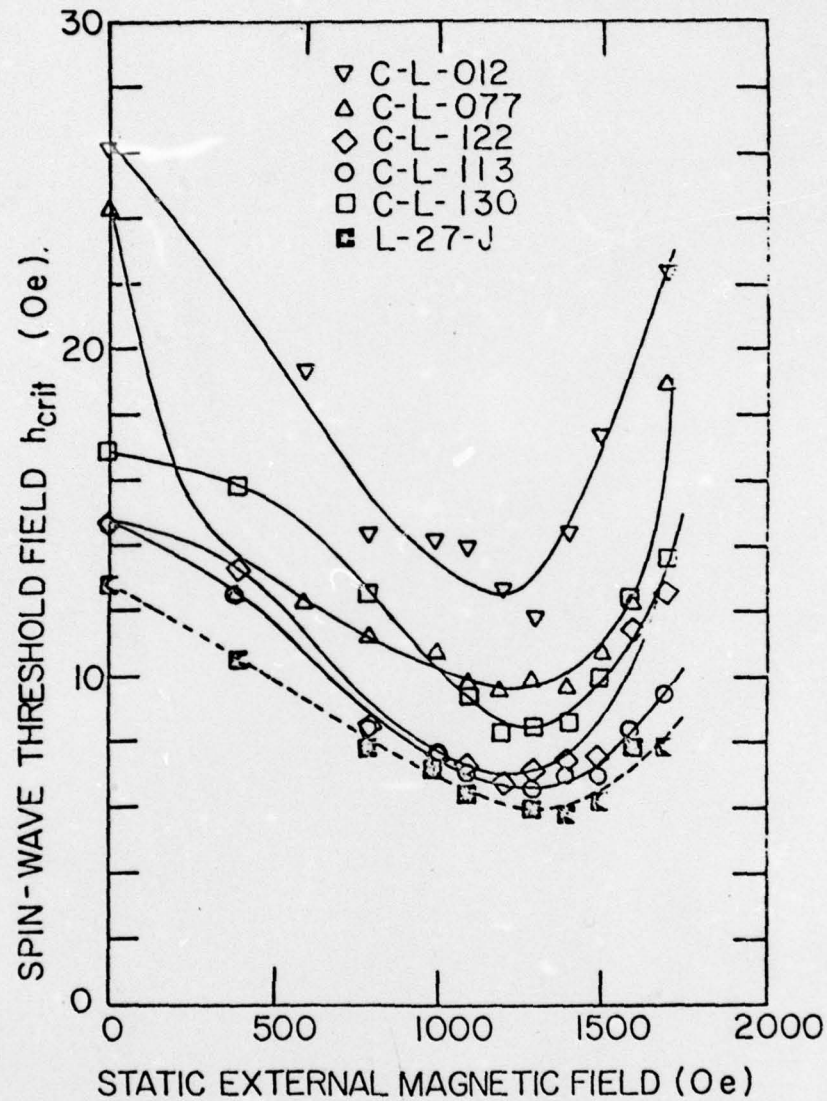
Figure VIII-3. Spin-wave threshold field as a function of static external magnetic field for the lithium ferrite materials.
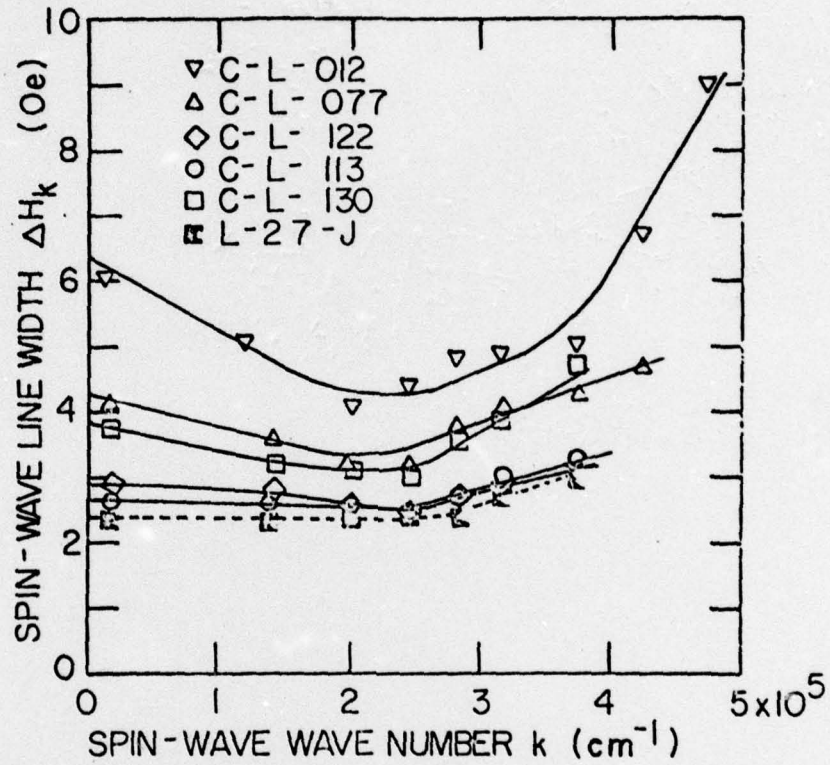
Figure VIII-4. Spin-wave linewidth as a function of spin-wave wave numbers for the lithium ferrite materials.

conventionally sintered L-27-J, to 6 Oe for the Zn doped APS C-L-012.

The ΔH_k versus k behavior summarized in Fig. VIII-4 is of funda-
mental interest. Below k $\approx$ 2 x 10^5 cm^{-1}, ΔH_k is an increasing function
of k. This general behavior is qualitatively similar to the behavior for
fine grain and porous YIG. In YIG, the inverse k-dependence of ΔH_k below
k $\approx$ 2 x 10^5 cm^{-1} has been qualitatively related to spin-wave transit time
arguments. The available microstructure data on the APS materials also
indicate relatively small grains. Therefore, it is likely that the ΔH_k
versus k dependence in Fig. VIII-4 for the APS materials is related to
grain size effects.

E. DISCUSSION

The large values of ΔH_{eff}, up to 650 Oe, in the manifold region are clearly related to the porosity and microstructure inherent in the APS process. The values are reduced by the addition of Zn. At low field ($\sim$ 2 Oe) or above 5 kOe, the effective linewidths of the APS materials are less than 10 Oe, comparable to those of conventionally prepared materials. The variations observed from sample to sample show no clear microstructure correlations. The high power data show that Zn additions increase h_{crit} and ΔH_k, opposite to the effect of Zn on ΔH_{eff} in the manifold region. This result is quite peculiar. The ΔH_{eff} in the manifold region and the high h_{crit} values must both be microstructure related. It is perplexing that a microstructure effect, which increases ΔH_{eff}, can cause a decrease in ΔH_k. Some clues to this behavior may be inferred from previous work on the effect of Zn. As previously mentioned, Baba, et al. (1972) report that Zn reduces the magnetocrystalline anisotropy. This may be the cause of the reduction in ΔH_{eff}. West and Blankenship (1967) report that Zn can increase porosity in hot pressed Li-ferrite. This may be related to the ΔH_k increase.

The most important practical observations are: (1) zinc substitution increases ΔH_k, while decreasing ΔH_{eff} in the manifold region; (2) the off-resonance loss properties are comparable to the losses in conventional materials; (3) the high power capability is the same or better than that of conventional materials. These observations in combination with the economic advantages of the APS process indicate the utility of these lithium ferrite materials for phase shifter applications.

BIBLIOGRAPHY

Baba, P. D., Argentina, G. M., Courtney, W. E., Dionne, G. F., and Temme, D. H., "Fabrication and Properties of Microwave Lithium Ferrites", IEEE Trans. Magnetics $\underline{8}$, 83 (1972).

Babbitt, R. W., "Arc Plasma Sprayed C-Band Lithium Ferrite Phase Shifters", IEEE Trans. Magnetics $\underline{11}$, 1253 (1975).

Burgemeister, E. A., "The Thermal Conductivity of Diamond Heat Sinks", Industrial Diamond Review, July, 1975, p. 242.

Collins, G. B., ed. "Microwave Magnetrons", MIT Radiation Laboratory Series, Vol. 6, (McGraw-Hill, New York, 1948).

Glasoe, G. N. and Lebacq, J. V., eds., "Pulse Generators", MIT Radiation Laboratory Series, Vol. 5, (McGraw Hill, New York, 1948).

Green, J. J. and Kohane, T., Semicond. Prod. $\underline{7}$, No. 8, 46 (1964).

Kaelberer, R. E., Temperature Dependence of the Effective Linewidth in Yttrium Iron Garnet, Ph.D. Thesis, Colorado State University (1978).

Kaelberer, R. E. and Patton, C. E., "Temperature Dependence of the Effective Linewidth in Porous and Fine Grain Yttrium Iron Garnet", IEEE Trans. Magnetics $\underline{13}$, 1230 (1977).

Kohane, T. and Schlömann, E., "Linewidth and Off-Resonance Loss in Poly-crystalline Ferrites at Microwave Frequencies", J. Appl. Phys. $\underline{39}$, 720 (1968).

Landau, L. and Lifshitz, E., "On the Theory of the Dispersion of Magnetic Permeability in Ferromagnetic Bodies", Phys. Z. Sowjet. $\underline{8}$, 153 (1935).

Morgenthaler, F. R., "Survey of Ferromagnetic Resonance in Small Ferro-magnetic Ellipsoids", J. Appl. Phys. $\underline{31}$, 95S (1960).

Motizuke, K., Sparks, M., and Seiden, P. E., "Theory of Ferromagnetic Resonance Line Shape Outside the Spin-Wave Manifold", Phys. Rev. $\underline{140}$, A972 (1965).

Patton, C. E., "Effect of Grain Size on the Microwave Properties of Poly-crystalline Yttrium Iron Garnet", J. Appl. Phys. $\underline{41}$, 1637 (1970).

Patton, C. E., Magnetic Oxides, Part 2, D. J. Craik, ed. (John Wiley, London, 1975), Chapter 10, pp. 575-648.

Patton, C. E. and Kohane, T., "Ultrasensitive Technique for Microwave Susceptibility Determination Down to 10^{-5}", Rev. Sci. Instr. $\underline{43}$, 76 (1972).

Patton, C. E. and Green, J. J., "Automatic System for Determining the Spin-Wave Instability Threshold in Ferromagnetic Materials at Microwave Frequencies", Rev. Sci. Instr. $\underline{42}$, 193 (1971).

Schlömann, E., "Behavior of Ferrites in the Microwave Frequency Range", J. Phys. (France) <u>32</u> C1-443 (1971).

Schlömann, E., Green, J. J., and Milano, U., "Recent Developments in Ferromagnetic Resonance at High Power Levels", J. Appl. Phys. <u>31</u> 386S (1960).

Sparks, M., <u>Ferromagnetic Relaxation Theory</u>, (McGraw Hill, New York, 1964).

Vrehen, Q. H. F., "Absorption and Dispersion in Porous and Anisotropic Polycrystalline Ferrites at Microwave Frequencies", J. Appl. Phys. <u>40</u>, 1849 (1969).

West, R. G. and Blankenship, A. C., "Magnetic Properties of Dense Lithium Ferrite", J. Amer. Ceram. Soc. <u>50</u>, 343 (1967).

APPENDIX I. PERSONNEL

Two faculty members, four graduate students, and four undergraduate students were involved in the ARO research program. Because the program was essentially started from scratch, with no previously existing microwave research facilities, a large amount of the effort was devoted to equipment design and construction. This work provided a useful training ground for all participants. The following enumerates the personnel and their specific activities.

Principal Investigator, Carl E. Patton

Following the funding of the grant, he was primarily involved in setting up initial ferromagnetic resonance measurement equipment, a vibrating sample magnetometer, and a facility for the grinding of suitable samples. He was also involved in the design of the effective linewidth spectrometer. He was involved in theoretical work related to ferrite relaxation processes. He participated in varying degrees in the specific projects described below, as well, by supervising the work in progress and serving as a sounding board for new ideas.

Postdoctoral Fellow, Geoffrey O. White

His primary responsibility was the design, construction, and utilization of the high power microwave system for spin-wave linewidth evaluation. Work was done on porous YIG and Li ferrite. He was also instrumental in obtaining much of the equipment needed for the program from the federal excess property operation. A number of magnets, power supplies, high frequency sources, and oscilloscopes, as well as numerous microwave components, were obtained in this way. A considerable effort was also devoted to the renewal proposal on Li ferrite and a review article to appear in J. Magnetism and Magnetic Materials.

Graduate Students:

Ronald E. Kaelberer, Ph.D., 1978 (Physics)

His thesis project concerned the temperature dependence of the effective linewidth in polycrystalline ferrite. This required the design of the high sensitivity transmission cavity and extensive measurements using that system.

LuVerne Peterson, M.S., 1977 (Physics)

The thesis project was concerned with nonlinear effects in single crystal YIG. The so-called "fine structure" in the instability onset was observed using cw techniques, by means of a conventional EPR system.

Undergraduate Students:

Tony Mallon, B.S., 1975 (Physics)

Dennis White, B.S., 1976 (Physics)

Helmut Schmidt, B.S., 1977 (Physics)

These physics majors worked on the project for research credit and as hourly assistants. They participated primarily in the construction of equipment and experimental measurements.

Clint Seanor, B.S., 1978 (Geology)

He was concerned with the design and construction of facilities for sphere grinding and with the preparation of ferrite samples.

APPENDIX II. PUBLICATIONS

The following publications report work on microwave materials and phenomena that was supported in part by this grant.

1. "Spin Wave Relaxation and Phenomenological Damping in Ferromagnetic Resonance", V. Kambersky and C. E. Patton, AIP Conf. Proc. 24, 516 (1975).

2. "Linewidth and Relaxation Processes in Microwave Ferrites", C. E. Patton, IEEE Trans. Magnetics 11, 911-919 (1975). [Section III of "Annotated Literature Survey of Microwave Ferrite Materials and Devices", D. M. Bolle and L. R. Whicker, IEEE Trans. Magnetics 11, 907-926 (1975).]

3. "Spin-Wave Relaxation and Phenomenological Damping in Ferromagnetic Resonance", V. Kambersky and C. E. Patton, Phys. Rev. B11, 2668-2672 (1975).

4. "Classical Theory of Spin-Wave Dispersion for Ferromagnetic Metals", C. E. Patton, Czech. J. Phys. B26, 925-935 (1976).

5. "Characterization of Ferromagnetic Precipitates in Glasses by Ferromagnetic Resonance", E. J. Freibele, D. L. Griscom, and C. E. Patton, Proc. Second International Symposium on Amorphous Magnetism (1977).

6. "Microwave Properties of Arc Plasma Sprayed Lithium Ferrite", R. E. Kaelberer, G. O. White and C. E. Patton, J. Physique (France), C1-225 to C1-259 (1977).

7. "Temperature Dependence of the Effective Linewidth in Porous and Fine Grain Polycrystalline Yttrium Iron Garnet", IEEE Trans. Magnetics 13, 1230-1232 (1977).

8. "Magnetic Properties of Li-Ferrite Microwave Materials", G. O. White and C. E. Patton, J. Magnetism and Magnetic Materials (1978), to be published.

The following theses were produced under grant support.

"Temperature Dependence of the Effective Linewidth in Polycrystalline
   Yttrium Iron Garnet", Ronald E. Kaelberer, Ph.D., July, 1978.

"Fine Structure in the Subsidiary Absorption of Yttrium Iron Garnet Single
   Crystals at 9.45 GHz", LuVerne Peterson, M.S., May 1977.

Several publications of work related to the grant are in preparation.

1.   "Temperature Dependence of the Spin-Wave Linewidth in Polycrystalline
      YIG".
2.   "Economical High Power Pulsed Microwave Source for Ferrite Evaluation".
3.   "A Simple, High Stability Temperature Control System for Microwave
      Ferrite Evaluation, 77-368K".